Imaging through optical multimode fiber: towards ultra-thin endoscopy

by

Szu-Yu Lee
B.S. Electrical Engineering, National Taiwan University, 2013
M.S. Photonics and Optoelectronics, National Taiwan University, 2015

Submitted to the Harvard-MIT Program in Health Sciences and Technology in partial fulfillment of the requirements for the degree of

Doctor of Philosophy in Medical Engineering and Medical Physics

at the

Massachusetts Institute of Technology

June 2022

Signature of Author:

Harvard-MIT Health Sciences and Technology
May 13, 2022

Certified by Thesis Advisors:

Brett Bouma, PhD/Professor of Dermatology at
Massachusetts General Hospital and Harvard Medical School

Martin Villiger, PhD/Assistant Professor of Dermatology at
Massachusetts General Hospital and Harvard Medical School

Accepted by:

Emery N. Brown, MD, PhD/Director, Harvard-MIT Program in Health Sciences and Technology/Professor of Computational Neuroscience and Health Sciences and Technology

Imaging through optical multimode fiber: towards ultra-thin endoscopy

Szu-Yu Lee

Harvard-MIT Health, Sciences, & Technology
Massachusetts Institute of Technology

Submitted to the Harvard-MIT Program in Health Sciences and Technology in partial fulfillment of the requirements for the degree of Doctor of Philosophy

June 2022

Abstract

Optical imaging in biomedicine provides pathophysiological information with high resolution, high speed, and minimal invasiveness. Endoscopy in particular has revolutionized healthcare diagnosis and treatment as well as biological research by offering visual access to otherwise unreachable remote tissues. However, existing endoscopic modalities face fundamental limitations in their designs that prohibit miniaturization to below a few millimeters in diameter, which would enable imaging through any natural or artificial lumen and thus unprecedented opportunities. This predicament and unmet medical needs such as deep-brain imaging, imaging-guided needle biopsy, and imaging-guided micro-surgery for new and scalable endoscope designs have motivated the concept of utilizing a single optical multimode fiber (MMF) as a stand-alone image conduit. MMF is fascinating as an optical waveguide attributed to its ultra-small footprint, high data throughput, low cost, and flexibility. Nevertheless, the mode mixing and dispersion effects inherent to MMF are technical barriers to its ability to relay clear images; optical propagation through a short length of MMF scrambles an image completely. The focus of this dissertation research is therefore to study waveguide physics of MMF and to innovate powerful computational methods as compensatory strategies that enable high fidelity imaging and sensing through the fiber: We developed numerical simulation toolboxes and experimental measurement systems to characterize bi-directional light transport through MMF; By modeling the light transmission through MMF and sample interaction with matrix operations, we demonstrated three-dimensional (3D) label-free multi-modal imaging based on computational reconstruction; To facilitate multi-spectral and broadband operations with MMF, we established a parametric dispersion model for efficient fiber calibration across a broad spectrum; The spatio-temporal modes within the MMF can be conveniently leveraged for depth sensing, where we created a high-resolution and long-range axial profiling system using MMF; Finally, we showed a proximal MMF calibration method for implementing flexible MMF-based endoscopes by exploiting the waveguide physics and numerical optimization.

Acknowledgements

I would like to express my gratitude to my primary supervisor, Prof. Brett Bouma, who guided me throughout this Ph.D. journey and provided consistent financial support so that I could concentrate on my research.

I am deeply grateful to my research mentor, Prof. Martin Villiger, who worked closely with me in each project from research direction to backbone theory to system design and implementation to debugging to numerical processing to presenting to preparing the manuscript. He struggled with me when things did not work out and taught me the research mindset by his own example.

I would like to thank my collaborator, Prof. Vicente Parot, who provided insights in numerical simulation, numerical processing, and debugging experimental setup. He also gave useful suggestions and constructive criticism in my presentation and manuscript preparation.

I would like to thank my other collaborator, Dr. Wallace Hui, who worked with me in the fiber sensing project and provided useful suggestions in manuscript preparation.

I would like to thank Dr. Norman Lippok, who taught me fiber splicing and configuring laser modules, and gave me suggestions regarding experimental setup when I first joined the Bouma lab.

I would like to thank Dr. Milen Shishkov, who provided technical support in machining components for my experimental setup.

I would like to thank all the Bouma lab members, who made the lab a friendly environment.

I am grateful for the support from my parents, brother, and friends in Taiwan, and would also like to thank my local friends here in Boston, who added color to my gloomy research life.

Last but not least, I want to thank my wife, Pei-Yu, who came with me to the States with great courage and sacrifice, and supported me through all the ups and downs in the past six years. My accomplishment of the degree and achievements in research would be impossible without her love, patience, and encouragement.

Abstract

Optical imaging in biomedicine provides pathophysiological information with high resolution, high speed, and minimal invasiveness. Endoscopy in particular has revolutionized healthcare diagnosis and treatment as well as biological research by offering visual access to otherwise unreachable remote tissues. However, existing endoscopic modalities face fundamental limitations in their designs that prohibit miniaturization to below a few millimeters in diameter, which would enable imaging through any natural or artificial lumen and thus unprecedented opportunities. This predicament and unmet medical needs such as deep-brain imaging, imaging-guided needle biopsy, and imaging-guided micro-surgery for new and scalable endoscope designs have motivated the concept of utilizing a single optical multimode fiber (MMF) as a stand-alone image conduit. MMF is fascinating as an optical waveguide attributed to its ultra-small footprint, high data throughput, low cost, and flexibility. Nevertheless, the mode mixing and dispersion effects inherent to MMF are technical barriers to its ability to relay clear images; optical propagation through a short length of MMF scrambles an image completely. The focus of this dissertation research is therefore to study waveguide physics of MMF and to innovate powerful computational methods as compensatory strategies that enable high fidelity imaging and sensing through the fiber: We developed numerical simulation toolboxes and experimental measurement systems to characterize bi-directional light transport through MMF; By modeling the light transmission through MMF and sample interaction with matrix operations, we demonstrated three-dimensional (3D) label-free multi-modal imaging based on computational reconstruction; To facilitate multi-spectral and broadband operations with MMF, we established a parametric dispersion model for efficient fiber calibration across a broad spectrum; The spatio-temporal modes within the MMF can be conveniently leveraged for depth sensing, where we created a high-resolution and long-range axial profiling system using MMF; Finally, we showed a proximal MMF calibration method for implementing flexible MMF-based endoscopes by exploiting the waveguide physics and numerical optimization.

Contents

List of Figures

List of Tables

List of Abbreviations

MMF	multimode fiber
SMF	single mode fiber
SI-MMF	step-index multimode fiber
GI-MMF	graded-index multimode fiber
GRIN	graded index
MCF	multi-core fiber
MEMS	microelectromechanical systems
PDT	photo-dynamic therapy
LG	Laguerre-Gaussian
HG	Hermite-Gaussian
LP	linear polarizer
WFS	wavefront shaping
DOPC	digital optical phase conjugation
TM	transmission matrix
SVD	singular value decomposition
SV	singular value
1-D, 2-D, 3-D	one-, two-, three- dimensional, referring in this thesis to spatial dimensions
NA	numerical aperture
DOF	degree of freedom
FOV	field of view
PSF	point spread function

FWHM . . . . full width half maximum

SNR . . . . . signal to noise ratio

SBR . . . . . signal to background ratio

PIM . . . . . propagation invariant mode

PM . . . . . principal modes

SDM . . . . . spatial division multiplexing

REM . . . . . random encoding matrix

OCT . . . . . optical coherence tomography

Indeed, we often mark our progress in science by improvements in imaging.

— Martin Chalfie

1 Introduction

Contents

Optical endoscopes were first developed in 1806 and first used in a successful operation in the mid 19th century [1, 2]. Since then, optical endoscopy has enabled numerous applications in various fields such as aeronautical engineering, nuclear engineering, and, importantly, biomedicine. While smaller optical imaging probes allow visual access to otherwise unreachable anatomy, existing endoscopic modalities face fundamental limitations in scale miniaturization. Imaging through optical multimode fiber (MMF) may circumvent these limitations and stimulate the development of ultra-thin endoscopes to help advance our knowledge of fundamental biology and clinical medicine.

1.1 Optical Endoscopy in Biomedicine

Optical imaging is eminently useful in biomedicine by providing fast and minimally invasive visualization of biological structures and functions from histological to cellular levels. Among different imaging modalities such as tomography and microscopy, optical endoscopy allows confined "light conduction" between an observer (the proximal side) and remote tissue (the distal side), and facilitates the acquisition of anatomical or physiological information in natural biological environments. Since its invention and deployment, optical endoscopy has revolutionized the way healthcare providers conduct diagnosis and treatment of a wide range of diseases, and biologists interrogate organisms at multiple levels using animal models.

1.1.1 Applications and Trends

As shown in Fig. 1.1.1, different-sized endoscopes are designed according to their use. Clinical white light endoscopes for gastrointestinal and urological imaging are often several millimeters to more than a centimeter in size and have hundreds of micrometers tissue-level resolution. To access deeper anatomical locations through tortuous pathways, optical endoscopes with reduced footprint have been developed. For example, integration of a camera [3], microelectromechanical system (MEMS) mirrors [4], piezo-actuated vibrator [5], or mechanical torque-driven scanner [6] into the distal tip of probes for sample scanning leads to millimeter sizes that allow imaging within lumen structures such as nose, mouth, lung, heart, esophagus, stomach, colon, bladder, ureter, and cervix [7, 8]; Alternatively, scanning could be done proximally at the operator side, including optical fiber bundle [9, 10], multi-core optical fiber [11], and gradient index (GRIN) rod lens image relay [12], which reduce the probe diameter to less than a millimeter. This provides visual access to small airways, coronary arteries, pancreatic parenchyma, biliary ducts, and cortical neurons [7, 10, 13].

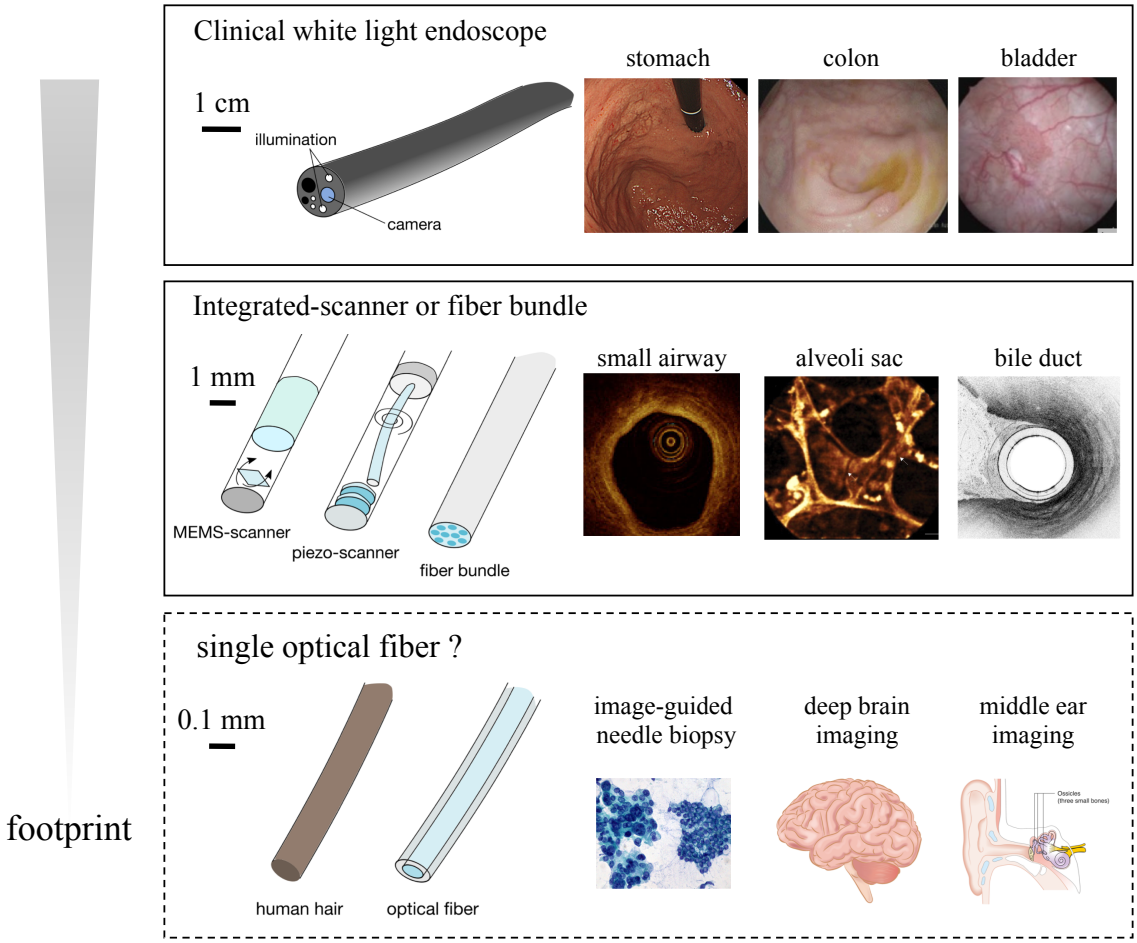

Figure 1.1.1: Clinical white light endoscopes allow examination of upper or lower gastrointestinal tracts on tissue level (Images from [14–16]) MEMS-based or integrated-scanner endoscopes can thread through small lumens in pulmonary or biliary systems for sampling lesions (Images from [17–19]) Moving forward, using single hair-thin optical fiber as stand-alone endoscopes has potential applications in image-guided needle biopsy, deep brain imaging, and middle ear imaging (Images from Pancreas FNA from Ed Uthman (licensed under CC BY-SA 2.0), Human Brain from Injurymap (licensed under CC BY-SA 4.0), and Diagram showing the parts of the middle ear from Cancer Research UK (licensed under CC BY-SA 4.0).) The scale bars signify the size variation of different imaging probes.

1.1.2 Unmet Medical Needs and Technical Limitations

Nevertheless, there remains clear needs that are not addressable with current endoscopic paradigms due to insufficiently small probe sizes: In neuroscience, a small enough probe

that avoids much damage to brain tissue and allows *in vivo* observation of deep brain neural activities with cellular resolution may provide valuable information; Middle or inner ear surgery may be much easier with visual access to the tympanic cavity through the eustachian tube while keeping the tympanic membrane minimally perturbed; Current needle biopsy is the gold standard for early stage cancer diagnosis. With on-site inspection by threading a small probe through the same needle channel, the sensitivity of biopsy may be much improved, and the cost, healing time, complication rate, procedure time may be well reduced. The hair-thin imaging probe may also open the opportunities of ovarian cancer screening and lymphatic imaging; Furthermore, while the on-site inspection of lesion at an early stage may be enabled, immediate image-guided therapy such as laser ablation, drug delivery, or deep photo-dynamic therapy (PDT) may also be possible.

In current endoscopic technologies, the imaging performance depends heavily on hardware specifications, resulting in fundamental limitations of probe miniaturization. For instance, integrating optics and electro-mechanics into a distal end is associated with complicated and high-cost fabrication processes, making it difficult to translate to the commercial market [5]; A small probe could be implemented by rotating a fiber with proximal mechanical torque, yet probe deformation may cause unbalanced torque and image distortion [7]; Imaging through fiber bundles or multicore fibers (MCFs) does not require integrated optoelectronics, but the separation of spatial channels leads to pixelation in images and poor resolution [20]; Using thin GRIN rod lens as image relay allows high-resolution *in vivo* imaging, but the rigid and short rod lens may introduce additional tissue injury during insertion [21], restricting the penetration depth. In light of the limitations, it would be implausible to implement a satisfactory thin imaging probe with high imaging performance and easy commercial availability.

Consequently, the unmet medical needs and technical limitations urge the development of a completely new optical endoscopic imaging method that could realize a probe with the following characteristics: Sub-millimeter footprint down to 10s of micrometers to

assure minimal invasiveness, micron-scale resolution to afford histological or cellular visualization, ideally real-time imaging speed to accommodate various clinical environments, preserved flexibility to support probe advancements through tortuous trajectory, and low fabrication cost as a disposable probe to omit sterilization and budget cost and time in clinical applications.

1.2 Imaging through Optical Multimode Fiber (MMF)

MMF is a cylindrical and flexible optical waveguide with diameter below few hundreds of micro-meters commonly used for communication over short distances, such as within a building or on a campus. Similar to traditional single mode fiber (SMF), MMF also has a single core, but in a larger size of tens to hundreds of micro-meters. Within the single core, MMF supports a large number of degrees of freedom (DOFs), or guided modes, propagating from input to output sides. Each mode has its corresponding pattern in space and serves as a spatial channel for encoding data stream. A multitude of modes can thus represent parallel data stream or multi-dimensional data, hence the high data-throughput of MMF. Compared to fiber bundles and MCF at equal DOFs, MMF has an overall smaller waveguide geometry attributed to its dense mode population (or number of spatial channels per unit core area) over the single core. Figure 1.2.1 shows an image of MMF, with core size in comparison to SMF. Using MMF for imaging applications may overcome the limitations of current optical endoscopes [22].

1.2.1 Potential of MMF in Endoscopy

The guided modes within MMF have different propagation speed and hence different arrival time at the output. In addition, the modes may exchange energy along the light propagation due to physical fiber deformations. These mechanisms lead to modal dispersion (different modes arrive at different time delays) and modal coupling (modes induce other modes during propagation). Therefore, the propagation through MMF generally scrambles

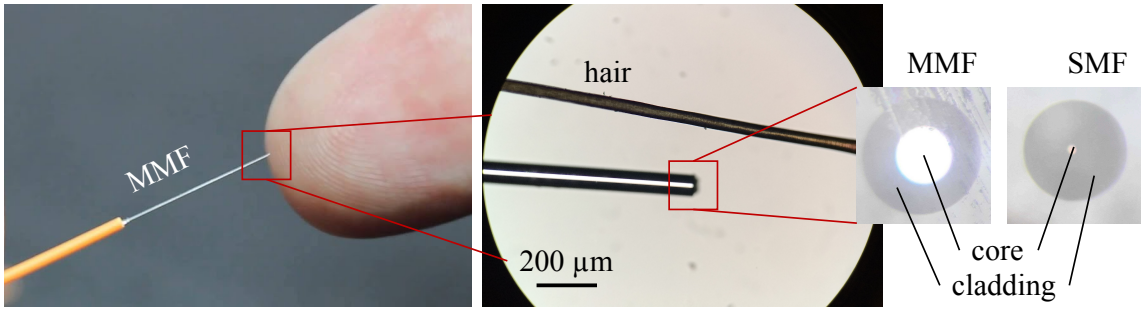

Figure 1.2.1: Optical fiber guides light within the core part due to total reflection at the cladding interface. MMF has a similar structure to SMF but a large core supporting a magnitude of modes. The diameter of MMF is typically few hundreds of micrometers.

an input light field in space, frequency/time, and polarization, resulting in a visually random speckle pattern at the output. As a result, MMF is typically considered as a complex medium with chaotic light transport process [23]. Nevertheless, this process is deterministic (the same input realization leads to the same output pattern) as long as the MMF maintains a static shape, where we can calibrate the transmission through MMF by measuring this output response. Based on the knowledge of transmission, controlling light and concentrating the energy at a spatial channel through MMF has been demonstrated [24, 25]. Details of MMF transmission will be discussed in Chapter 2.

Similar to data delivery with MMF in optical communications, the guided modes in MMF can also be used to encode the spatial features of a remote sample, where each mode carries partial information of the sample conformation. By harnessing the spatio-temporal modes, researchers have shown various methods for focusing and imaging through MMF without distal optics or distal scanning modules. For example, focusing through MMF based on physics principal of time reversal has been demonstrated a decade ago [25–27]. By configuring the input light to MMF, the generated focus through the MMF can be steered across remote samples for point by point image formation [28, 29]. The focal plane of imaging through MMF can be variable, and the light illumination coverage through MMF

improves with the distance of remote sample from the MMF [30]. Based on the paradigm, neural imaging with fluorescence labeling and muscle imaging with intrinsic contrast through MMF have been shown in animal models [21, 31, 32]. Side-view imaging through MMF can be simply achieved with engineered fiber termination [33]. Alternatively, imaging through MMF has also been achieved by numerical post processing without configuring the input light to MMF [20, 34]. These demonstrations reveal many advantages of imaging through MMF over existing optical endoscopes: single MMF could be transformed into a standalone probe with ultra-small footprint and variable working distance; the dense mode population renders a high spatial resolution and large field of view (FOV); MMF is commercially available at a low cost; imaging through MMF can support either forward- or side-viewing applications; and MMF is physically flexible. As illustrated in Fig. 1.1.1, the size of MMF could be orders of magnitude smaller than existing probes, making MMF-based endoscopes potential solutions to unmet medical needs. However attractive, imaging through MMF is technically challenging and still at the research and development phase.

1.3 Thesis Structure

To exploit MMF for endoscopic purposes, a deeper understanding of optical transmission through MMF is needed and may stimulate innovative computational imaging and sensing schemes. Toward this end, the thesis studies MMF characteristics and addresses major technical challenges in the following outline:

1. In Chapter 2, to study the light transport properties of MMF, we develop numerical simulations based on the theoretical model and setup experimental measurement systems for real-world MMF calibration. We unveil hidden structure behind the seemingly random fiber transmission. We also show a transpose symmetry of bi-directional fiber transmission imposed by optical reciprocity. The acquired knowledge helps us develop efficient MMF imaging and calibration methods.

2. In Chapter 3, to avoid limitations of active wave control and fluorescent labeling predominantly used in imaging through MMF [21, 28, 31, 35], we establish a computational imaging paradigm in a reflection mode, and demonstrate three-dimensional multi-modal label-free imaging with variable working distance and flexible trade-off between spatial resolution and FOV. The method streamlines the hardware system design and could have a speed advantage over active-wave-control approaches, and the label-free imaging will be desirable for clinical diagnostic applications.

3. in Chapter 4, to attain efficient multispectral calibration of MMF without repeated measurements at varying wavelength over a broad spectrum, we develop a parametric dispersion model that accounts for general dispersion beyond the first order model. We show an ultra-wide spectral correlation of the transmission through MMF after numerical dispersion compensation, which allows multispectral calibration with fewer measurements by more than an order of magnitude. The method may also benefit research in multi-color tissue imaging or wavelength multiplexing in optical communications.

4. In Chapter 5, to achieve depth imaging through MMF and observe stratified structures without using optical or mechanical scanning, we leverage the spatio-temporal modes of the MMF for encoding sample reflectivity at varying path length. We show a micrometer-scale axial resolution over a centimeter-long sensing range, which would otherwise require great hardware resources if a scanner were employed. The method also exemplifies a new design of light detection and ranging system.

5. In Chapter 6, to facilitate the development of a flexible MMF-based imaging probe, we demonstrate a MMF calibration method with proximal measurements. On-site MMF calibration without open distal access is imperative because imaging through MMF has a notorious intolerance to fiber perturbation, which is probably the most frequent criticism towards using MMF for endoscopic purposes [36]. Regardless of several attempts [22, 37–40], so far a robust method that allows complete MMF calibration in a practical

endoscopic setting is still lacking, and current MMF-based endoscopes require rigid geometries. The method avoids the drawbacks of previous attempts and may be a pragmatic solution to the enduring problem.

6. In Chapter 7, we briefly review each chapter and our contributions. Building on top of our achievements in this thesis, we also propose future prospect of practical imaging through MMF for endoscopic applications.

The key point to keep in mind, however, is that symmetry is one of the most important tools in deciphering nature's design.

— Mario Livio

2

Optical Transmission through MMF

Contents

Waveguide theory informs the underlying structure of transmission through MMF. Furthermore, the coherent transmission matrix (TM) is a convenient method to characterize

wave transmission through general media: The light propagation through MMF could be modeled by an empirical linear complex TM that summarizes the relationship between the input and output channels of spatial locations and polarization states, and a certain optical input state could be expressed as a column vector with elements as defined indexed channels [24]. In this way, light propagation through MMF is equivalent to the mathematical multiplication of the vector by the representative TM. We can thus study the MMF transmission physics through mathematical operations on the corresponding TM.

In addition to the waveguide theory, reciprocity is a fundamental principle of wave physics and directly relates to the symmetry in the transmission through a system when interchanging the input and output, regardless of transmission complexity. We demonstrate the optical reciprocal nature of a looped 1m-long step-index optical MMF by exploring its TM properties. These insights may inform the development of new imaging techniques through complex media and coherent control of waves in photonic systems. These results have been published and selected as Editor's Pick in APL Photonics [41].

2.1 Theoretical Model of MMF

MMF is a cylindrical waveguide, where the radial refractive index profile of the core part is a square wave function in step-index MMF (SI-MMF) or parabolic shape in graded-index MMF (GI-MMF). The numerical aperture (NA) of MMF is directly related to its acceptance angle of confined light due to the boundary condition between the core and cladding parts, and we can calculate the fiber NA

$$NA = \sqrt{n_{core}^2 - n_{clad}^2}, \tag{2.1}$$

where n_{core} and n_{clad} are the refractive indices of core and cladding parts, respectively. We can solve the Maxwell Equation of confined light in MMF and derive a set of propagation invariant modes (PIMs) with their profiles and propagation constants, β [42]. The PIMs maintain the same profile throughout propagation. While there are exact analytical solutions

for a SI-MMF, the modes in a GI-MMF are only approximated [43]. The well known V number (normalized frequency parameter) of a MMF is

$$V = \frac{2\pi}{\lambda} aNA, \tag{2.2}$$

where λ is the operating wavelength, and a is the fiber core radius. The V number allows us to estimate the total number of PIMs in a SI-MMF ($\sim V^2/2$) or GI-MMF ($\sim V^2/4$). In the following, we will show simulated theoretical modes in straight SI- and GI- MMF as well as their propagation constant distributions. In practice, when a MMF is bent, mode mixing effects have to be considered, where modes exchange energy, and the process can be simulated based on perturbation theory [30].

2.1.1 Modes and Modal Dispersion

Step-index MMF

We simulated 1m-long commercially available SI-MMF with 50 µm core size and 0.22 NA (e.g., FG050LGA, Thorlabs), operated at 1550 nm. There are 258 PIMs (close to 248 approximated based on the V number) with corresponding complex profile of Bessel functions of different orders indexed in l (orbital angular momentum) and m (radial oscillations). The exact PIMs have both azimuthal and radial polarization and can be grouped into EH and HE modes, and the propagation constants have a uniform distribution with bounds determined by the NA. The results are shown in Fig. 2.1.1, and the simulation code for this is available at <https://www.mathworks.com/matlabcentral/fileexchange/75327-mmf-simulation> or here. It is worth noting that while the Bessel functions are exact solutions, under weakly guiding condition, where the refractive index difference between the core and cladding is small, the PIMs can be approximated in linear horizontal (H) or vertical (V) polarization states, and become Laguerre-Gaussian (LG) functions [44], which are perhaps more commonly seen in literature. Essentially, the LG modes are the superposition of Bessel functions.

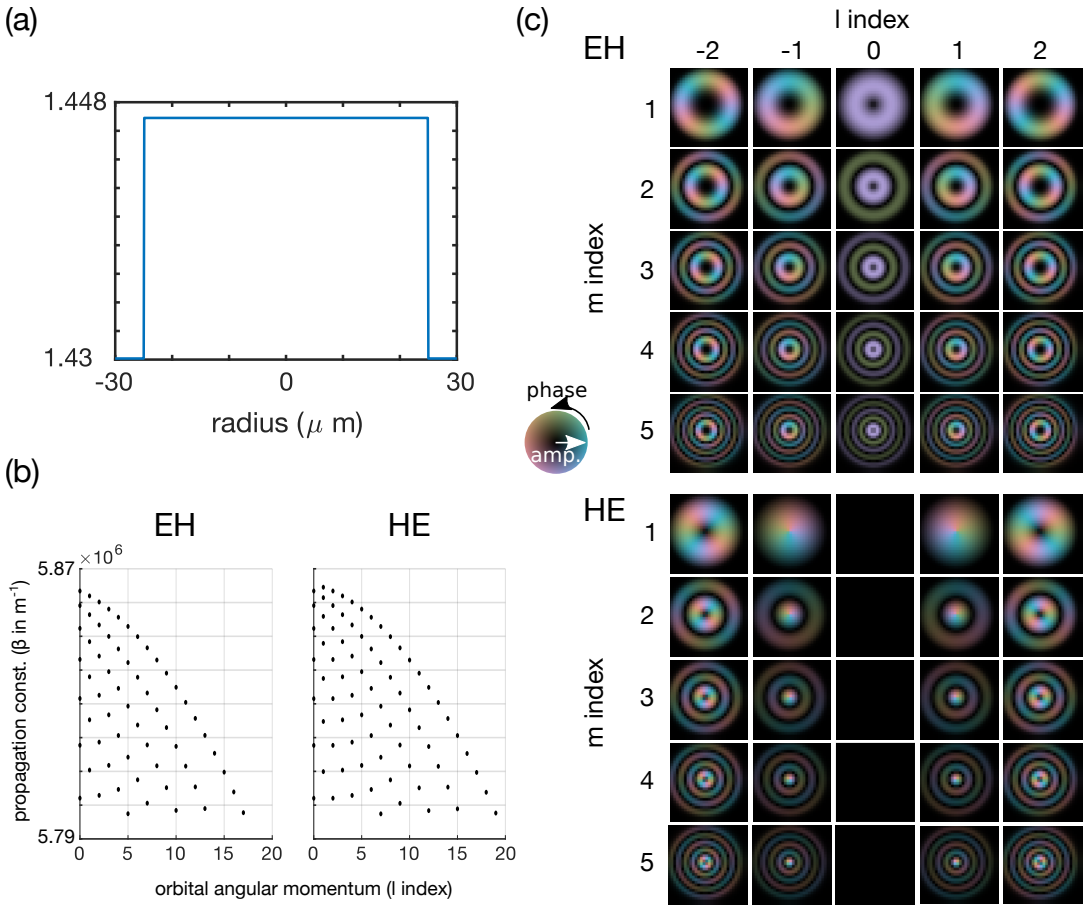

Figure 2.1.1: (a) Step refractive index profile of the 50 µm core size SI-MMF (b) Propagation constants of PIMs ordered in increasing l and m indices (c) The Bessel-function like profile of several theoretical PIMs. Polarization along the radial direction is plotted. The color map encodes complex values.

Graded-index MMF

We also simulated 1m-long commercially available GI-MMF with 62.5 µm core size and 0.275 NA (e.g., GIF625, Thorlabs) commonly used in optical communications (OM1), operated at 1550 nm. There are 306 PIMs (close to 303 approximated based on the V number) with 17 group indices and propagation constants having a discrete step-like distribution with bounds determined by NA. Each mode has a complex profile of Hermite-Gaussian (HG) functions of individual orders indexed in p (horizontal nodes) and

q (vertical nodes). The results are shown in Fig. 2.1.2. Since the modes in H and V polarization are identical, we only show the modes in H polarization. The simulation code for this is available at <https://www.mathworks.com/matlabcentral/fileexchange/78610-grin-mmf-simulation> or here.

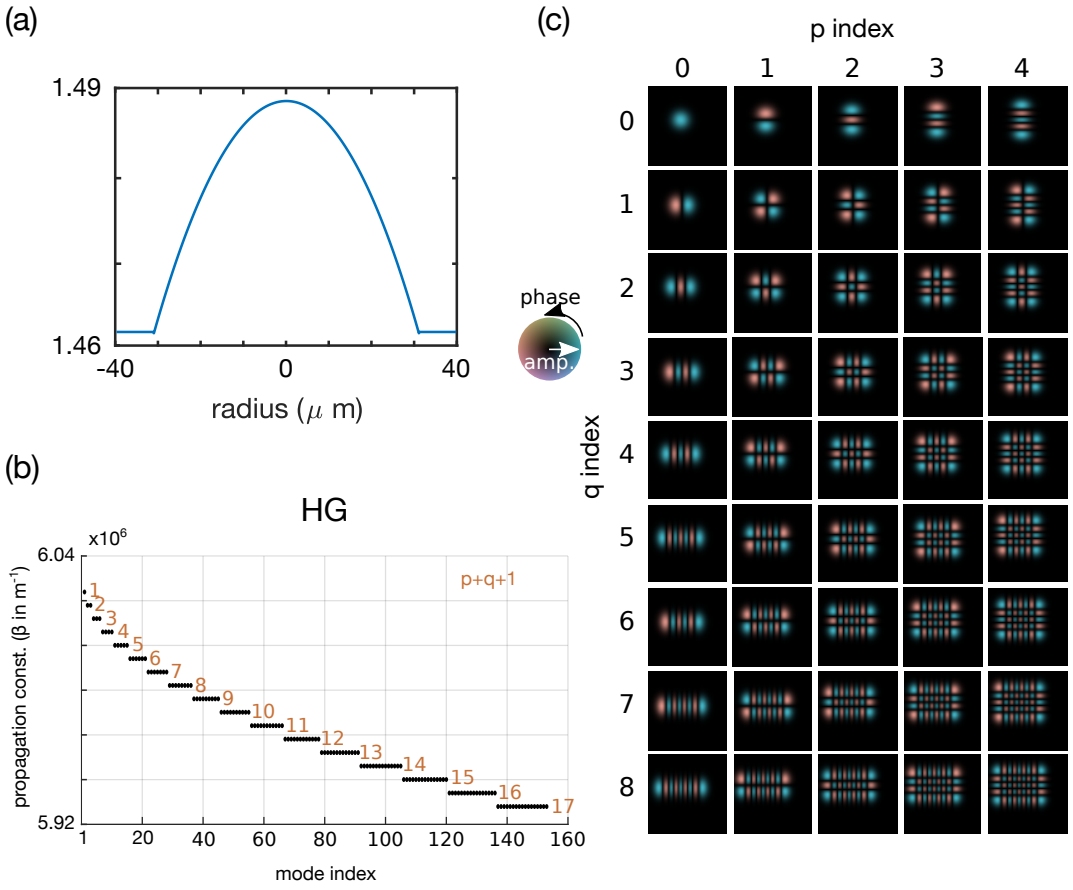

Figure 2.1.2: (a) Parabolic refractive index profile of the 62.5 µm core size GI-MMF (b) Propagation constants of PIMs ordered in increasing p and q indices (c) the Hermite-Gaussian-function like profile of several theoretical PIMs. H polarization is plotted.

2.1.2 Mode Mixing

The theoretical PIMs assume perfectly straight MMF with ideal refractive index profile. However, in practice, real-world MMF has distributed bending curvature, twisting, and

non-ideal refractive index due to fabrication imperfection. These physical deformations give rise to mode mixing effects of theoretical PIMs along the optical transmission through the MMF, where modes of similar propagation constants exchange energy during propagation. The local waveguide deformation provides necessary spatial frequency momentum that bridges the momentum difference between the wave-vector of different modes for momentum conservation. To simulate cross-coupling between any two PIMs, we followed the seminal work by Plöschner et al. [22, 45], and computed the amount of exchanged energy based on perturbation theory. Basically, the method calculates a spatial overlapping integral between any two PIMs across the MMF core. Since the theoretical PIMs are orthogonal to each other, the evaluated integral has a zero value when the MMF is straight. On the other hand, when the MMF is bent, a coordinate change is induced and leads to a non-zero value of the overlapping integral, and any two PIMs may couple to each other. The method is suitable for modeling loosely bent MMF, where the mode mixing effect is small, and there is mostly single coupling of light from one mode to another, which is often called a weakly coupling regime [46]. The method ignores birefringence effects induced by the fiber bending. Utilizing the method, we can simulate general MMF with arbitrary shape and bending curvature, and numerically study the transmission through MMF. An example is shown in Fig. 2.1.3, where the 1m-long SI-MMF is randomly bent in several locations, and we observe the outputs per different input realization. When the fiber is straight, the input PIM only experiences a phase delay, but the focus spot is scrambled due to modal dispersion; When the fiber is bent, the input PIM couples to different PIMs due to mode mixing, changing the output pattern.

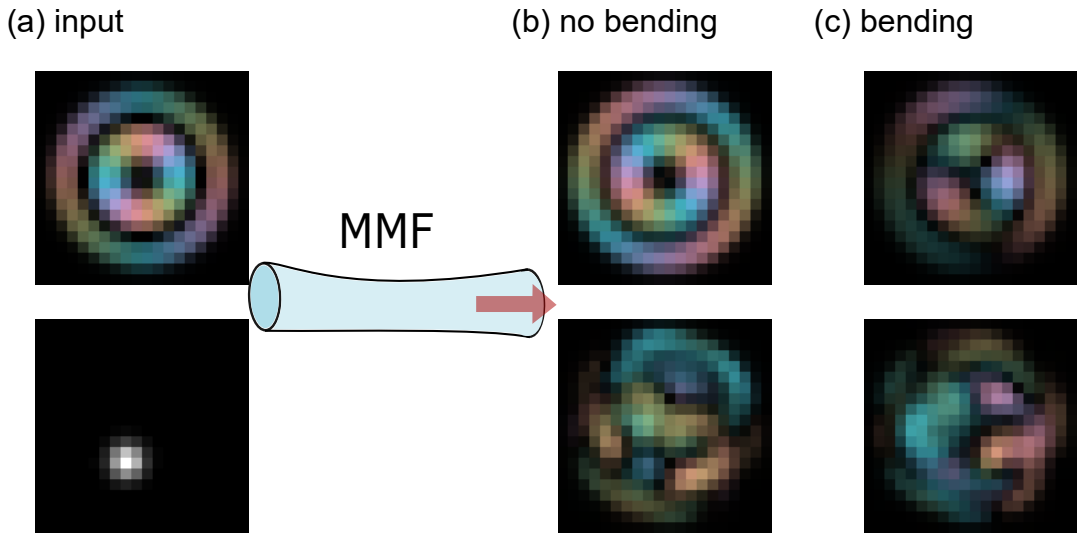

Figure 2.1.3: The output response of 1m-long, 50μm core, 0.22 NA SI-MMF to (a) PIM or focal spot input (b) before and (c) after bending of 30 ± 5 cm radius of curvature at 10 locations in random orientation along the fiber.

2.2 Transmission Matrix

While we can simulate transmission through MMF given the fiber geometry, it is almost impossible to acquire the exact shape of a real-world MMF and predict the corresponding complicated mode mixing effect in a microscopic scale. Fortunately, the optical transmission through a general medium from an input surface to an output surface can be expressed by a transmission matrix (TM), which is similar to a ray transfer matrix in geometrical optics but focuses only on the channel positions. This is illustrated in Fig. 2.2.1, where each element is a complex coefficient specifying the amplitude and phase evolution of the transmitted monochromatic field between the corresponding pair of input and output spatial channels. The spatial channels correspond to the sampling locations on the input and output surfaces, respectively, and are assumed to be sufficiently dense to correctly sample the electromagnetic fields. We can then express forward light transmission, $\mathbf{T}_{\text{fw}}$,

from the proximal to distal end as

$$\vec{t} = \mathbf{T}_{\text{fw}}\vec{s}, \tag{2.3}$$

where $\vec{t}$ and $\vec{s}$ are the vectorized representations of the distal output field and proximal input field, respectively. If $\vec{t}$ and $\vec{s}$ are ordered first by the spatial modes, and then by polarization, $\mathbf{T}_{\text{fw}}$ can be partitioned into four blocks,

$$\mathbf{T}_{\text{fw}} = \begin{bmatrix} \mathbf{T}_{\text{XH}} & \mathbf{T}_{\text{XV}} \\ \mathbf{T}_{\text{YH}} & \mathbf{T}_{\text{YV}} \end{bmatrix}, \tag{2.4}$$

where the subscripts X, Y and H, V denote two orthogonal polarization states on the distal and proximal side, respectively.

2.2.1 Measuring the Forward Transmission Matrix

To measure the experimental monochromatic $\mathbf{T}_{\text{fw}}$ of 1m-long MMF randomly coiled with a minimum radius of curvature of 23 mm, we set up a calibration system as shown in Fig. 2.2.2. A laser beam ($\lambda = 1550$ nm and linewidth < 100 kHz) was linearly polarized in a vertical (V) polarization state, reflected on a phase-only spatial light modulator (SLM, Model P1920-850-1650-HDMI, Meadowlark Optics) in the same polarization state, and then focused by using an objective lens (Mitutoyo Plan Apo NIR Infinity Corrected) with a numerical aperture (NA) of 0.4 into a 2.5 µm full-width at half maximum (FWHM) spot. An offset phase ramp was applied to the SLM to block unmodulated light. To uniformly probe all MMF guided modes, we first created on the proximal side a dense grid of 695 equally spaced illuminating foci sequentially generated by phase gradients on the SLM. We recorded the focus positions by placing a reflective surface on the focal plane and capturing the image of each focus with an InGaAs camera (OW1.7-VS-CL-LP-640, Raptor Photonics). An integrated focus grid image at each position is shown in the inset. From the image, we extracted the center of focus and created a proximal position map, where each position is an input spatial channel.

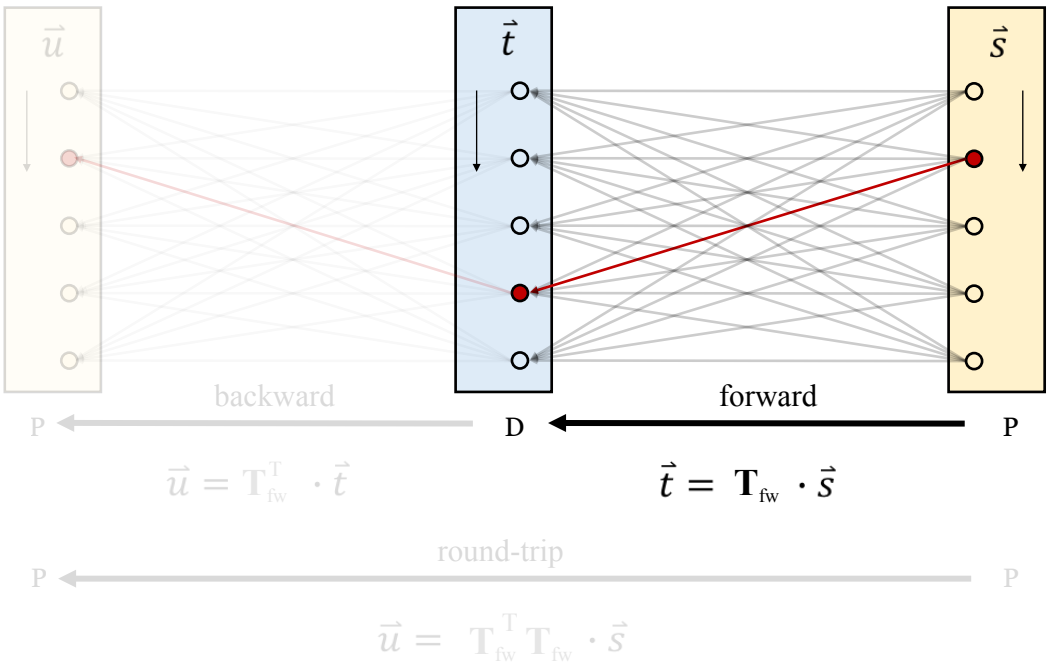

Figure 2.2.1: Schematic of forward TM characterizing transmission from the proximal (P) to distal (D) ends of a linear optical system. The vectors $\vec{s}$ and $\vec{t}$ represent complex fields with constituent spatial channels indexed by i and j on the proximal and distal ends, respectively. Each element a_{ji} of the forward TM describes the complex contribution of proximal input channel i to distal output channel j. The red arrows link a pair of spatial channels in the forward transmission.

Next, we coupled the focal spot through proximal input channels into the step-index MMF with 105 µm core diameter and a NA of 0.22 (FG105LCA, Thorlabs), which theoretically supports ∼550 guided modes per linear polarization [42]. The angular spectrum of the spot exceeded the NA of the MMF to ensure efficient population of high-order modes. On the MMF distal side, we imaged the speckle pattern exiting from output spatial channels with another identical objective and a tube lens (f = 30 cm) onto the camera with a vertically oriented, linear polarizer (LP) placed in front of it. A tilted plane reference wave, polarized by the same polarizer, interfered with the speckle pattern to record the complex image of the speckle pattern field through off-axis holography in the V polarization state. If we

consider the V polarizers at the proximal and distal sides as part of the system whose TM we are measuring, then $\mathbf{T}_{\mathrm{YV}} = \mathbf{T}_{\mathrm{VV}}$ and $\mathbf{T}_{\mathrm{fw}}$ becomes

$$\mathbf{T}_{\mathrm{fw}} = \begin{bmatrix} 0 & 0 \\ 0 & \mathbf{T}_{\mathrm{VV}} \end{bmatrix}. \tag{2.5}$$

To release digital storage burden, we down-sampled the complex image at a defined grid of 2637 positions. This procedure was repeated in an oversampling fashion for the dense focus grid. Rearranging column by column the ensemble of vectorized complex output images recorded over all input spatial channels constructed $\mathbf{T}_{\mathrm{fw}}$ representing the linear transformation of light traveling from the proximal facet to the distal facet. The TM was recorded in spot basis on both input and output channels. Due to the difference in the number of input and output sampling positions, $\mathbf{T}_{\mathrm{fw}}$ is a tall rectangular matrix.

2.2.2 Number of Modes

We quantified the number of guided modes within the MMF by performing singular value decomposition (SVD) on measured TMs, counting the singular values (SVs) above a threshold defined as 5% of the largest SV. As shown in Fig. 2.2.3, there are ∼500 populated modes in $\mathbf{T}_{\mathrm{fw}}$, but mode-dependent transmission loss is apparent. While the numbers are consistent with a theoretical maximum of 550, when inspecting the left singular vectors associated with decaying SVs, we find that the loss of guided power increases as a mode carries higher radial frequencies. We attribute the losses to coupling and detection of a single polarization state and to oversampling and interpolation of TM measurements.

2.2.3 Matrix Inversion

When a TM is unitary, we can apply Hermitian transpose as its true inverse, $\mathbf{T}^{-1} = \mathbf{T}^{\dagger}$. However, because experimental $\mathbf{T}_{\mathrm{fw}}$ is non-square, corrupted by noise, and close to singular, we approximated matrix inversion with Tikhonov regularization, $\mathbf{T}^{-1(\mathrm{tik})}$, with the regularization parameter, γ, chosen as 10% of the greatest SV. This is justified based

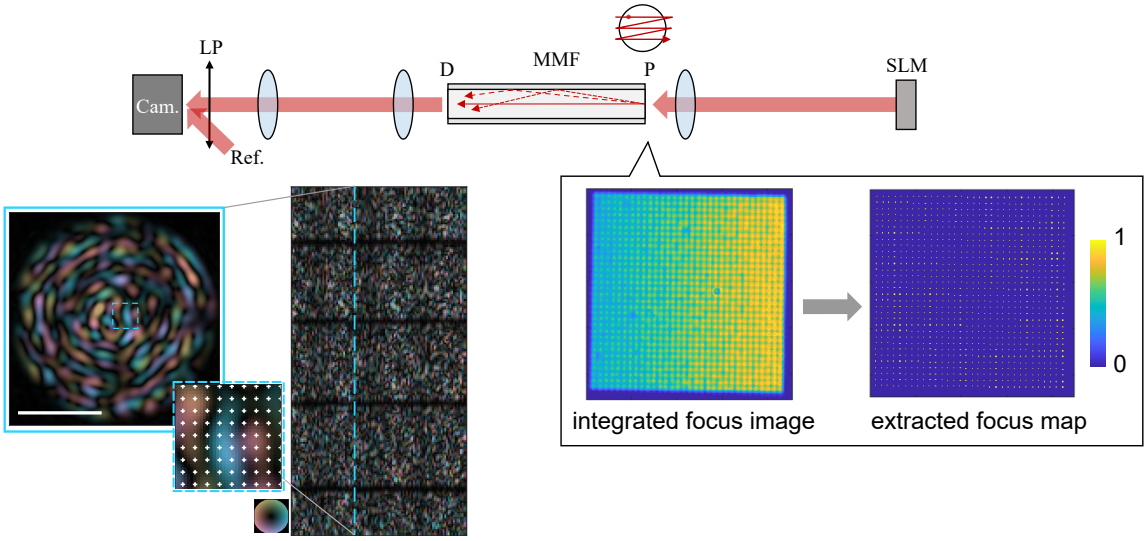

Figure 2.2.2: Measurement of the MMF forward TM, $\mathbf{T}_{\text{fw}}$. The fiber, although drawn as if it were straight, was in fact coiled in experiments. P: proximal, D: distal, LP: linear polarizer, Ref.: reference wave, Cam.: camera, M: gold-coated mirror, and BS: beam splitter. A focus was scanned by using the SLM across 695 positions distributed over the proximal focal plane. The reflection image of foci grid provides the position map of input channels. On the distal side, the output light field interfered with a reference wave on the camera and created a modulated image, which could be processed through Hilbert transformation into the complex amplitude of the output speckle. The image was down-sampled, as exemplified in the magnified inset, and rearranged into a column vector of $\mathbf{T}_{\text{fw}}$, with rows and columns indexed by the output and input channel positions, respectively. Only a subset of $\mathbf{T}_{\text{fw}}$ is shown.

on the L-curve method [47]. The product of $\mathbf{T}_{\text{fw}}$ with its regularized inverse is identical to the multiplication of a modified TM with its Hermitian transpose. The modification consists of rescaling each SV, σ, of the TM by $1/\sqrt{\sigma^2+\gamma^2}$ and is shown in dashed curves (labeled as "regularized") in Fig. 2.2.3.

2.2.4 Numerical Correction

To correct the physical misalignment between the MMF facet and the focal plane of the imaging system at the input/output sides, we developed an automated misalignment correction function that parameterizes and compensates the aberration based on an optimization approach following Plöschner et al [22]. We parameterized the physical

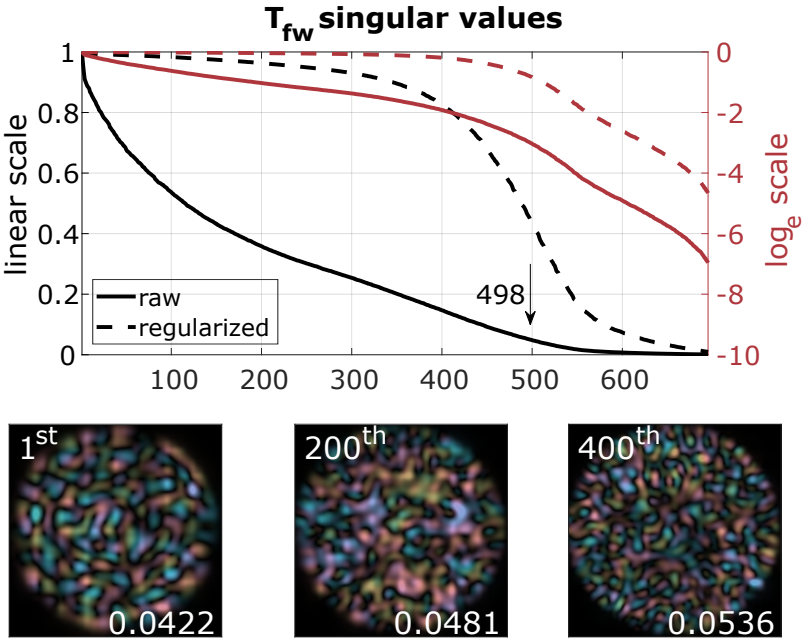

Figure 2.2.3: Singular values (SVs) of the measured TM in single-pass $\mathbf{T}_{\text{fw}}$. The black arrows indicate the number of modes with an SV above 5% of the TM's largest SV. The solid and dashed curves correspond to raw and regularized SVs, while black and red lines show linear and log scales, respectively. Three examples of singular modes are visualized for each configuration by reshaping singular vectors to 2D images and numerically interpolating the images for better visual appearance. The averaged normalized radial frequency (0.5 cycles/radius) of the power spectral density of each mode is indicated in the lower-right corner. High-order modes are associated with higher radial frequency and are subject to increased loss.

misalignment of the input/output considering 8 variables: To address the phase mismatch, we applied a two-dimensional (2D) phase term constituted by Zernike polynomials in the recording space of the spatial channels, as shown in Fig. 2.2.4. This corresponds to a diagonal phase-only matrix left-multiplied to the TM to be corrected. The Zernike orders correspond to 2D tilts, defocus, and 2D astigmatisms (5 variables); To register the positional shifts, we applied another phase term with 2D tilts and defocus in the

Fourier space of the spatial channels of the TM (3 variables), as this is the same as the lateral and axial translation of the observation coordinates. The correction is equivalent to convolving the spatial channels with a complex and offset point spread function. In the matrix formalism, the correction to the input/output channels is a further right-/left-multiplication of the TM with a Toeplitz matrix. To optimize for the 8 variables, we defined a scalar metric quantifying the matrix energy close to the main diagonal when representing experimental TMs in theoretical PIM basis.

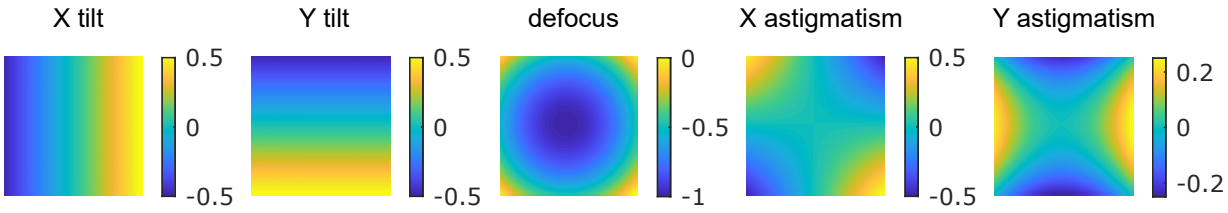

Figure 2.2.4: First 5 Zernike modes for numerical correction to aberration.

2.3 Sparsity in MMF Transmission

The TMs of MMF in the experimental recording basis is typically dense and chaotic. However, a TM can also be linearly transformed into a different space spanned by an arbitrary set of orthogonal spatial functions. For instance, we could project the TM into a modal representation with theoretical PIMs of the MMF as the spatial functions. Since a loosely bent MMF is in a weak coupling regime, coupling may be confined between PIMs of similar propagation constants, thereby providing an advantageous sparsity in the transformed TM that we can utilize to develop efficient imaging paradigms and calibration methods. In the following, we measured forward TMs of a 1m-long SI-MMF and a 1m-long GI-MMF in the spot basis and transformed the TMs into PIM representations.

2.3.1 Modal Projection

To transform the basis for TM representation, we first calculated the set of theoretical PIMs according to the MMF's specifications and at the experimental spatial sampling rate. We ordered the PIMs in an increasing in-plane momentum (thus a decreasing propagation constant) and grouped the vectorized PIMs in a complex matrix $\mathbf{E}$. Since the spatial sampling rate is different in the MMF input and output space, we repeated the processes and acquired $\mathbf{E}_{\text{in}}$ and $\mathbf{E}_{\text{out}}$, respectively. Theoretically, to represent the input and output of the TM in the PIM set, $\mathbf{T}_{\text{mode}}$, we should calculate $\mathbf{E}_{\text{out}}^{\dagger}\mathbf{T}\mathbf{E}_{\text{in}}$. However, due to the physical misalignment between the focal plane of the imaging system and the fiber facet, direct basis transformation results in random interference of the PIMs and bury the hidden TM structure. Appropriate correction matrices, $\mathbf{C}_{\text{in}}$ and $\mathbf{C}_{\text{out}}$, compensating the misalignment on both input and output sides are necessary to complete the modal projection [22, 48]. Using the developed numerical correction technique, we can generate the correction matrices by parameterizing the misalignment. Since a PIM exchanges energy with others with similar propagation constants under the weak coupling regime, we expected the TM in modal representation to have energy concentrated in the diagonal. Therefore, we aimed to optimize for correction to misalignment by maximizing on-diagonal energy of TM in modal representation

$$\overline{\mathbf{C}}_{\text{in}}, \overline{\mathbf{C}}_{\text{out}} = \underset{\mathbf{C}_{\text{in}},\mathbf{C}_{\text{out}}}{\arg\max} \frac{||diag.(\mathbf{E}_{\text{out}}^{\dagger}\mathbf{C}_{\text{out}}\mathbf{T}\mathbf{C}_{\text{in}}\mathbf{E}_{\text{in}})||_F}{||\mathbf{E}_{\text{out}}^{\dagger}\mathbf{C}_{\text{out}}\mathbf{T}\mathbf{C}_{\text{in}}\mathbf{E}_{\text{in}}||_F}, \tag{2.6}$$

where F is the Frobenius norm, and the overline denotes optimal quantities. After the optimization process, we have the TM in modal representation $\mathbf{T}_{\text{mode}} = \mathbf{E}_{\text{out}}^{\dagger}\overline{\mathbf{C}}_{\text{out}}\mathbf{T}\overline{\mathbf{C}}_{\text{in}}\mathbf{E}_{\text{in}}$.

2.3.2 Step-index MMF

We measured the forward TM of a randomly coiled 1m-long SI-MMF with 50 µm core and NA 0.22 at 1550 nm fixed on optic table in the spot basis, as shown in Fig. 2.3.1. The TM in the original basis is completely random and one can hardly see any structure.

Nevertheless, after the modal projection, we can see that the mode mixing effect due to MMF deformation is confined to modes of similar propagation constants to preserve the momentum. Also, more energy is populated in the low order modes, which may be attributed to the more efficient light coupling into low order modes on the input side and higher propagation loss in the high order modes.

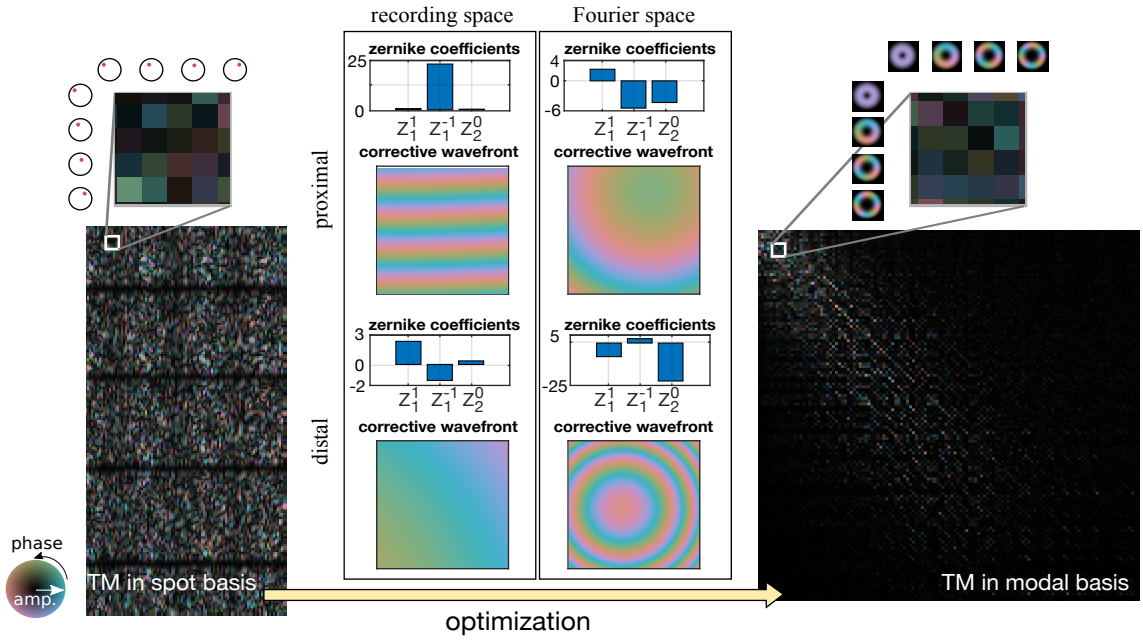

Figure 2.3.1: (a) Experimental TM in spot basis representation. (b) in PIM basis representation.

2.3.3 Graded-index MMF

We measured the forward TM of a randomly coiled 1m-long GI-MMF with 62.5 µm core and NA 0.275 at 1550 nm fixed on optic table in the spot basis, as shown in Fig. 2.3.2. Similar to the SI-MMF, the TM in the original basis is completely random. Nevertheless, after the modal projection, we can see that the mode mixing effect due to MMF deformation is confined to modes in the same mode group of the same propagation constants. The momentum gap between modes in different groups is large enough to prevent inter-group

coupling, leading to block diagonal matrix structure of the TM. This highlights the main difference in the transmission between a GI-MMF and SI-MMF: The dispersion can be minimized for pulse delivery in GI-MMF when launched in a certain group, where energy will remain in the same group of identical propagation speed; On the other hand, SI-MMF may have a strong modal dispersion effect, and energy can be continuously diffuse to modes of various propagation speed during transmission through the fiber.

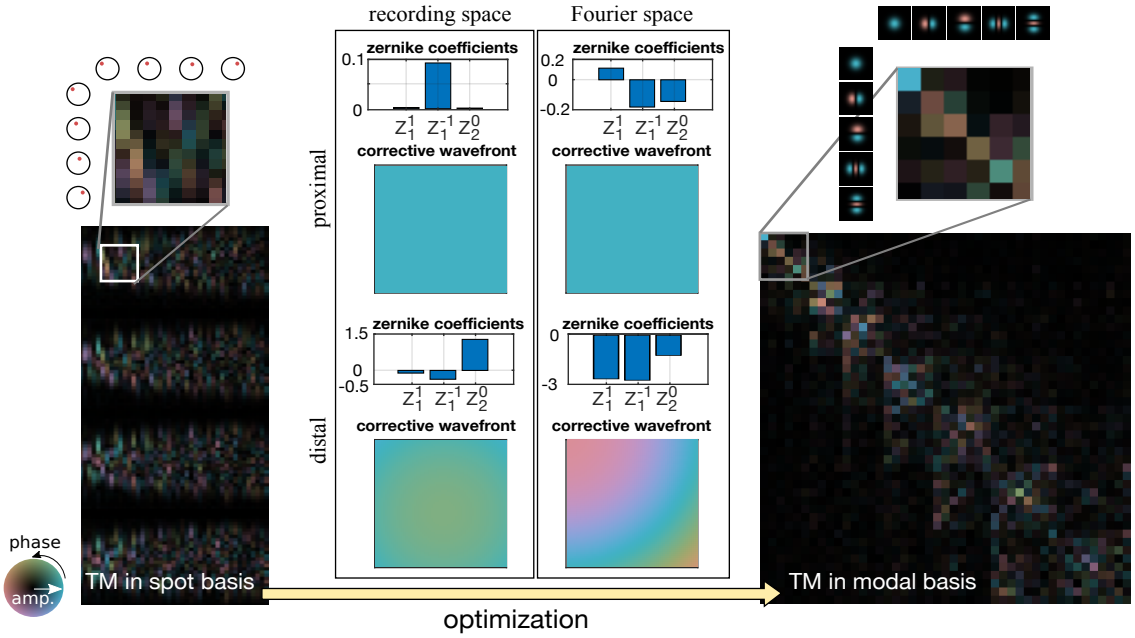

Figure 2.3.2: (a) Experimental TM in spot basis representation. (b) in PIM basis representation.

2.4 Optical Reciprocity in MMF Transmission

The bi-directional transmission through photonic systems is governed by the universal Lorentz reciprocity (or the Helmholtz reciprocity), which states that light propagating along a reversed path experiences the exact same transmission coefficient as in the forward direction, independent of the path complexity [49, 50] or the presence of loss [51–53]. In the linear regime, this suggests a definite relation, or symmetry, between the forward and the

backward transmission when interchanging the source and detector. This symmetry not only underlies the behavior of common optical components, such as polarizers, beam splitters, and wave-plates, but also engenders surprising physical phenomena in complex systems such as coherent backscattering (or weak localization) and Anderson localization [54, 55]. Optical phase conjugation is a well-known consequence of this symmetry in loss-free systems, whereby an original light distribution is replicated by reversing the propagation direction of the detected field while conjugating its wave-front. Digital optical phase conjugation (DOPC) has been well established for focusing and imaging through complex or disordered media, including MMFs [25, 56–58]. However, the more general underlying transmission symmetry of bi-directional light transmission through complex systems and its implications have not been explicitly demonstrated and discussed.

Here, we investigate MMF transmission properties using a monochromatic coherent TM formalism [24, 59] and experimentally demonstrate the transpose symmetry between the forward and backward TMs in this complex medium imposed by general optical reciprocity. The TM description is a subpart of the common scattering matrix formalism [24, 60], and offers a simpler framework that decouples the input and output channels. The gained insights are readily applicable to general electromagnetic transport in complex and disordered media.

In section 2.2, we described the forward TM of a MMF. As illustrated in Fig. 2.4.1, the backward light transmission from the distal to proximal end can be written as

$$\vec{u} = \mathbf{T}_{\mathrm{bw}}\vec{t}, \tag{2.7}$$

where $\vec{u}$ and $\vec{t}$ are the proximal output field and distal input field, respectively. According to the reciprocity theorem, light propagating along the reversed path between the input and output will experience the same transmission coefficient as in the forward direction. In the context of Jones matrices, which describe the relation between the polarization states of the input and the output field propagating through an optical system, de Hoop's notion of reciprocity manifests as a transpose relationship between the Jones matrices

describing forward and reverse transmissions. By analogy with the Jones matrix formalism, when interchanging the input and output spatial channels of the medium, reciprocity instructs that $\mathbf{T}_{\mathrm{bw}}$ is the transpose of $\mathbf{T}_{\mathrm{fw}}$,

$$\mathbf{T}_{\mathrm{bw}} = \mathbf{T}_{\mathrm{fw}}^{\mathrm{T}} = \begin{bmatrix} \mathbf{T}_{\mathrm{XH}}^{\mathrm{T}} & \mathbf{T}_{\mathrm{YH}}^{\mathrm{T}} \\ \mathbf{T}_{\mathrm{XV}}^{\mathrm{T}} & \mathbf{T}_{\mathrm{YV}}^{\mathrm{T}} \end{bmatrix}, \tag{2.8}$$

where the superscript T indicates the regular matrix transpose. In addition, since sequential light transmission is modeled as TM multiplication, the round-trip transmission through the same medium, $\mathbf{T}_{2\mathrm{X}}$ (light transmits to and is reflected from the distal side; then, it travels back to the proximal side), equals the product of $\mathbf{T}_{\mathrm{bw}}$ and $\mathbf{T}_{\mathrm{fw}}$,

$$\mathbf{T}_{2\mathrm{X}} = \mathbf{T}_{\mathrm{bw}}\mathbf{T}_{\mathrm{fw}} = \mathbf{T}_{\mathrm{fw}}^{\mathrm{T}}\mathbf{T}_{\mathrm{fw}}, \tag{2.9}$$

making $\mathbf{T}_{2\mathrm{X}}$ a transpose symmetric matrix,

$$\mathbf{T}_{2\mathrm{X}} = \begin{bmatrix} \mathbf{T}_{\mathrm{XH}}^{\mathrm{T}}\mathbf{T}_{\mathrm{XH}} + \mathbf{T}_{\mathrm{YH}}^{\mathrm{T}}\mathbf{T}_{\mathrm{YH}} & \mathbf{T}_{\mathrm{XH}}^{\mathrm{T}}\mathbf{T}_{\mathrm{XV}} + \mathbf{T}_{\mathrm{YH}}^{\mathrm{T}}\mathbf{T}_{\mathrm{YV}} \\ \mathbf{T}_{\mathrm{XV}}^{\mathrm{T}}\mathbf{T}_{\mathrm{XH}} + \mathbf{T}_{\mathrm{YV}}^{\mathrm{T}}\mathbf{T}_{\mathrm{YH}} & \mathbf{T}_{\mathrm{XV}}^{\mathrm{T}}\mathbf{T}_{\mathrm{XV}} + \mathbf{T}_{\mathrm{YV}}^{\mathrm{T}}\mathbf{T}_{\mathrm{YV}} \end{bmatrix} = \mathbf{T}_{2\mathrm{X}}^{\mathrm{T}} \tag{2.10}$$

Of note, the two on-diagonal blocks are self-transpose-symmetric and the two off-diagonal blocks are instead the transpose of each other.

2.4.1 Measuring the Round-trip Transmission Matrix

To experimentally verify Eqs. 2.8 and 2.9, we measured the round-trip TM, $\mathbf{T}_{2\mathrm{X}}$, of the MMF, using the setup shown in Fig. 2.4.2. We again sequentially coupled light into the MMF from the proximal end through the same set of input spatial channels. On the distal side, we replaced the camera used for measuring in the forward transmission with a gold-coated mirror to reflect the light back into the MMF. The same V linear polarizer, previously in front of the camera and now in front of the gold-coated mirror, was necessary to maintain the identical $\mathbf{T}_{\mathrm{fw}}$ and avoid polarization crosstalk. In general, the spatial and polarization DOFs are coupled through mode mixing during light propagation in the MMF, and the MMF output polarization states are different from the input polarization state

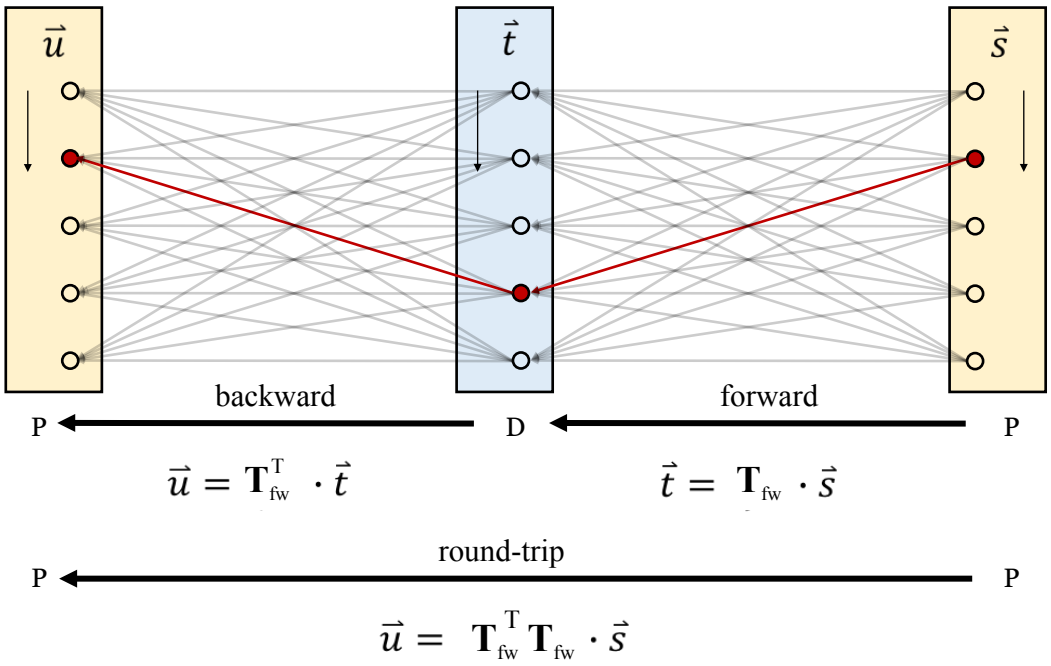

Figure 2.4.1: Schematic of forward and backward TMs characterizing transmission between the proximal (P) and distal (D) ends of a linear optical system. The round-trip transmission from and to the proximal end is unfolded to reveal the hidden transpose symmetry when flipping the direction of an optical path (gray arrows) linking a pair of spatial channels. The red arrows link a pair of spatial channels in the forward and backward transmission. Owing to reciprocity, both directions feature the same transmission coefficient, yet they correspond to transposed elements in the corresponding TMs, with interchanged row and column indices.

[61]. With the distal and proximal V linear polarizers, we measure the transmission from a V linear input polarization state into a V linear output polarization state, both for the forward and the double-pass TMs. $\mathbf{T}_{2\text{X}}$ of Eq. 2.10 simplifies in this case to

$$\mathbf{T}_{2\text{X}} = \begin{bmatrix} 0 & 0 \\ 0 & \mathbf{T}_{\text{VV}}^{\text{T}} \mathbf{T}_{\text{VV}} \end{bmatrix}. \tag{2.11}$$

On the proximal side, we recorded the round-trip transmission by decoupling its path from the illumination with a non-polarizing beam splitter. To preserve the symmetry between the illumination and the detection configurations and to obtain a square matrix $\mathbf{T}_{2\text{X}}$, we sampled the recorded output fields at the 695 positions defined by the input focus positions

(the foci map). Furthermore, to mitigate specular reflections at both the distal and proximal facets, wedge prism mounting shims (SM1W1122, Thorlabs) filled with index-matching gel (G608N3, Thorlabs) were used to cover both facets for measurements of forward and double-pass TMs. Intriguingly, the round-trip measurements through individual proximal spatial channels allow us to observe the coherent backscattering effect, which guarantees constructive interference in pairs of time-reversed optical paths, and thus, light is statistically twice as likely to exit through the same spatial channel that it used to couple into the fiber than through any other output channel [62]. In the TM formalism, this corresponds to a ratio of two between the mean intensities of the main diagonal and off-diagonal elements in $\mathbf{T}_{2X}$, as plotted in Fig. 2.4.2. Mathematically, if we assume that the elements in $\mathbf{T}_{fw}$ feature independent real and imaginary parts following identical normal distributions, then Eq. 2.9 states that $\mathbf{T}_{2X}$ is the same as a pseudo-covariance matrix (or relation matrix) of proper complex random vectors [63, 64], resulting in the factor of two due to Gaussian statistics.

In our experiments, we used a single polarization for illumination and detection to avoid the experimental complexity of measuring polarization-resolved TMs [22]. Furthermore, the X and Y polarization states at the distal side were identical to the H and V polarizations at the proximal side. Measuring the round-trip TM without the distal V polarizer would still result in a transpose symmetric matrix $\mathbf{T}_{2X}$, but the coupling between the polarization states would create a second term $\mathbf{T}_{HV}^{T}\mathbf{T}_{HV}$. Hence, the distal V polarizer was required when measuring the round-trip TM to be able to relate $\mathbf{T}_{2X}$ to the measured $\mathbf{T}_{VV}$ of $\mathbf{T}_{fw}$. The polarization DOF simply extends the DOFs of the spatial modes, and in analogy to the partition of the TM into the four polarization blocks of Eq. 2.9, we could also partition $\mathbf{T}_{VV}$ into any two subsets of input and output spatial modes. Thus, $\mathbf{T}_{VV}$ can likewise be defined as being composed of four blocks, which express the transmissions from the two input subsets to the two output subsets. The measured round-trip matrix $\mathbf{T}_{VV}^{T}\mathbf{T}_{VV}$ contains two on-diagonal blocks that are self-transpose-symmetric and two off-diagonal blocks that are the transpose of each other. By extension, the experimental verification of

the symmetry relation for a single polarization state holds for any combination of spatial channels and polarization states and holds without loss of generality.

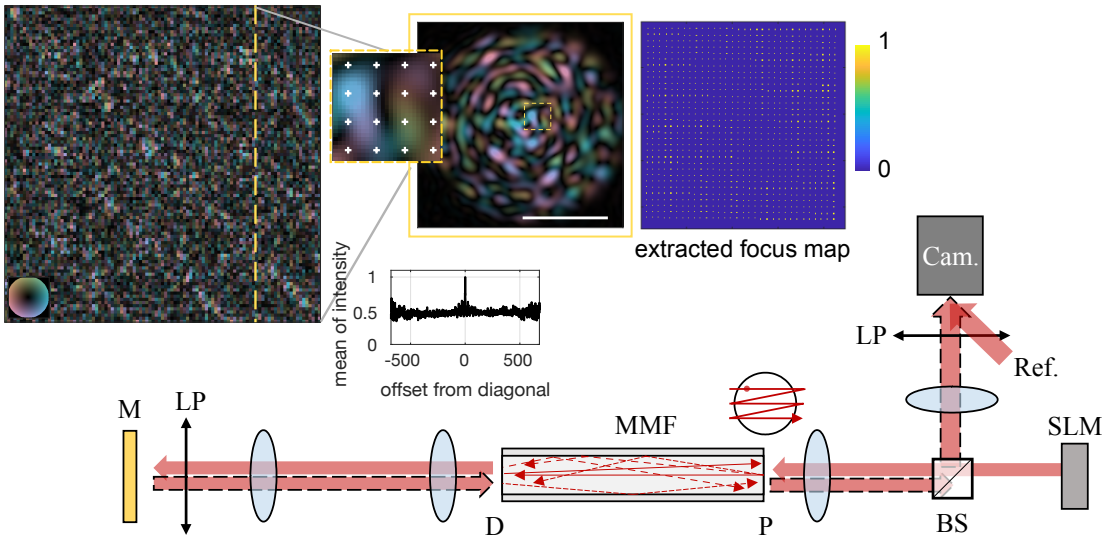

Figure 2.4.2: For round-trip $\mathbf{T}_{2X}$ measurements, the camera at the distal side was replaced by a mirror, and the returning light was directed by using a non-polarizing beam splitter to the same camera for holographic recording. The complex image of the round-trip output speckle was down-sampled at the 695 positions of the input foci grid (inset), resulting in a square matrix. A subset of $\mathbf{T}_{2X}$ is shown, the vertical dashed line indicates the vector arranged as an image of the facet, and the yellow inset shows sampling locations as white markers. The color maps encode complex values, and the scale bars in the insets are 50 µm. The plotted trace is the average intensity of matrix elements with varying offset from the diagonal, and the ratio of two between the main diagonal and the off-diagonal reveals the coherent backscattering in the MMF.

2.4.2 Symmetry in Round-trip Measurement

We set out to verify the anticipated transpose symmetry within the round-trip TM $\mathbf{T}_{2X}$, as stated in Eq. 2.10. This property should be self-sustained and independent of $\mathbf{T}_{fw}$. Physical misalignment between the defined input surface to the MMF and the image recording plane at the proximal end introduces a phase mismatch and relative shifts that need to be compensated to reveal the underlying transpose symmetry. This is similar to misalignment issues in common DOPC systems [65]. The Zernike coeffcients

parameterizing the physical misalignment were determined by minimizing the error $|\mathbf{T}_{2X}^{'T} - \mathbf{T}_{2X}^{'}|2$, where $\mathbf{T}_{2X}^{'}$ is the corrected $\mathbf{T}_{2X}$ and $|\cdot|^2$ is the squared Frobenius matrix norm. Without correction, the initial error, normalized by $|\mathbf{T}_{2X}|^2$, was 200%. With correction, the normalized error was reduced to 23%. For comparison, we found a 15% residual error when computing the normalized squared Frobenius norm of the difference between two sequentially measured round-trip TMs of the identical MMF transmission. To investigate transpose symmetry, we verified the diagonal localization in the product of the matrix by its inverse transpose. The product of the uncorrected $\mathbf{T}_{2X}$ with its Tikhonov regularized transpose matrix inversion $\mathbf{T}_{2X}^{-T(tik)}$ is a chaotic matrix due to the disordered interference between populated modes caused by the physical misalignment (Fig. 2.4.3). However, after applying the correction, the product of $\mathbf{T}_{2X}^{'}$ with $\mathbf{T}_{2X}^{'-T(tik)}$ became close to the identity matrix, with the integrated on-diagonal energy over the total matrix energy improving from 0.24% to 43.5%. As benchmark, the same metric applied to a perfectly symmetric TM, $(\mathbf{T}_{2X}^{'T} + \mathbf{T}_{2X}^{'})/2$, resulted in 59.2% on-diagonal energy, limited by the regularized matrix inversion. These results show that the phase-corrected round-trip TM matches its transpose, thus demonstrating its transpose symmetry.

2.4.3 Reciprocity in Bi-directional Transmission

With the corrected $\mathbf{T}_{2X}$, we proceeded to verify the transpose relationship between the forward and backward TMs, as stated in Eq. 2.8. For experimental convenience, instead of directly comparing $\mathbf{T}_{bw}$ and $\mathbf{T}_{fw}$, we assumed that $\mathbf{T}_{bw} = \mathbf{T}_{fw}^{T}$ and worked with $\mathbf{T}_{fw}^{T}\mathbf{T}_{fw}$ and $\mathbf{T}_{2X}^{'}$, avoiding the complexity of directly measuring $\mathbf{T}_{bw}$. Similar to correcting the round-trip measurements, we had to compensate the physical misalignment between the recording plane on the distal side for measuring $\mathbf{T}_{fw}$ and the gold-coated mirror used in measuring $\mathbf{T}_{2X}$. In a similar way to how we corrected $\mathbf{T}_{2X}$, we applied phase terms to the recording and Fourier spaces of the output spatial channels of $\mathbf{T}_{fw}$. However, in this case, we aimed to minimize the error $|\mathbf{T}_{2X}^{'} - \mathbf{T}_{fw}^{'T}\mathbf{T}_{fw}^{'}|^2$, where $\mathbf{T}_{fw}^{'}$ is the corrected $\mathbf{T}_{fw}$.

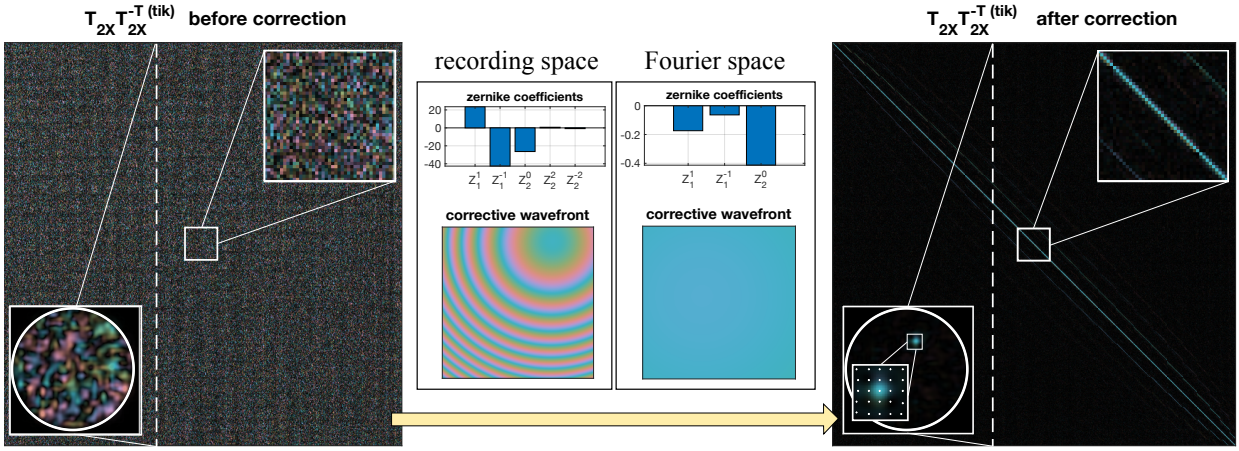

Figure 2.4.3: Transpose symmetry of $\mathbf{T}_{2X}$ before and after correction for misalignment at the proximal end. The phase mismatch and positional shifts are described as Zernike polynomials in the recording and Fourier space, respectively, and the amplitude of each mode is iteratively updated to minimize the difference between $\mathbf{T}'_{2X}$ and $\mathbf{T}'^{T}_{2X}$. Higher order Zernike polynomials are found to be negligible after additional trials. Using a Newtonian-based optimizer, the normalized error converges from 200% to 23% after the phase mismatch and positional shift corrections, each within tens of iterations. The horizontal and vertical tilts and defocus in the recording space are the dominant factors. A column in the products of $\mathbf{T}_{2X}$ and $\mathbf{T}_{2X}^{-T(tik)}$ before and after phase correction is selected, converted back into 2D coordinates, and smoothed by interpolation to illustrate constructive interference at the corresponding proximal spatial channel when using corrected TMs. The offset diagonals on both sides of the main diagonal are due to oversampling during TM measurement, as visualized by indicating the proximal sampling positions.

Figure 2.4.4 shows that the misalignment, characterized by the amplitude of the Zernike polynomials, was quite different from that encountered in $\mathbf{T}_{2X}$. Without correction to $\mathbf{T}_{fw}$, the initial error, normalized by $|\mathbf{T}'_{2X}|^2$, was 101% and the product of $\mathbf{T}'_{2X}$ and $(\mathbf{T}_{fw}^{T}\mathbf{T}_{fw})^{-1(tik)}$ appeared far from a diagonal matrix, implying low resemblance between $\mathbf{T}'_{2X}$ and $\mathbf{T}_{fw}^{T}\mathbf{T}_{fw}$. Clearly, the random background denotes that the physical misalignment caused undesired interference over all spatial channels. Crucially, the normalized error reduced to 27.7% after correction, which is again close to the experimental benchmark of 15%. Additionally, the resultant product closely resembled the identity matrix, with its integrated on-diagonal energy over the total matrix energy improving from 0.27% to 36.6%. The product of $\mathbf{T}'_{2X}$ with its regularized inverse reached 56.8% on-diagonal energy. Therefore, we conclude

that $\mathbf{T}'_{2X}$ and $\mathbf{T}'^{T}_{fw}\mathbf{T}'_{fw}$, at least as measured in a single polarization state, are identical to each other, as stated in Eq. 2.9, which implies that the backward transmission $\mathbf{T}_{bw}$ is the same as $\mathbf{T}^{T}_{fw}$, as described in Eq. 2.8. This provides evidence of general optical reciprocity and the ensuing transpose symmetry for transmission through a MMF, which serves as a convenient model for general complex media.

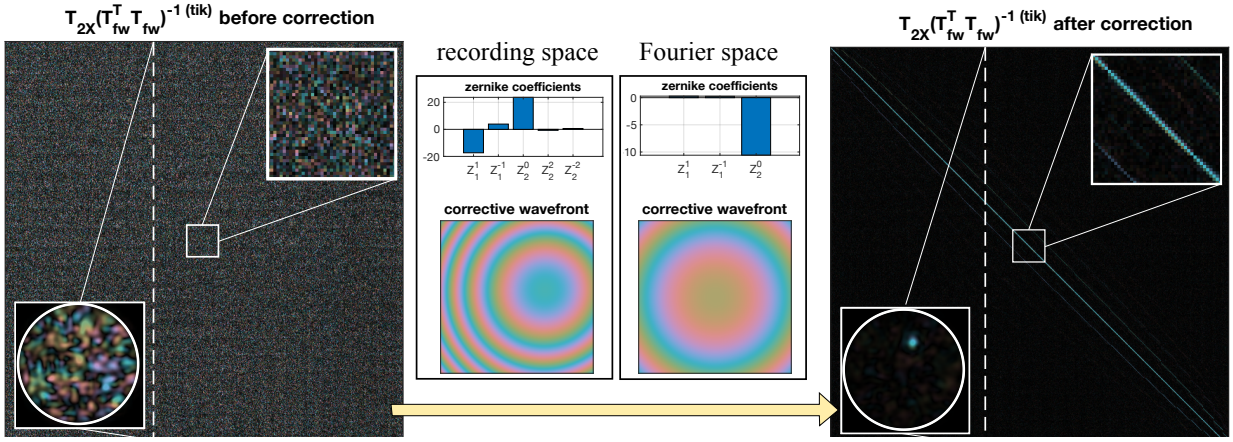

Figure 2.4.4: Visualization of optical reciprocity within the MMF after correcting $\mathbf{T}_{fw}$ for misalignment. During optimization, the amplitude of each Zernike polynomial is iteratively updated to minimize the difference between experimental and synthesized round-trip transmission. The Newtonian-based optimizer was again used to find the optimal correction. The on-diagonal energy ratio improved from 0.27% to 36.6% after the phase mismatch and positional shift corrections, each within tens of iterations.

2.5 Conclusion

In this chapter, we investigated the waveguide physics of MMF based on theory and numerical simulation, and calibrated real-world fiber by measuring its TM. We conveniently analyzed the transmission through MMF by matrix operations, and verified the optical reciprocity hidden in the chaotic transmission. These insights will assist the development of new techniques in the following chapters.

The purpose of computing is insight, not numbers.

— Richard Hamming

3

Confocal 3D Imaging through MMF without WFS

Contents

This chapter focuses on a computational imaging strategy through optical multimode fibers (MMFs), which has the potential to enable hair-thin endoscopes that reduce the invasiveness of imaging deep inside tissues and organs. Current approaches predominantly require active wavefront shaping and fluorescent labeling, which limits their use to preclinical applications and frustrates imaging speed. On the other hand, imaging through MMF without active wave-control has been demonstrated [20, 34, 66], but the methods lead to limited image contrast or assume simple sample structure, and optical sectioning mechanism is lacking. Here we present a computational approach to reconstruct depth-gated confocal images using a raster-scanned, focused input illumination. We demonstrate the compatibility of this approach with quantitative phase, dark-field, and polarimetric imaging. Computational imaging through MMF opens a new pathway for minimally invasive imaging in medical diagnosis and biological investigations. These results have been published in Optica.

3.1 Overview

In this chapter, we express forward light transmission through a MMF as matrix $\mathbf{T}$, as illustrated in Fig. 3.1.1(a). The measurement of $\mathbf{T}$, by determining the amplitude and phase of the output speckle pattern arising from focal illumination at each independent transverse location on the input fiber facet, calibrates the transmission from the proximal end (P) to a distal calibration plane (at $z = 0$). The MMF output speckle pattern on the calibration plane per each proximal input realization constitutes a column vector of $\mathbf{T}$. In imaging mode with a sample at the fiber distal end, we illuminate and detect light from the fiber proximal end. This corresponds to a bi-directional light transport consisting of forward transmission through the MMF, free-space propagation to an observation plane

(OP) modeled by Fresnel diffraction ($\mathbf{H}$), speckle illumination on and backscattering from the sample, coupling back into the same MMF, and backward transmission to the proximal facet. The TM representing backward transmission $\mathbf{T}^{\mathrm{T}}$ is the transpose transformation of the forward TM $\mathbf{T}$ due to underlying reciprocity [41], and the overall round-trip reflection matrix $\mathbf{M}$, describing optical transmission from and to the proximal side can be expressed as

$$\mathbf{M} = \mathbf{T}^{\mathrm{T}} \left(\sum_i \mathbf{H}\left(z_i\right)^{\mathrm{T}} \mathbf{R}\left(z_i\right) \mathbf{H}\left(z_i\right) \right) \mathbf{T}, \tag{3.1}$$

similar to [40, 67]. $\mathbf{R}\left(z_i\right)$ quantifies the backscattering process of the light-sample interaction in the spot basis on the distal OP at distance z_i from the calibration plane, with i indexing all sample layers. Multiplication with $\mathbf{H}\left(z_i\right)$ corresponds to convolution with the impulse-response function of free-space propagation by z_i. $\mathbf{R}$ has intrinsic transpose symmetry, $\mathbf{R} = \mathbf{R}^{\mathrm{T}}$. Each column of $\mathbf{M}$ is a proximally recorded speckle pattern per input realization and contains contributions from all present sample layers. The transpose symmetry of $\mathbf{M}$ that follows from Eq. 3.1 is experimentally attained as elaborated in the Experimental Setup section.

The computational reconstruction is conceptually illustrated in Fig. 3.1.1(b). With a previously measured $\mathbf{T}$, we can digitally compensate the light scrambling during round trip MMF propagation and isolate the scattering signal of the various sample layers, including propagation from and to the fiber facet. This is similar to modeling conventional confocal microscopy, with the fiber facet taking the place of the principal output plane of the objective lens. The $\mathbf{H}$ matrix is independent of fiber shape and can be numerically generated for any desired OP position z_i. Right- and left- multiplying $\mathbf{M}$ with the inverse and transpose inverse of $\mathbf{H}\left(z_i\right)\mathbf{T}$, respectively, extracts the in-focus signal from layer at z_i. The signal from adjacent layers $z_j \neq z_i$ is suppressed with increasing layer separation owing to the confocal gating effect, which arises from the defocusing $\mathbf{H}\left(z_j\right)\mathbf{H}^{-1}\left(z_i\right)$ acting independently both on the illumination and detection side. For simplicity, we drop the subscript of z_i and use z to specify the OP position from here on.

In practice, we used Tikhonov regularization to approximate the inversion and transpose inversion of the fiber transmission, $\mathbf{T}^{-1(\mathrm{tik})}$ and $\mathbf{T}^{-\mathrm{T}(\mathrm{tik})}$, with the regularization parameter set to 10% of the largest singular value as justified by the L-curve method [68]. The approximated sample signal $\mathbf{R}(z)$, $\tilde{\mathbf{R}}(z)$ thus can be derived as

$$\tilde{\mathbf{R}}(z) = \mathbf{H}^{-\mathrm{T}}(z)\,\mathbf{T}^{-\mathrm{T}(\mathrm{tik})}\mathbf{M}\mathbf{T}^{-1(\mathrm{tik})}\mathbf{H}^{-1}(z) \approx \mathbf{R}(z), \tag{3.2}$$

where matrices are defined regardless of basis representation. When the input and output of $\tilde{\mathbf{R}}$ are both in the spot basis, an adequate high-contrast image reconstruction of the *en face* scattering on the OP can be obtained by reshaping the intensity on the diagonal of $\tilde{\mathbf{R}}$ into its corresponding 2D xy-layout. The graphical expression of the computational reconstruction by using Eq. 3.2 is shown in Fig. 3.1.2. Physically, the diagonal elements of $\tilde{\mathbf{R}}$ correspond to synthetic focused illumination and detection occurring through identical channels on the OP, creating a spatial confocal gating effect with a depth of focus determined by the effective numerical aperture (NA) available at each location on the OP. By varying the propagation distance of $\mathbf{H}(z)$, we can numerically shift the OP along the optical axis to different distances and reconstruct the full addressable 3D image volume from a single measured $\mathbf{M}$.

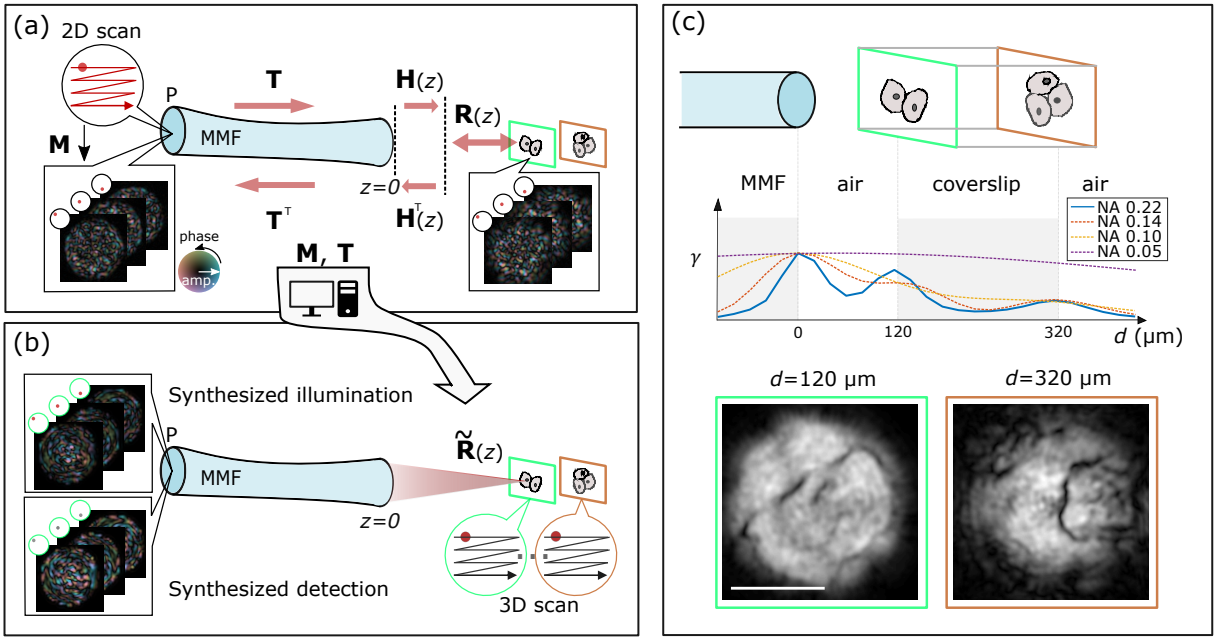

Figure 3.1.1: Overview of computational confocal imaging through MMF. (a) We calibrate the MMF by measuring $\mathbf{T}$. In the imaging phase, we measure the coherent round-trip $\mathbf{M}$ through the same set of proximal channels as used for calibrating $\mathbf{T}$, but now in the presence of a distal object. The $\mathbf{H}$ matrix accounts for free-space propagation from the calibration plane to an OP. The sample is illuminated by different speckle realizations due to the proximal 2D scan, and $\mathbf{R}$ denotes light-sample interaction. The measured $\mathbf{M}$ and $\mathbf{T}$ are used for computational reconstruction. (b) By modeling the round-trip light transmission with matrix multiplications, we can compensate the MMF scrambling using the measured $\mathbf{T}$ and modeled $\mathbf{H}$ to isolate the reflection matrix $\tilde{\mathbf{R}}$ at a certain depth. The image of the sample is reconstructed from the diagonal of $|\tilde{\mathbf{R}}|^2$, corresponding to confocal illumination (red) and detection (gray) through all available channels. Note that the illumination and detection spots are overlapping on the sample. With numerical refocusing, we can generate a complete 3D scan from a single measured $\mathbf{M}$. The color map encodes complex values. amp.: amplitude. (c) γ curves show the intensity reflection signal summed in the lateral directions as a function of physical distance d from the fiber facet for the schematically depicted sample. Only the full fiber NA = 0.22 can correctly resolve the three reflective interfaces. The *en face* images show confocal images of buccal epithelial cells deposited on the front and back surface of the coverslip, reconstructed with the full fiber NA. The scale bar is 50 µm.

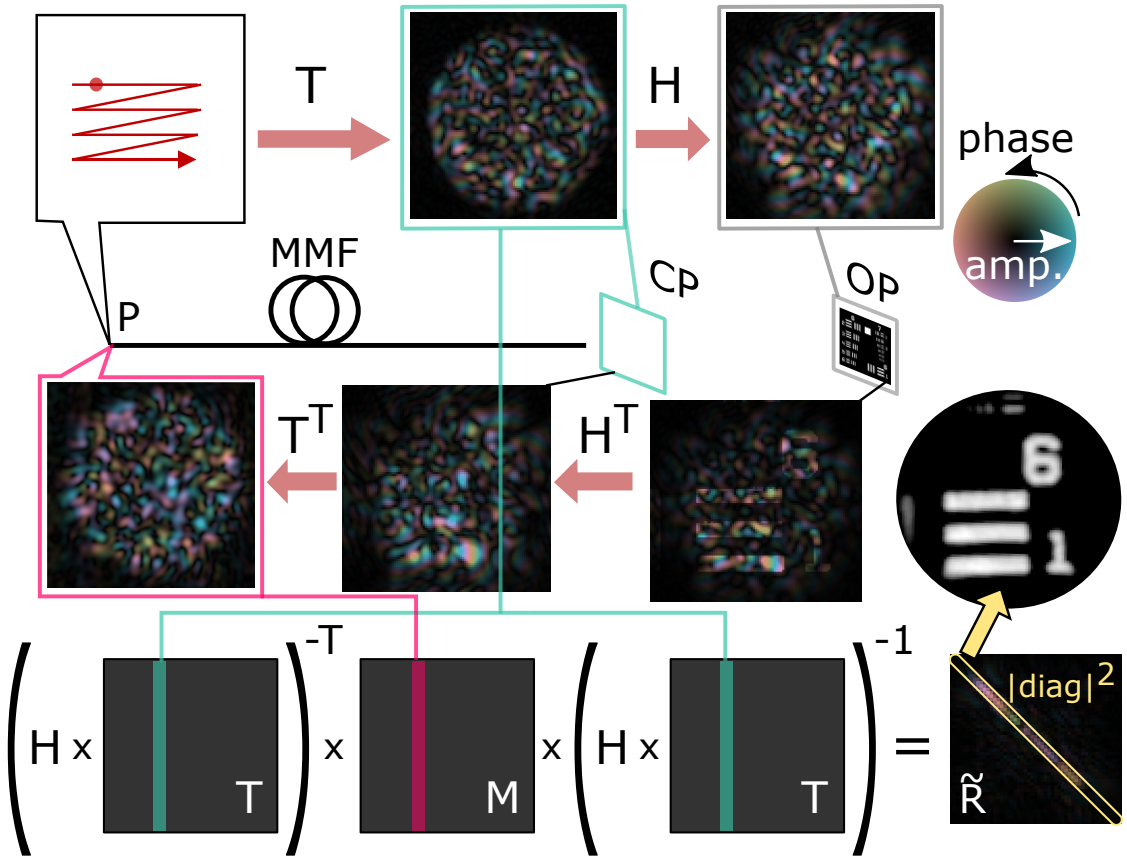

Figure 3.1.2: The graphical expression of computational reconstruction. The complex patterns visualize the light field evolution of one MMF input realization at each location throughout the MMF imaging arrangement. CP: calibration plane, which defines the output plane of **T**. The speckle pattern on CP corresponds to one column of the **T** matrix, and the speckle pattern on the proximal side of returning light corresponds to one column of the **M** matrix. The $\tilde{\mathbf{R}}$ matrix, which is extracted from measurement **M** with calibration **T** and free-space propagation model **H**, allows a confocal image reconstruction of the distal object at OP by reshaping the main diagonal to 2D coordinates.

3.2 Experimental Setup

3.2.1 MMF Calibration

All experiments in this chapter used a 1-m-long step-index MMF with 105 µm core diameter and a NA of 0.22 (FG105LCA, Thorlabs) that theoretically supports ~ 550 guided modes per polarization. The fiber was coiled with a minimum radius of curvature of ~ 50 mm. The monochromatic calibration matrix $\mathbf{T}$ was measured similar to the previous chapter, however, with some modifications. As depicted in Fig. 3.2.1(a), each input and output channel now included two orthogonal polarization states: horizontal (H) and vertical (V). To alternate the illumination polarization between H and V, a laser beam ($\lambda = 1550$ nm and linewidth < 100 kHz) was linearly polarized and passed through a fiber-based electro-optical phase retarder (PR, Boston Applied Technologies). Instead of using the SLM, the laser was steered by a two-axis galvanometer scanning stage (GM, GVSM002-US, Thorlabs), and then focused by an objective lens (Plan Apo NIR Infinity Corrected, Mitutoyo) with a NA of 0.4 into a 2.5 µm full-width at half maximum (FWHM) spot on the proximal facet of the MMF. The focal spot position on the proximal input side was indexed by u and the speckle pattern exiting on the distal side was imaged with another identical objective lens and a tube lens ($f = 30cm$) onto an InGaAs camera (OW1.7-VS-CL-LP-640, Raptor Photonics) with exposure time of 20 µs at 120 frames per second. The distal channel in real-space was indexed by ν. The object plane of the distal imaging system determined the calibration plane, which was approximately 100 µm away from the distal facet. We define d as the distance of the OP away from the MMF distal facet (at $d = 0$). A beam displacer (BD40, Thorlabs) was used in front of the camera to spatially separate the output into H and V polarization states. An angled plane reference wave polarized at 45° independently interfered with the two speckle patterns on the camera to record the speckle field amplitude and phase through off-axis holography in both detection polarization states simultaneously. Images of the two polarization states were demodulated, spatially

registered, and flattened into a column vector of $\mathbf{T}$ directly in the Fourier domain, with output channels at (k_x, k_y) indexed by ν_F. Transmission was recorded for an oversampled grid of input spot positions u within the core region, typically ∼700 points for each input polarization state, sequentially generated by driving the GM and PR. The total acquisition time was 20 seconds. The input and output spatial channels of $\mathbf{T}$ have been ordered first by spatial coordinate, then by polarization.

3.2.2 Measuring Sample Reflection

In imaging experiments, as illustrated in Fig. 3.2.1(b), a sample was placed in front of the MMF distal tip (b-1) and the round-trip $\mathbf{M}$ was measured from the proximal side (b-2). We again sequentially coupled light into the MMF through the same set of proximal input states. Light with a power of ∼0.5 mW exited the distal facet and propagated towards the sample, where part of the light backscattered and coupled back into the same MMF. On the proximal side, we recorded the round-trip light transmission by decoupling its path from the illumination with a non-polarizing beam splitter and directing it to the same off-axis holography setup. The exposure time was set in the range $200 - 1000$ µs depending on the sample. A complete round-trip sample measurement was acquired in 20 s. To preserve the symmetry between the illumination and the detection configurations and to obtain a square matrix $\mathbf{M}$, we sampled the recorded complex output fields at the ordered positions identical to the set of input states. The matrix $\mathbf{M}$ was then constructed with the same procedure that was used to find $\mathbf{T}$. Similar to the round-trip TM correction in Chapter 2, we compensated the physical misalignment in $\mathbf{M}$ to accurately match the input channels and recovered the underlying transpose symmetry. Using the sample measurement $\mathbf{M}$, the pre-measured $\mathbf{T}$, and $\mathbf{H}(z)$, we then computed $\tilde{\mathbf{R}}$ following Eq. 3.2.

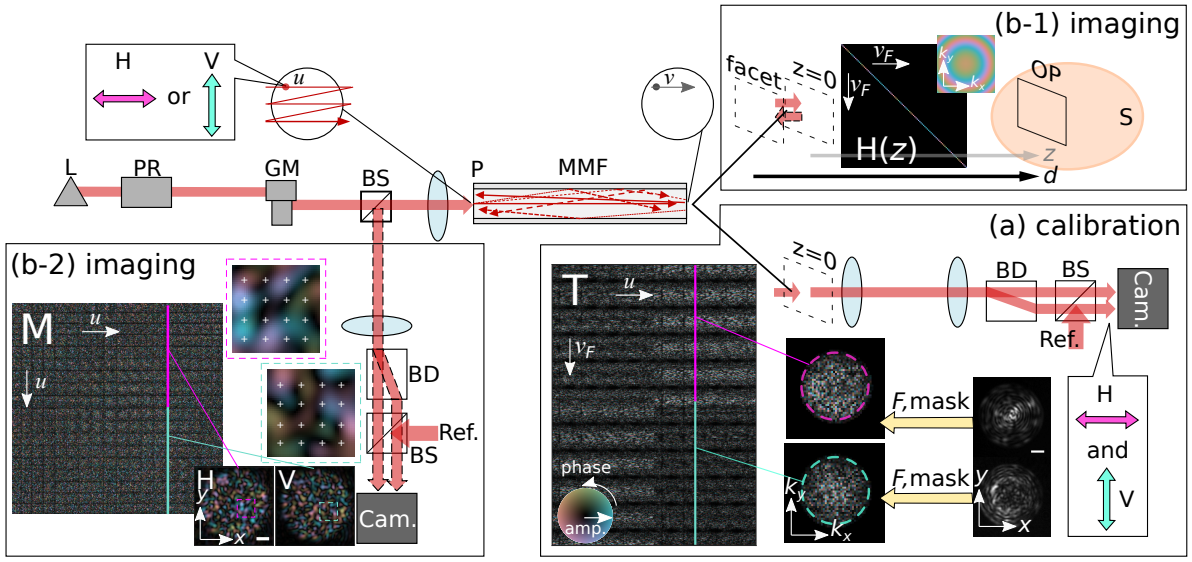

Figure 3.2.1: Measurements of the MMF TMs. The fiber, although drawn as if it were straight, was in fact coiled in experiments. The red arrows correspond to light pathways, and the dashed ones indicate reflected light traveling from the sample through the MMF in the reverse direction to the proximal detection. BD: beam displacer, BS: non-polarization beam splitter, Ref.:reference wave, Cam.: camera, S: sample. A focused spot was scanned with the GM across positions indexed by u distributed over the MMF proximal input facet and alternating between H and V polarizations by means of the PR. The output field was split into two orthogonal polarization states by the BD, and interfered with matching reference waves for simultaneous recording. (a) In the calibration phase, the camera records the transmitted speckle pattern interfering with the reference wave in spatial coordinates (x, y) (rightmost insets). In the Fourier domain, we isolated the demodulated complex-valued signals in momentum coordinates (k_x, k_y) confined to a frequency band imposed by the fiber NA and rearranged them into a column vector of $\mathbf{T}$, as indicated by the solid vertical line, color-coded in magenta and cyan for the H and V polarizations, respectively. The forward transmission $\mathbf{T}$ has rows and columns indexed by ν_F and u, respectively, and was ordered first by the spatial modes, and then by polarization states. Only a subset of $\mathbf{T}$ is shown here. The color map encodes complex values. (b-1) In the imaging phase, light backscattered from distal OPs at varying d from the fiber facet. Free-space propagation, modeled by $\mathbf{H}$, is a diagonal matrix in ν_F where it defines a quadratic phase in the Fourier domain. (b-2) The detected images were demodulated into complex-valued images of the proximal output speckle in spatial coordinates (x, y), then down-sampled at the positions of the input foci (shown as white markers in the dashed magenta and cyan boxes) following the same ordering as for illumination, and flattened into column vectors of the square matrix $\mathbf{M}$. $\mathbf{M}$ thus has rows and columns indexed both by u. Only a subset of $\mathbf{M}$ is shown here. The scale bars in the insets are 20 µm.

3.2.3 Numerical Refocusing

For a sample with volumetric structures, under weakly scattering regime and the Born approximation, we can express the total light reflection counting from the calibration plane ($z = 0$) as a summation of backscattering fields contributed from individual OPs at varying axial positions. In Eq. 3.1, $\mathbf{H}$ is a unitary TM modeling the loss-less free-space propagation from the calibration plane to the OP, as shown in Fig. 3.2.1(b-1). Due to the unitary matrix properties,

$$\mathbf{H}^{-1} = \mathbf{H}^{\dagger} \quad \text{and} \quad \mathbf{H}^{-\mathrm{T}} = \mathbf{H}^{\star}, \tag{3.3}$$

where the superscript –1, –T, †, and $\star$ indicate true inverse, true inverse of transpose, Hermitian transpose, and conjugate, respectively. Note that $\mathbf{H}$ simply reduces to an identity matrix when $z = 0$. According to Fresnel diffraction theory under paraxial approximation, the transfer function of a free-space propagation is a convolution kernel in real space, or a multiplicative quadratic phase term in the Fourier domain. Depending on the distance, z, of a selected OP, we can compute the Fourier phase term accounting for the propagation process

$$F(k_x, k_y, z) = \exp\left(\frac{-iz(k_x^2 + k_y^2)}{k_n} \right), \tag{3.4}$$

where k_n is the wavenumber in the given medium and k_x and k_y are the coordinates in the in-plane momentum domain. The matrix $\mathbf{H}(z)$ in Fourier domain is then a diagonal matrix and incorporating it into $\mathbf{T}$ through left-multiplication extends the output of $\mathbf{T}$ to the OP at z. Note that $z/k_n = zn/k_0$, where k_0 is the wavenumber in $n = 1$, encodes the optical path length, which is the physical thickness of the medium multiplied with its refractive index n, and $\mathbf{H}$ is parameterized only by z and independent of fiber shape and $\mathbf{T}$. Plugging Eq. 3.1 into Eq. 3.2 and setting $z = z_j$, Eq. 3.2 becomes

$$\tilde{\mathbf{R}}(z_j) \approx \mathbf{R}(z_j) + \sum_{i \neq j}^{N} \mathbf{H}^{-\mathrm{T}}(z_j)\mathbf{H}^{\mathrm{T}}(z_i)\mathbf{R}(z_i)\mathbf{H}(z_i)\mathbf{H}^{-1}(z_j), \tag{3.5}$$

where we isolate the in-focus from the out-of-focus matrices. By varying z, we can digitally shift to the j$^{\text{th}}$ OP at $z = z_j$ without repeated measurements

3.3 Confocal Gating

3.3.1 Confocal Image Reconstruction

In Eq. 3.5, assuming the out-of-focus reflective planes are separated from the in-focus plane by much more than a depth of focus, and the total background energy is uniformly distributed over all spatial channels, we can approximate the summation of out-of-focus terms as a complex matrix with random phases but a constant amplitude. In real-space coordinates, collecting the on-diagonal elements of $\tilde{\mathbf{R}}(z_j)$ hence leads to signal predominance by the *en face* reflectivity at $z = z_j$ and suppression of out-of-focus signals, or background rejection. Based on this, in experiment, after obtaining $\mathbf{R}$, its input and output bases were converted from the Fourier domain to real-space indexed distal channel ν by multiplication with a pre-computed inverse discrete Fourier transform matrix. A 2D confocal intensity image $\mathbf{I}$ of sample reflectance at the OP was then reconstructed by reshaping the diagonal of $\tilde{\mathbf{R}}$ as

$$\mathbf{I}(x, y) = |\tilde{\mathbf{R}}[\nu(x, y), \nu(x, y)]|^2, \tag{3.6}$$

where the point (x, y) is mapped from the distal channel ν to real-space coordinates, and $[\cdot]$ indicates matrix entries, arranged in rows and columns. For polarization-preserving samples, reconstructed images of co-polarized illumination and detection channels are identical and were incoherently summed to increase signal. This computation was repeated for multiple values of z to generate 3D images from a single reflectance measurement $\mathbf{M}$ with depth expressed in d (referenced to distal facet). Intensity images were converted to base-10 logarithmic scale for display. To investigate the effect of reduced fiber NA as in Fig. 3.1.1(c), we optionally truncated the spatial frequencies of the measured $\mathbf{T}$. Owing to the Tikhonov-regularized inversion this has the same effect as limiting the spatial frequencies in the sample measurement $\mathbf{M}$ and emulates the use of MMF with a lower NA.

3.3.2 Wide-field Image Reconstruction

From the same measured $\mathbf{M}$, we can also obtain wide-field imaging that is equivalent to the turbid lens imaging algorithm [69]. We compensated for the reverse MMF transmission of reflectance from the sample under the variety of speckle illuminations, and then incoherently averaged the reflectance to statistically compose a uniform illumination. In terms of matrix operations, we left-multiply Eq. 3.1 with $\mathbf{H}^{-\mathrm{T}}\mathbf{T}^{-\mathrm{T(tik)}}$

$$\tilde{\mathbf{R}}\mathbf{H}\mathbf{T} = \mathbf{H}^{-\mathrm{T}}\mathbf{T}^{-\mathrm{T(tik)}}\mathbf{M}, \tag{3.7}$$

where each column of the matrix product is the sample reflection resulting from a distinct speckle illumination. Wide-field images were reconstructed by integrating the absolute square of $\tilde{\mathbf{R}}\mathbf{H}\mathbf{T}$ along the input dimension into a single column vector

$$\sum_u |\tilde{\mathbf{R}}\mathbf{H}\mathbf{T}(:,u)|^2, \tag{3.8}$$

and reshaping the vector back to 2D coordinates. $\mathbf{T}(:,u)$ means u^{th} column vector of $\mathbf{T}$. To simplify computation, the matrix product $\mathbf{H}\mathbf{T}$ in Eq. 3.7 was assumed to be unitary, so that by Parseval's theorem the integrated row intensity of $\tilde{\mathbf{R}}\mathbf{H}\mathbf{T}$ is identical to that of $\tilde{\mathbf{R}}$. Confocal and wide-field images from the same $\tilde{\mathbf{R}}$ can be thereafter fairly compared.

3.3.3 High Contrast Confocal Imaging

Following the concepts in Sections 3.2.3 and 3.3.1, to demonstrate the depth gating effect of our computational reconstruction, we imaged a 3D sample through the MMF, as shown in Fig. 3.1.1(c). The sample is a coverslip in air with buccal epithelial cells deposited on both surfaces. We computed the confocal image for each OP at varying distance d from the MMF distal facet ($d = 0$) and calculated the corresponding integrated reflectivity (γ) by summing the intensity over the entire *en face* image. The γ versus depth profile reveals three separated peaks (blue curve), which inform on the position of the reflective MMF facet and coverslip surfaces, with their axial positions at $d = 0$, 120, and 320 µm considering the

medium's refractive index. To evidence the confocal gating mechanism at play, we computed the γ profiles corresponding to a reduced fiber NA (0.14, 0.1, and 0.05) by truncating the spatial frequency of $\mathbf{T}$. The axial signal peaks blur with reduced fiber NA and fail to resolve the individual sample interfaces, confirming the expected strong dependence of axial rejection power on the NA. The green and brown insets show high-contrast images of cells on the front ($d = 120$ µm) and back ($d = 320$ µm) surfaces of the coverslip, respectively, using the full fiber NA. Our matrix approach, which achieves confocal gating with numerical refocusing, thus enables 3D imaging from a single measured $\mathbf{M}$ without WFS. For more details and additional results of this experiment, please see Section 3.5.4.

To further evaluate the confocal gating effect, we imaged a USAF resolution chart (R1D21P, Thorlabs) in air or intralipid and distances d through the MMF, as sketched in Fig. 3.3.1(a). In each medium, a sample reflectance matrix $\tilde{\mathbf{R}}$ was computed from a single measured $\mathbf{M}$ for each OP at varying depth, and processed to reconstruct confocal and wide-field images for direct comparison, as shown in Fig. 3.3.1(b). In each imaging condition and modality, we calculated the corresponding γ profile, which is normalized by the highest value along the axial OP positions. The γ profile allows us to find the in-focus position. Since the chart has a binary reflectance pattern across its surface, we can quantify the intensity image contrast as

$$\varsigma = \frac{I_p - I_g}{I_p + I_g}, \tag{3.9}$$

where I_p and I_g are the intensities of the chrome pattern and the glass substrate, respectively. In experiments, I_p and I_g are averaged within selected regions of interest on in-focus images for the chrome and glass substrate areas, respectively.

We first demonstrated optical sectioning by imaging the chart placed at $d = 120$ µm in air. In Fig. 3.3.1(c), the confocal method renders the chart patterns with a high contrast of 0.9 due to the rejection of background signals from reflection at the MMF facet. The value is close to the expectation $\sim$0.92, assuming full reflection from the chrome

pattern and 4% reflection at the air-glass interface. In Fig. 3.3.1(e), the profile reveals two prominent and separated peaks at $d = 0$ and $d = 120$ µm, corresponding to the MMF facet and the resolution chart, respectively.

To test the capacity of computational confocal gating in the presence of additional sample scattering, we imaged the chart placed at $d = 400$ µm in agarose gel mixed with 2 wt.% intralipid, which corresponds to ∼0.36 mean free paths. In Fig. 3.3.1(d), the reduced confocal image quality may be due to: intralipid scattering that distorted the wavefront and the reconstructed images, and degraded spatial resolution upon beam divergence at large d (elaborated in the following section). Despite the scattering medium and lower signal to background ratio when the chart is far from the facet, the confocal image maintained a high contrast of 0.96, compared to a theoretical value of ∼0.99 (assuming 0.4% reflection at the gel-glass interface). In Fig. 3.3.1(f), the peak in the γ profile at $d = 400$ µm corresponds to the chart, and, although weak, precisely informs on its physical location when assuming the medium's refractive index to be 1.4. These results evidence the effective suppression of out-of-focus scattering and reflection signal without active WFS.

To theoretically compare the confocal method to the wide-field processing explained in Section 3.3.2, one can juxtapose Eqs. 3.7 and 3.2 to find that the matrix multiplication also on the right side of $\mathbf{M}$ pre-compensates the light scrambling effect of the MMF forward transmission, and synthesizes sharp foci through the MMF on a selected OP. In contrast, the wide-field processing of $\tilde{\mathbf{R}}$ corresponds to speckle illumination, as illustrated in Fig. 3.3.1(b). When imaging in air as in Fig. 3.3.1(c), while the pattern with wide-field imaging stands out from the background on the OP at $d = 120$ µm, the strong background reflection from the facet results in a low contrast of 0.48, and the corresponding γ profile in Fig. 3.3.1(e) remains constant throughout the entire observation range. When imaging through intralipid, the wide-field image in Fig. 3.3.1(d) can barely distinguish the pattern from the background, resulting in poor contrast of 0.11. The uniform γ plot of wide-field imaging in Fig. 3.3.1(f) again exposes the lack of optical sectioning.

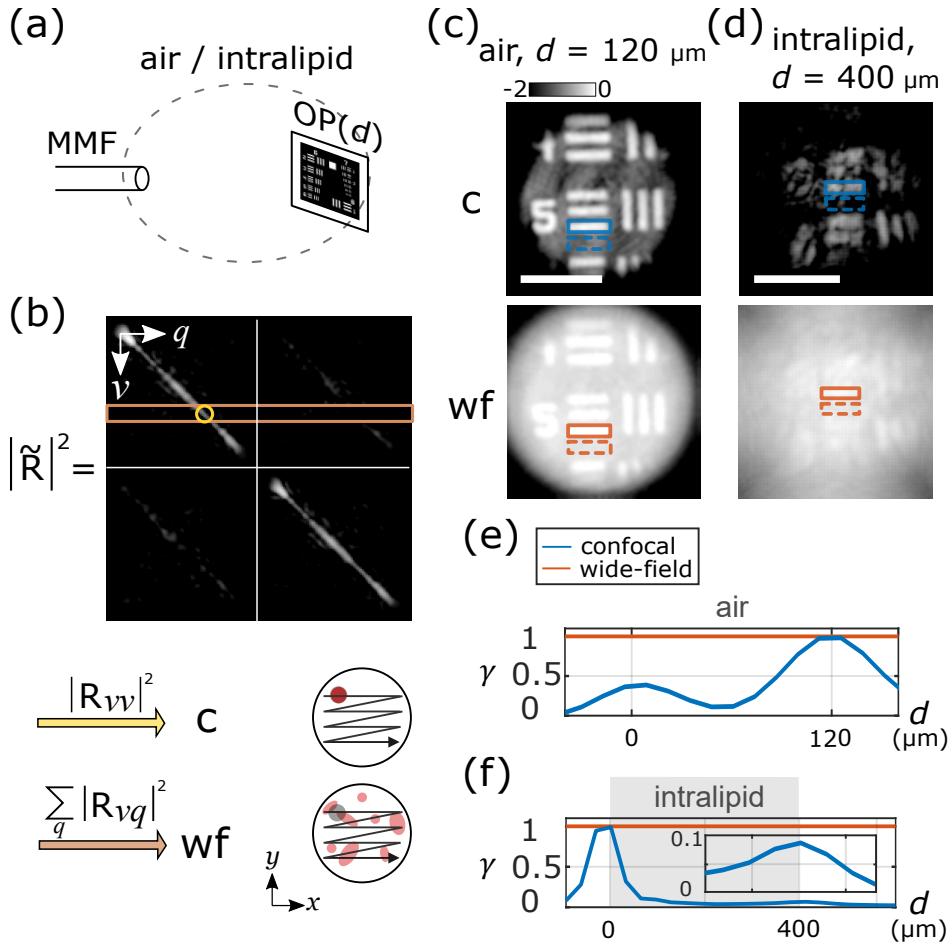

Figure 3.3.1: Depth gating of computational confocal imaging. (a) Imaging geometry: a resolution chart was imaged a distance d in front of the distal MMF facet. (b) From the computed sample reflectivity matrix $\tilde{\mathbf{R}}$, pixels of a confocal image were obtained by taking the intensity of diagonal elements, and of a wide-field image by taking the energy of row vectors for all available distal channels, visualized by the yellow circle and the brown rectangular box, respectively, for a single channel. Images at multiple depths were computed from the same measured $\mathbf{M}$ with numerical refocusing. The image diagrams show the fundamental difference in illumination (red) and detection (gray) patterns of computational image formation. c: confocal; wf: wide-field. (c)-(d) Confocal images showed high, axially localized contrast compared to wide-field images, both in (c) air (at d = 120 μm) and in (d) intralipid media (at d = 400 μm). Images show logarithm of normalized intensity. The solid line (or dashed line) boxes indicate chrome pattern (or glass substrate) areas for image contrast quantification. (e)-(f) The normalized integrated reflectivity plots of confocal (blue) and wide-field (orange) images in (e) air and in (f) intralipid media. The scale bars are 50 μm.

3.4 Flexible Reconstruction

Imaging through a MMF using WFS typically scans a focus along a pre-defined scanning trace and records a single image point from each focus location. In contrast, our method illuminates the sample with a sequence of MMF-induced speckle patterns and utilizes the camera for parallel sampling of all addressable locations in the imaging volume. This allows arbitrary definition of sampling grid and working distance in post processing of a single measurement of **M**. As light diverges upon exiting the MMF distal end governed by the fiber NA, computational reconstruction can adapt to a growing field of view (FOV) with increasing OP distance from the fiber facet. Here, we demonstrate this flexible reconstruction in MMF reflectance imaging and evaluate the resulting FOV and 3D spatial resolution as a function of distance from the tip of the fiber.

3.4.1 Digital Resampling of Image Dimensions

The light transport through a MMF and interaction with a distal sample can be well modeled with measured TMs, which contain full complex propagation information of wave-vectors within the NA of the MMF. While the experimental **T** has output channels stored in Fourier domain, with an one-time measured **M** in the imaging phase, arbitrary resampling of 2D image dimensions and also digital adjustment of image size on any selected OPs can be readily configured based on Fourier relations. This offers flexible trade-off between image processing speed and accuracy in a pragmatic circumstance: a lower resampling rate or smaller physical dimension reduces the computational burden, which is suitable for a faster image preview, whereas a higher resampling rate produces a detailed and smooth image at the expense of longer processing duration. Here, we quantify the trade-off by timing the image processing on a personal computer with a 3.4 GHz Intel Core i7 CPU and 16 GB RAM using MATLAB.

For an arbitrary setting of image physical and digital dimensions, we upsampled the output spatial channels of **T** in the Fourier domain by interpolation, and pre-computed

an inverse discrete Fourier Transform (iDFT) matrix for converting the distal channels to resampled real-space coordinates during the 2D real-space image reconstruction. We focus on the upsampling that corresponds to a valid augmentation to the initial pupil size on the calibration plane (∼105 µm in diameter). Note that the interpolation of $\mathbf{T}$ output channels and the calculation of iDFT matrices are performed prior to actual image formation processes. The necessary computation of images on an OP involves application of phase terms to $\mathbf{T}$ outputs for intended numerical refocusing, distal spatial channels conversion into real-space coordinates with the prepared iDFT matrix, left and right multiplication of $\mathbf{M}$ with regularized inversion of extended backward and forward TMs following Eq. 3.2 to retrieve $\tilde{\mathbf{R}}$, and reshaping back to a 2D image using Eq. 3.6.

In the experiment, the initial $\mathbf{T}$ had output channels accounting for 247×247 square area of camera recording pixels conjugating a physical size of 123×123 µm^2, and the resolution chart as sample was placed on an OP at $d = 10$, 600, 1200 µm away from the facet. For each imaging setting, we timed only the necessary computation. As shown in Fig. 3.4.1, the computation for co-polarization 2D confocal images at $d = 10$ µm with original dimensions and size takes ∼58.2 sec. To reduce computation complexity and complete image formation in a shorter time, we can down-sample the image dimensions to 32×32 in the same physical extent, resulting in pixelated images on OPs at $d = 10$ µm calculated within ∼5.2 sec. For images on an OP at $d = 1200$ µm from the distal MMF facet, illuminating light diverges, and a larger configured image physical dimension is needed to avoid image clipping. For instance, the computation time of 32×32 confocal intensity images covering 247×247 µm^2 on the OP at $d = 1200$ µm is ~ 11.2 sec. Table 3.1 summarizes the computation time of individual settings.

3.4.2 Imaging Performance Characterization

To mimic endoscopic imaging with a variable working distance, a resolution chart was mounted on a translation stage and positioned at different distances $d = 10$, 600, or 1200 µm.

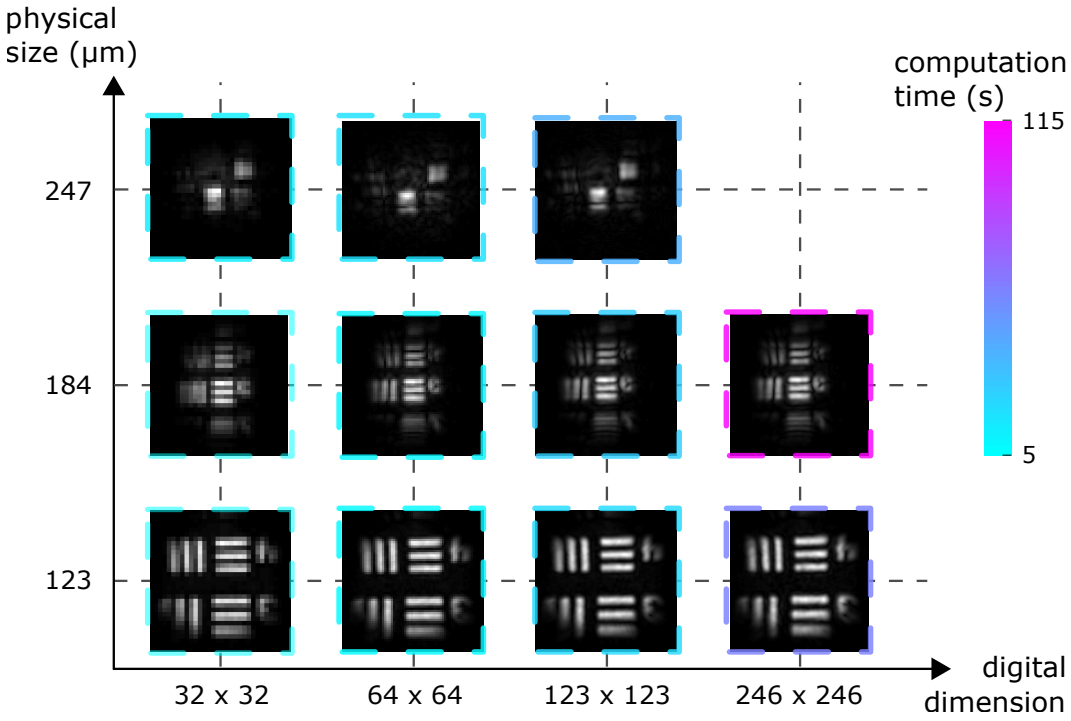

Figure 3.4.1: Computation time and quality of confocal images as a function of physical and digital image size. We only show intensity images in a single polarization state since the sample is binary and isotropic. The time in second is color coded.

computation time (sec)				
physical size (μm)\digital dimension	32	64	123	247
123	5.2	7.9	17.5	58.2
184	7.4	13.7	28.5	114.81
247	11.2	20.3	39.9	

Table 3.1: Computation time of confocal images considering different image configuration settings.

For each d, a round-trip $\mathbf{M}$ was measured and computational reconstruction with numerical refocusing was utilized to locate the axial position of the resolution chart. Figure 3.4.2(a)-(c) show the in-focus confocal images of different chart areas (color boxes in (d)) with physical

dimensions of 123, 184, and 247 µm, when $d = 10, 600$, and 1200 µm, respectively. The illumination power on the chart was kept at ∼0.5 mW. Due to the beam divergence and limited laser power, camera exposure time was increased from 200 µs up to 1 ms for larger d to compensate for the declining photon collection. We filled the space between the fiber and the chart with index-matching gel (G608N3, Thorlabs) to mitigate the specular reflection from the MMF distal facet. In Fig. 3.4.2(a)-(c), imaging from farther away captures a more complete picture, as the FOV expands with increasing d. However, this comes at the expense of spatial resolution and collected reflectance power, as the patterns are severely blurred at $d = 1200$ µm, and background speckle becomes apparent. The finest detail of the chart, element 6 in group 7, can be resolved when the MMF is in close proximity of the facet, $d = 10$ µm, where the FOV is determined on a lower bound by the fiber core size.

To quantify the spatial resolution at varying d, we inferred the lateral resolution, δx, from the smallest resolvable pattern on the chart, as shown by example dashed blue line and its linear intensity profile plot in Fig. 3.4.2(e). Also, since the chart serves as a sharp edge in the axial direction, we utilized the FWHM of the γ profile around the reflectance peak to measure the axial resolution δz. The FOV of each computed image was characterized by its diameter $\varnothing$, set as twice the radius where the radially averaged image intensity dropped below 1% of the center. We tested several imaging realizations and computed corresponding axial profiles and radial mean intensities for statistical analysis, as plotted in red and black curves in 3.4.2(e), respectively, for $d = 10$ µm. For comparison, the theoretically expected spatial resolution was derived considering the effective on-axis NA defined by the minimum between the fiber NA and the solid angle subtended by the fiber core at the corresponding distance from the facet. The overall quantification results are shown in Fig. 3.4.2(f). While the experimental spatial resolution is consistent with diffraction-limited theoretical values, the experimentally determined FOVs are up to 50% smaller than expected at increasing distance. This may be due to the low light collection efficiency of reflectance from distant planar objects. Nevertheless, the agreement in scaling properties of experimental and

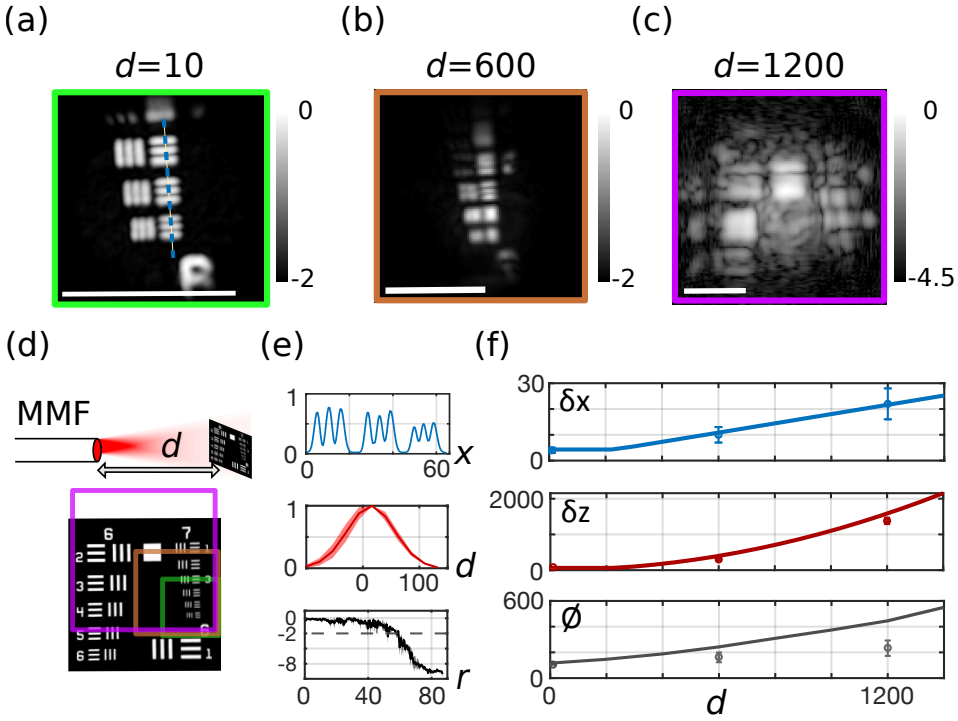

Figure 3.4.2: Characterization of FOV and resolution of computational MMF imaging. (a)-(c) In-focus confocal intensity images of a USAF target at a distance (a) $d = 10$ (b) $d = 600$ (c) $d = 1200$ µm away from fiber facet. The green, brown, and purple boxes correspond to the ones in (d) that highlight the areas of the target. At $d = 1200$ µm, the speckle background reduces the image quality, and the dynamic range of the image was increased to reveal weak signals. (e) Analysis of imaging performance at $d = 10$ µm distance. The blue plot shows the normalized intensity profile in linear scale along the dashed line in the image in (a); the red plot indicates γ at varying d, and its FWHM estimates the axial resolution, with the shadowed areas indicating the standard deviations around the mean value of several independent realizations; the black curve shows the radial mean intensity in logarithmic scale, with 1% cut-off at dashed line roughly equal to the fiber radius. (f) Experimental 3D resolution and FOV at various d and corresponding theoretical values. The scale bars are 100 µm.

theoretical values corroborates the flexibility in addressable spatial dimensions given by the degrees of freedom guided through the MMF. These results demonstrate the convenience of reconstructing the entire sample volume without a pre-defined scan pattern in a practical setting where the sample distance is unknown.

3.4.3 Image Reconstruction from Partial TM Measurement

The flexibility of the matrix approach allows confocal image reconstruction from partial measurements of $\mathbf{M}$ with illumination through only a subset of proximal spatial channels. While the measurement of a full $\mathbf{M}$ by sequentially coupling light into all MMF proximal channels delivers maximal information of the distal sample bounded by the MMF throughput, intermediate confocal images for preview can also be reconstructed from a round-trip measurement with partial set of input realizations, $\ddot{\mathbf{M}}$, which is a subset of $\mathbf{M}$ containing constituent column vectors, leading to a rectangular matrix. As illustrated in Figure 3.4.3(a), with $\ddot{\mathbf{M}}$, we can reconstruct a speckled image on an OP from a computed reflection matrix, $\ddot{\mathbf{R}}$, by respectively left and right multiplying $\ddot{\mathbf{M}}$ with full $\mathbf{T}^{\text{-T(tik)}}$ and $\ddot{\mathbf{T}}^{\text{-1(tik)}}$, which is the regularized inverse of a subset of $\mathbf{T}$ with constituent column vectors at input channels corresponding to $\ddot{\mathbf{M}}$. Physically speaking, the image derived from the partial measurement corresponds to the distal sample under statistically non-uniform illumination. Using confocal intensity images $\mathbf{I}$ for demonstration here, we define the completeness of an intermediate image as the normalized intensity correlation, C, with the final image reconstructed from full $\mathbf{M}$ measurement,

$$C = \frac{\sum_{x,y} \mathbf{I}_i(x,y)\mathbf{I}_f(x,y)}{\sum_{x,y} \mathbf{I}_i(x,y) \sum_{x,y} \mathbf{I}_f(x,y)}, \tag{3.10}$$

where $\mathbf{I}_i$ and $\mathbf{I}_f$ are intermediate and final images, respectively. The completeness arrives at $C = 1$ when $\mathbf{I}_i = \mathbf{I}_f$. Figure 3.4.3(b) shows examples of intermediate images with their quantified completeness. Here, the sample is a resolution chart, and the full $\mathbf{M}$ is a 1354-by-1354 square matrix. We assume that the 1354 proximal input spots uniformly couple to the 1100 MMF guided modes and define the compression ratio as $1 - m/1354$, where m is the number of input realizations. We tested two input channel sampling orders: the original proximal scanning spot basis order (blue curve) and a random sampling order (orange curve). From the plot, we can see that the completeness quickly improves with the number of input realizations and achieves 0.9 with $\sim$200 and $\sim$80 input realizations, which

are only ∼15% and ∼5.9% of the total number of realizations (85.2% and 94.1%compression ratio) in the two ordering conditions, respectively. The random sampling order has a steeper completeness compared to the original since any input channel is less correlated with the next. The intermediate images start from speckled pattern and evolve to clean and high-contrast final confocal intensity image. As a result, while reconstruction from partial measurements compromises background suppression, it accelerates the volume rate, which may be critical for real-time applications.

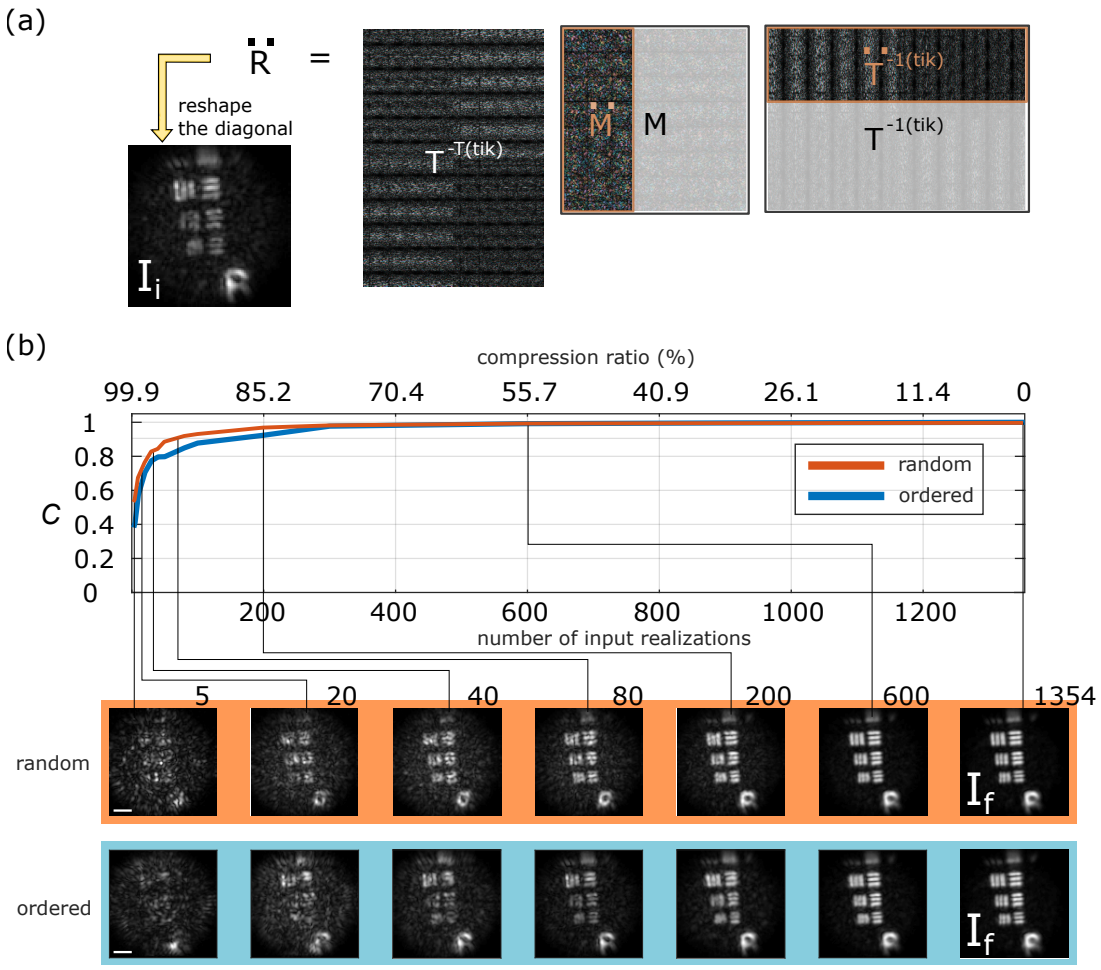

Figure 3.4.3: Confocal intensity image reconstruction with partial measurement (a) Illustration of computational image reconstruction with the MMF forward TM, **T**, and a partially measured round-trip reflection matrix, $\ddot{\mathbf{M}}$ (b) Reconstruction results and image correlation with increasing round-trip measurement completeness in the ordered (blue curve) or a random (orange curve) proximal input channel order. The scale bar is 20 µm.

3.5 Complex Sample Imaging

To improve specificity in confocal MMF imaging without WFS for visualizing unlabeled biological specimens in reflection mode, we leveraged the matrix approach to generate diverse contrasts from a measured round-trip **M** by applying different post-processing, and synthesized multiple imaging modalities to create signal specificity. Different strategies for

image formation are described and illustrated in the following figures.

3.5.1 Quantitative Phase Imaging

In confocal imaging as described in Section 3.3.1, due to the complex nature of $\tilde{\mathbf{R}}$, quantitative phase imaging can be accomplished by taking the complex values of the diagonal elements of a computed $\tilde{\mathbf{R}}$ to form a complex 2D image ($\mathbf{X}$),

$$\mathbf{X}(x, y) = \tilde{\mathbf{R}}[\nu(x, y), \nu(x, y)], \tag{3.11}$$

where the amplitude encodes the absolute reflectivity, and the phase quantifies changes in the wavefront of light propagating through the specimen and back.

3.5.2 Dark-field Imaging

Off-diagonal elements of $\tilde{\mathbf{R}}$ also contain abundant information of sample optical properties, which can be extracted through manipulations on $\tilde{\mathbf{R}}$. For instance, each column of $\tilde{\mathbf{R}}$ represents the scattering at OP in response to an illumination focused on a single channel q. Instead of collecting the intensity at the corresponding location on the matrix diagonal, the intensity of surrounding output channels ν was summed with weights $L(\nu, q)$ given by their Euclidean distance from the input channel on the xy-plane up to an empirical cutoff of $\sim$2.83 Airy disk radius (12 µm on the fiber facet). The on-diagonal confocal signal thus has a zero weight and minimal contribution. This sum was furthermore normalized by the overall intensity

$$\begin{aligned} \mathbf{S}(x, y) &= \frac{\sum_\nu L(\nu(\zeta, \xi), q(x, y)) \times |\tilde{\mathbf{R}}[\nu(\zeta, \xi), q(x, y)]|^2}{\sum_\nu |\tilde{\mathbf{R}}[\nu(\zeta, \xi), q(x, y)]|^2}, \\ L(\nu(\zeta, \xi), q(x, y)) &\equiv \sqrt{(\zeta - x)^2 + (\xi - y)^2} \end{aligned} \tag{3.12}$$

where the Cartesian point (ζ, ξ) maps to the distal channel indexed at ν. $L(\nu, q)$ favors multiply scattered light emerging from channels adjacent to the illumination spot, while the cutoff suppresses signal with excessive scattering paths, arising, e.g., from out-of-focus OPs.

We named this metric scattering contrast (**S**). Since $\tilde{\mathbf{R}}$ is transpose-symmetric, interchanging the illumination and detection renders identically reconstructed images. For each location in the image plane, the scattering contrast **S** is essentially the combination of focused illumination and ring-shaped detection mode, which captures positive signals from the boundaries of sample heterogeneity and is analogous to a dark-field confocal imaging scheme [70].

3.5.3 Computational Multi-Modal Imaging of Unstained Samples

Figure 3.5.1 (a) shows a typical reflection matrix $\tilde{\mathbf{R}}$. The sample arrangement for these experiments, shown in Figure 3.5.1 (b), allowed imaging of a sample on a microscope glass slide in a reflection mode through the MMF, and also in transmission mode (t) with the distal imaging system and bright-field illumination through the MMF as ground truth images. Figure 3.5.1 (c) shows the images of a monolayer of 3 µm polystyrene beads spread on the surface of a microscope slide and imaged in air at $d = 100$ µm. Since the reflectivity of the beads is orders of magnitude lower than that of the air-glass interface, the obtained round-trip $\tilde{\mathbf{R}}$ at in-focus OP has diagonal elements dominated by the specular reflection from the glass slide, resulting in beads silhouetted against the glass signal in the confocal intensity image (**I**) and featuring negative contrast, similar to other reports of reflectance imaging through optical fibers [29, 69, 71]. With the full knowledge of $\tilde{\mathbf{R}}$ and following Eq. 3.12, we are able to extract scattering signal specifically from the beads and create a dark-field-like image (**S**) through numerical engineering of the system point spread function (PSF). Physically, forward scattering by the beads followed by reflection at the glass interface created a multiply scattered signal that partially cross-coupled to neighboring spatial channels. Intriguingly, the cross-coupling signals that delineate the beads provided a slightly higher resolving power than the confocal intensity image, as verified by comparing the line profiles of clustered particles. This exemplifies the benefit of computational reconstruction,

whereas physical implementation of dark-field imaging would traditionally require an annular filter, axicon lens, or customized pinhole, and increase the system complexity [70, 72, 73].

To demonstrate multimodal MMF imaging including phase and dark-field imaging from the same measurement of an unlabeled biological specimen, human buccal epithelial cells were smeared on microscope glass slide and placed at $d = 120$ µm in air. The sample was laterally translated to image several overlapping areas, and at each lateral location a round-trip $\mathbf{M}$ was measured to reconstruct the corresponding image. Multiple images were then stitched together to make a composite image with a wider FOV. Fig. 3.5.1 (d) shows phase contrast (left, $\mathbf{X}$), revealing the contour of cellular membranes and nuclei in its amplitude (coded in brightness), likely because they deflect the focused illumination, which attenuates the reflected signals, thereby resulting in negative contrast. Furthermore, as shown by its color-coded phase, the variation in sample thickness or refractive index inhomogeneity provides an intrinsic phase contrast of the unlabeled sample likely caused by sub-cellular structures, revealing information not contained in the intensity image alone. The scattering contrast image (right, $\mathbf{S}$) delivers complementary information, likely arising from multiple scattering by the sample and coverslip, and positively outlines the cellular membrane morphology along with some cytoplasmic organelles that can be roughly correlated with the transmission image.

3.5.4 Multi-Modal 3D Imaging

To demonstrate 3D imaging of biological samples through the MMF based on numerical refocusing, a sample with multiple layers was prepared following similar volumetric reconstruction experiments performed by others [11, 74, 75]. A proximal reflectance measurement of $\mathbf{M}$ through the MMF included reflectance from multiple layers of a sample, shown in Fig. 3.5.2(top), including buccal epithelial cells deposited on both surfaces of a glass coverslip with thickness of ∼200 µm, placed at $d = 120$ µm in air. From this single $\mathbf{M}$, 3D volumetric imaging was computed by numerical refocusing and image reconstruction.

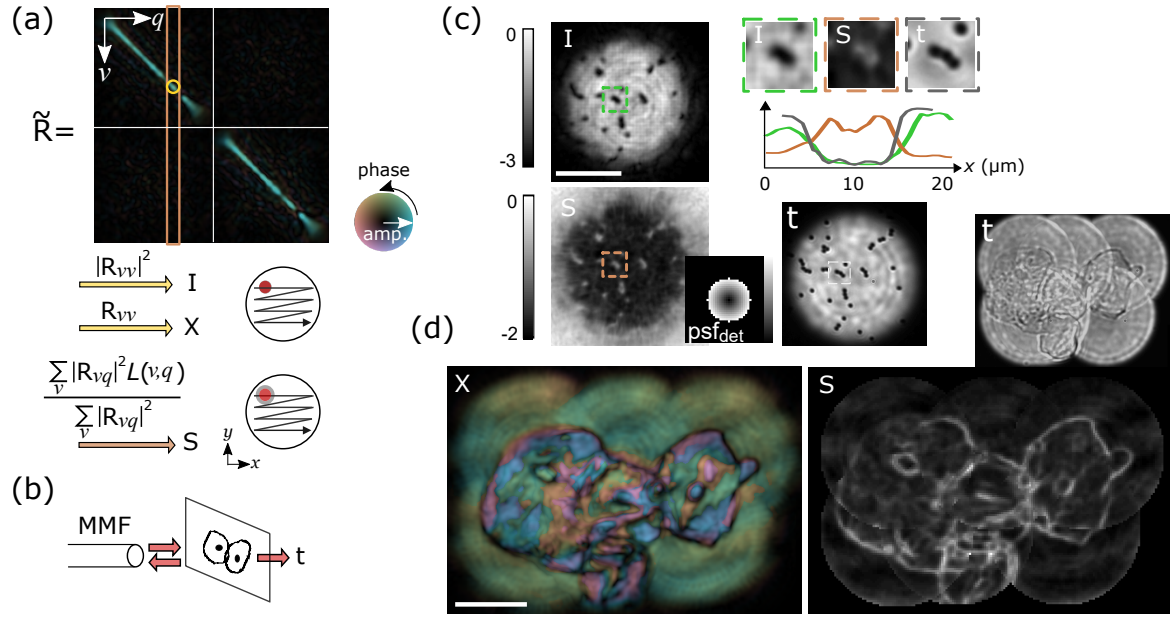

Figure 3.5.1: Multi-modal MMF imaging of unlabeled samples including confocal intensity, quantitative phase, and dark-field scattering imaging. (a) The diagonal elements of $\tilde{\mathbf{R}}$ and correspond to pixels in confocal intensity ($\mathbf{I}$) and complex ($\mathbf{X}$) images, respectively. PSF engineering by an appropriate weighting function applied using Eq. 3.12, generates scattering contrast ($\mathbf{S}$). (b) Sample arrangement at the MMF distal end. Transmission images (t) served as ground truth for verification. (c) Confocal intensity and scattering contrast images of 3 μm polystyrene beads. The ring-shaped detection PSF is shown in the inset. Imaging based on scattering contrast features slightly better resolving power, judging from the plotted line profiles across a cluster of beads. (d) Stitched images of buccal epithelial cells with phase and dark-field contrasts. (left) Phase contrast depicts nuclei and intracellular morphology. (right) Dark-field scattering contrast reveals positive signals at cell boundaries and membrane roughness. The scale bars are 50 μm.

The depth-dependent γ plot was consistent with the physical location of each reflective interface, considering the refractive indices of each layer (1.44 in glass). High-resolution confocal images with intensity, phase, and scattering contrasts were computed at the two individual coverslip surfaces ($d = 120$ and 320 μm). Both planes exhibited contrast from cell samples in all images, consistent with the transmission ground truth, and with high contrast, indicating the confocal gating efficacy. Note that in complex samples, because optical phase accumulates as light is reflected from further into the sample, the phase of shallower cells is overlaid on deeper-lying cells.

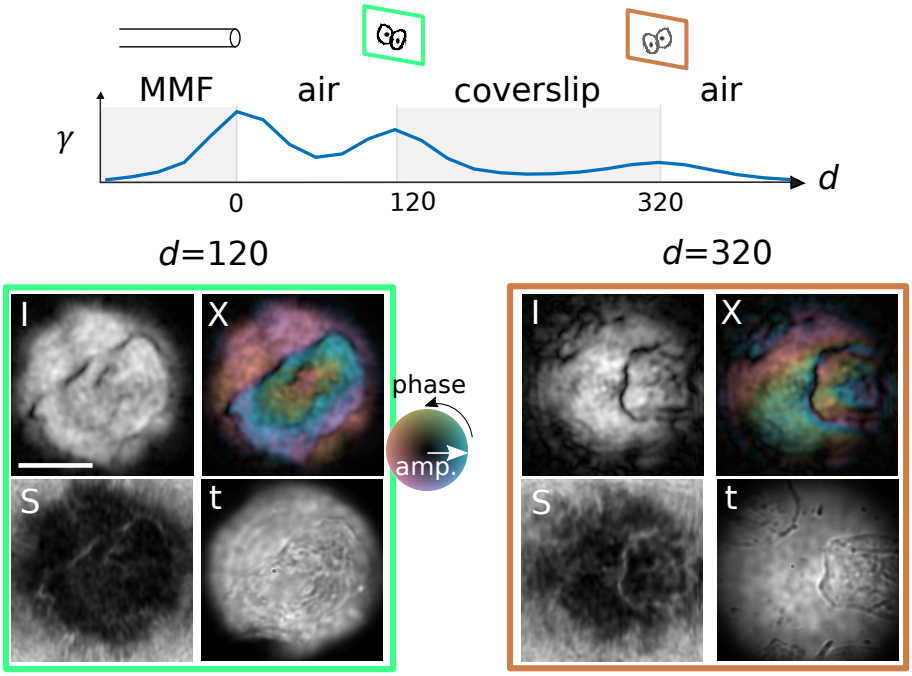

Figure 3.5.2: Label-free 3D computational imaging through the MMF with multiple contrasts. The sample included two layers of buccal epithelial cells deposited on both surfaces of a glass coverslip in air. The d position indicates physical distance and is in the unit of µm. The scale bars are 50 µm.

3.6 Polarimetric Imaging

So far, computation of images from $\tilde{\mathbf{R}}$ only considered co-polarized illumination and detection, where each distal spatial channel ν degenerates into ν_H and ν_V, and entries corresponding to input and output channels were used with the same polarization state. For birefringent samples such as collagen, illumination through a channel in a certain polarization state may induce cross-polarized backscattering.

3.6.1 Polarization Contrast

In $\tilde{\mathbf{R}}$, the diagonals of the two off-diagonal matrix quadrants represent cross-polarized detection, and the sample birefringence at individual image positions (x, y) can be resolved

and characterized by assembling 2-by-2 Jones matrices,

$$\mathbf{J}(x,y) = \begin{bmatrix} \mathbf{J}_{11} & \mathbf{J}_{12} \\ \mathbf{J}_{21} & \mathbf{J}_{22} \end{bmatrix} = \begin{bmatrix} \tilde{\mathbf{R}}[\nu_H, \nu_H] & \tilde{\mathbf{R}}[\nu_H, \nu_V] \\ \tilde{\mathbf{R}}[\nu_V, \nu_H] & \tilde{\mathbf{R}}[\nu_V, \nu_V] \end{bmatrix}, \tag{3.13}$$

in the basis of orthogonal linear polarization states. From the Jones matrix at each channel, a retardation matrix was isolated using polar decomposition. Owing to the intrinsic transpose symmetry, the resulting matrix describes a linear retarder that can be characterized by its amount of retardance (ret) δ and optic axis (OA) ϕ orientation. Endogenous contrast within birefringent samples can thus be retrieved from this polarization-diverse measurement.

3.6.2 Imaging of Birefringent Samples

To demonstrate polarization sensitive (PS) computational imaging through MMF based on our matrix approach and Eqs. 3.13, as illustrated in Fig. 3.6.1(a), we obtained reflection matrices of anisotropic materials including quarter-wave plate (QWP) and cholesterol crystals through the MMF. To validate quantitative retardation and OA measurements, a QWP (WPQ501, Thorlabs) was placed on a microscope slide and its proximal reflection was measured. As show in Fig. 3.6.1(b), the edge of the wave plate was imaged in different orientations to verify the OA orientation retrieved from polarization analysis. One $\mathbf{M}$ was measured in each orientation. Due to the round-trip light propagation, the QWP has an effective half-wave retardance, which leads to full attenuation in the co-polarized detection for confocal intensity images when the slow axis is 45° to the H or V polarizations, and partial attenuation in between. Consistently, the corresponding retardance images reveal a constant π rad retardance of the wave plate regardless of the orientation. On the other hand, the color-coded OA images (combined with brightness-coded ret images) show a rotating OA of the QWP with orientation exactly the same as the slow axis angle. Note that the OA colormap has a periodicity of π instead of 2π used in phase colormaps. Figure 3.6.1(c) shows another example with home-made plate-like cholesterol crystals (S25677, Fisher Science Education) on a microscope slide, which has a much weaker retardance due

to its small thickness (tens of µm) yet uniform optic axis orientation. Judging from the values of retardation, the crystal may be thicker towards the bottom of the image. Since the crystal thickness is much smaller than the confocal gate, interference between the front and back surfaces results in *en face* fringes. A tighter confocal gate may be achieved by switching to MMFs with higher NA or choosing a shorter operating wavelength.

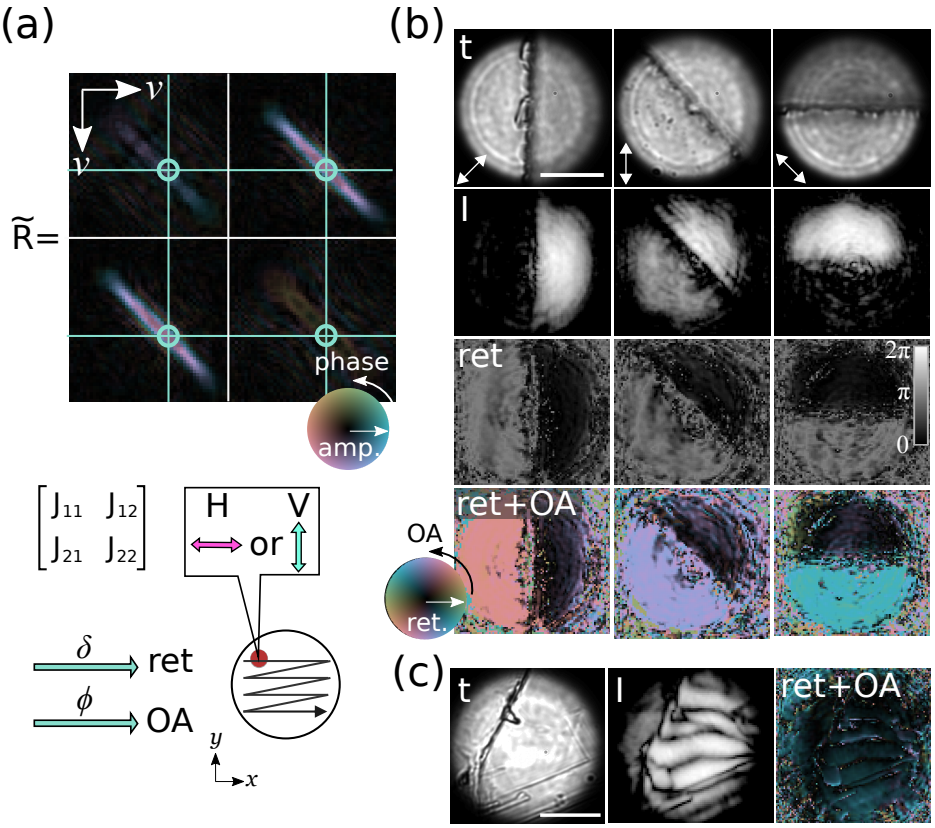

Figure 3.6.1: Birefringence imaging of anisotropic samples through the MMF by utilizing reflection matrices. (a) Illustration of processing the matrix for computational polarization sensitivity. The full reflection matrix $\tilde{\mathbf{R}}$ on an OP provides both co- and cross-polarization entries for assembling a Jones matrix at each spatial channel, which informs on retardation and OA orientation. (b) Accuracy evaluation of anisotropy reconstruction using a QWP with slow axis (white arrows) oriented at 45°, 90°, and 135° with respect to the x axis. While the confocal intensity images only show the sharp edge of the plate, the retardation and OA images unveil its intrinsic optical properties. (c) Birefringence imaging through the MMF of cholesterol crystal precipitated on a microscope slide. The visible fringes are attributed to thin film interference of the crystal and glass surfaces. The scale bars are 50 µm.

3.7 Discussion

Computational confocal imaging through MMF is a novel matrix-based method to obtain depth-gated images using a proximal scanning spot basis for reflectance measurement without WFS, yielding multimodal 3D reflectance of unlabeled samples including confocal intensity,

quantitative phase, dark-field, retardance, and optic axis orientation contrast modalities. Pushing the frontier of MMF imaging techniques, this is the first report of numerical PSF engineering, phase, and polarization-resolved imaging through MMF in a reflection geometry.

High-contrast imaging through MMF frequently relies on fluorescent labeling or is operated in a transmission regime [21, 30, 31, 35, 66], which may be incompatible with practical endoscopic applications. Fluorescence scanning microendoscopy furthermore has potential photobleaching issue [8, 76]. Our computational imaging approach instead efficiently extracts weak elastic scattering signals from unstained samples and operates in a reflection regime, making it favorable for practical endoscopic applications. The matrix approach moreover offers an elegant way of achieving full polarization management and leverages polarization as additional contrast mechanism. In comparison, WFS for physical focusing through MMF typically addresses only a single polarization state [21, 29], to avoid complicated hardware setup required for full polarization-control [30]. While inspired by the arbitrary PSF engineering through complex media in a transmission regime [77], our method here does not need SLM/DMD and optimization. More broadly speaking, illumination and detection with any respective PSF and in any polarization state can be readily engineered by weighting the entries of $\tilde{\mathbf{R}}$ accordingly. Access to the reflection matrix may offer the ability to optimize image contrast for a given sample through post-processing, to synthetically adjust the confocal pinhole size, or to correct for sample-induced aberrations.

The matrix approach employs a simple proximal spot basis for illumination, which relaxes hardware requirements by accepting any 2D scanning module without using WFS. The limiting factor in imaging speed of this work is the InGaAs-camera frame rate of 120 Hz, which may be directly improved by an order of magnitude by replacing it with a faster one or by shifting the operation wavelength towards visible wavelengths with more and even faster camera options. Recently, MMF calibration covering 256 degrees of freedom within only 34 ms has been demonstrated by using a field programmable gate array (FPGA) to address the general latency issue in hardware interfacing and communication

[78]. This work exemplifies the potential of software system optimization and is readily applicable to speed up our implementation. Our approach also allows image formation from a partial round-trip measurement with as few as 200 input realizations, offering an attractive trade-off between image quality and measurement time. Because the reconstruction of individual spatial channels is independent from other channels, this offers high potential for parallelization of the processing using GPU acceleration. With careful engineering of the data acquisition and processing pipeline, fast video-rate imaging should be achievable. Fundamentally, imaging speed of our MMF imaging method is limited by computational complexity, and no longer by hardware as for WFS methods.

MMF imaging has a notorious intolerance to small fiber perturbations such as bending or looping. In Eq. 3.1, while $\mathbf{H}$ and $\mathbf{R}$ are independent of fiber shape, the round-trip matrix $\mathbf{M}$ changes with fiber transmission $\mathbf{T}$. Even small fiber alterations result in distinctive $\mathbf{T}$ and typically require MMF re-calibration. In our experiments, the calibrated 1-m-long MMF was looped and fixed on the optical table and remained stable for several hours without perceivable TM change such that the same measured TM could be used for imaging different samples through the MMF. In a practical setting, a segment of MMF could be mechanically shielded inside a rigid needle or hypodermic tubing to enable high-quality imaging through MMF without re-calibration. Furthermore, several promising strategies are being pursued to address the need for TM calibration without physical access to the distal fiber end: the installation of carefully designed passive optics or a guide star at the MMF distal tip [37, 40, 67], compressive sampling of TM with sparsity constraint [79], or the use of graded-index MMF which has increased robustness of light transport to bending deformations [80].

The disclosed method offers 3D confocal imaging through MMF with high signal specificity, yet is less hardware-demanding than common WFS methods. Even with the present limitation that the MMF must be mechanically stable, our approach may expedite or create applications of minimally invasive MMF-based endoscopy in biomedicine, where probe size and cost are critical factors. For instance, deep brain imaging in neurosurgery,

in situ inspection in needle biopsy, collagen imaging in arthroscopy, and tympanic cavity imaging in middle and inner ear surgery are potential uses of MMF endoscopy. The same methodology may also be extended to optical imaging through other complex or turbid media, or other imaging technologies such as ultrasound tomography.

3.8 Conclusion

In this chapter, we reconstructed high-contrast MMF-relayed images of remote samples from the measurements of elastic optical scattering in a reflection regime based on accurate knowledge of light propagation through MMF. The demonstrated computational imaging through MMF based on round-trip measurements in a proximal spot-basis may prove to be broadly applicable and clinically viable since it avoids the requirement for WFS and the use of fluorescent labeling. The computational contrast rendering further creates signal specificity of label-free samples. Thus, our approach may streamline the system design by circumventing hardware limitations and providing flexibility in image formation.

Memories are the key not to the past, but to the future.

— Corrie ten Boom

4

Efficient dispersion modelling in optical multimode fiber

Contents

Dispersion in complex optical scattering media is an enduring problem to many multispectral imaging or sensing techniques. Here we report a novel parametric dispersion model of the chaotic transmission through optical multimode fiber (MMF) that extends the spatiospectral domain of principal modes. We validate the model in MMF across a broad bandwidth more than two orders of magnitude beyond the uncorrected spectral coherence length. The model enables highly efficient reconstruction of multispectral transmission through MMF over direct measurement. Final manuscript in preparation.

4.1 Efficient dispersion modeling in MMF with exponential mapping

We can express spectral-variant light transmission through MMF as

$$\vec{t}(\omega) = \mathbf{M}(\omega)\vec{s}, \tag{4.1}$$

where $\vec{t}$ and $\vec{s}$ are the vectorized representations of the output and input fields, respectively, and $\mathbf{M}(\omega)$ is the complex TM at an optical frequency ω. The instantaneous dispersion at ω can be computed as a differential matrix

$$\mathbf{m}(\omega) = \frac{\partial \mathbf{M}(\omega)}{\partial \omega}\mathbf{M}^{-1}(\omega). \tag{4.2}$$

Note that while the group-delay operator is more commonly defined as $-j\mathbf{M}^{-1}(\omega)\frac{\partial \mathbf{M}(\omega)}{\partial \omega}$ with eigenvectors as input PMs [81], Eq. 4.2 is equivalent to the convention since the input and output can be converted to each other with Eq. 4.1. In general, the frequency dependent $\mathbf{m}$ is not commutative, i.e., $[\mathbf{m}(\omega), \mathbf{m}(\omega')] = \mathbf{m}(\omega)\mathbf{m}(\omega') - \mathbf{m}(\omega')\mathbf{m}(\omega) \neq 0, \omega \neq \omega'$, and $\mathbf{M}$ cannot be expressed by $\mathbf{m}$ in a closed form. Nevertheless, we can develop

the expression of $\mathbf{M}$ as a fundamental matrix with initial value at ω_o by means of the exponential map of matrix Lie algebra $\mathbf{X}$

$$\begin{aligned}\mathbf{M}(\omega = \omega_o + \Delta\omega) &= e^{\mathbf{X}(\omega,\omega_o)}\mathbf{M}(\omega_o) \\ &\equiv \mathbf{D}(\Delta\omega)\mathbf{M}(\omega_o),\end{aligned} \tag{4.3}$$

where $\mathbf{D}(\Delta\omega)$ is coined as dispersion matrix, modeling the transition of $\mathbf{M}$ due to spectral perturbation $\Delta\omega$. Similar to [82], $\mathbf{X}$ can be subsequently constructed as a series expansion

$$\mathbf{X}(\omega, \omega_o) = \sum_{k=1}^{\infty} \mathbf{X}_k \Delta\omega^k, \tag{4.4}$$

where the complex constant matrix $\mathbf{X}_k$ records the k^{th} order dispersion. When the series is truncated to $k = 1$, Eq. 4.3 reduces to the integral of Eq. 4.4, corresponding to classic PM theory considering only the linear dispersion,

$$\mathbf{M}(\omega) = e^{\mathbf{X}_1 \Delta\omega}\mathbf{M}(\omega_o). \tag{4.5}$$

This assumes that the instantaneous dispersion is frequency-independent, $\mathbf{m} = \mathbf{X}_1$, whose eigenvectors correspond to PMs at the output, and the $\mathbf{M}$ variation due to dispersion can be accounted for by simply scaling with the eigenvalues of $\mathbf{X}_1$, which correspond to the time delays of the PMs. However, random fiber bending or twisting induces higher orders of $\mathbf{X}_k$ and thus spectral variance in $\mathbf{m}(\omega)$, limiting the PMs bandwidth. Crucially, the exponential map in Eq. 4.3 linearizes the dispersion matrix and decouples different orders of dispersion into $\mathbf{X}_k$ series, allowing elegant parameterization of dispersion in a polynomial of $\Delta\omega$.

As illustrated in Fig. 4.1.1(a), to derive the matrix series $\mathbf{X}_k$ and create the dispersion model of MMF following Eq. 4.3, we measured a multispectral TM (msTM) of the MMF at discrete frequencies and solved for $\mathbf{X}_k$ up to K orders that fit the msTM in optimization formalism. Since there is no apparent relative loss or gain between $\mathbf{M}(\omega)$ at different frequencies, $\mathbf{D}$ is configured as a unitary matrix. This leads to manifold optimization associated with Riemannian gradient [83, 84], which also emerges as a fruitful area of

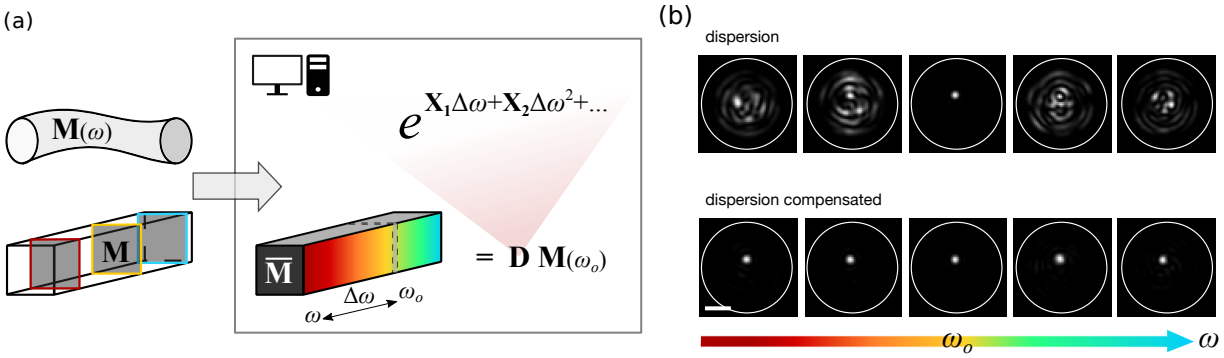

Figure 4.1.1: Overview of the parametric dispersion modeling. (a) We calibrated the MMF transmission at several discrete optical frequencies and created the corresponding dispersion model with matrix series $\mathbf{X}_k$. We then predicted the TM at varying ω, $\overline{\mathbf{M}}(\omega)$, by computing a dispersion matrix $\mathbf{D}(\Delta\omega)$ referenced at ω_o, and reconstructed full spatio-spectral channels of the MMF transmission. (b) To synthesize a focus through the MMF, we digitally propagated the required wavefront from the predicted TM using $\mathbf{M}(\omega_o)$ (top row) or $\overline{\mathbf{M}}(\omega)$ (bottom row) through a separately measured $\mathbf{M}(\omega)$. The circular support outlines the fiber core, and the scale bar is 20µm.

research in the fields of deep or recurrent neural networks as it improves training stability and enhances model robustness [85].

To verify the created dispersion model at a test frequency ω, we compensated the dispersion $\mathbf{D}(\Delta\omega)$ referenced at ω_o, predicted $\overline{\mathbf{M}}(\omega) = \mathbf{D}(\Delta\omega)\mathbf{M}(\omega_o)$ (the overline denotes expected quantity), and compared to the separately measured ground truth. We visualized the results by synthesizing focusing through the MMF at varying frequency, as we can computationally image through MMF without physical focusing in Chapter 3 and [86]. As shown in Fig. 4.1.1(b), the focal spot remains sharp and clean across the entire observation spectrum (bottom), compared to speckle pattern without dispersion compensation (top). This evidences a hidden spectral correlation if the dispersion is properly addressed. Importantly, while fitted at discrete frequencies, the model allows TM prediction over a continuous spectrum not confined to grids of a defined spectral step size.

4.2 Multispectral Transmission Matrix

4.2.1 Experimental Setup

To measure the msTM of a MMF, we set up an automated system as shown in Fig. 4.2.1. A 1-MHz-line-width laser (TSL-510, Santec) and an objective lens (Mitutoyo Plan Apo NIR Infinity Corrected) with a numerical aperture (NA) of 0.4 were used to generate a 2.5 µm FWHM focus spot on the input facet of a randomly looped MMF (FG050LGA, Thorlabs). The focal spot was sequentially coupled into ∼250 individual input spatial channels with a two-dimensional (2D) galvanometer mirror scanner (GVSM002, Thorlabs). For every input spatial channel, the laser was switched between the two horizontal and vertical linear polarization states by a fiber-based electro-optical phase retarder (PRT1010, Boston Applied Technologies Inc.). We used a InGaAs camera (OW1.7-VS-CL-LP-640, Raptor Photonics) with exposure time of 20 µs and a maximal frame rate of 120 Hz, and employed off-axis digital holography to record the complex light emitted from all output spatial channels subject to each MMF input realization, and the two polarization states of the complex output were spatially separated with a beam displacer (BD40, Thorlabs) for simultaneous acquisition. We then recorded the captured output images in the Fourier domain, flattened output images into column vectors, and constructed a monochromatic full TM at the operating optical frequency. The overall acquisition time of one monochromatic TM was about 7 seconds. Repeating the TM measurement from a starting frequency, ω_s, over a spectral span, Ω, at defined optical frequency steps, $\delta\omega$, produced a three-dimensional (3D) msTM, where TM at ascending frequencies were discretized in N sampling points and indexed by n

$$\mathbf{M}_n = \mathbf{M}(\omega = \omega_s + n\delta\omega)\,, \quad n = 0, 1, 2..., N-1. \tag{4.6}$$

4.2.2 Correction to Spatial Channel Misalignment

In the off-axis holographic imager setup, the modulation frequency of fringed images is dependent on the effective in-plane momentum component and thus on the operation

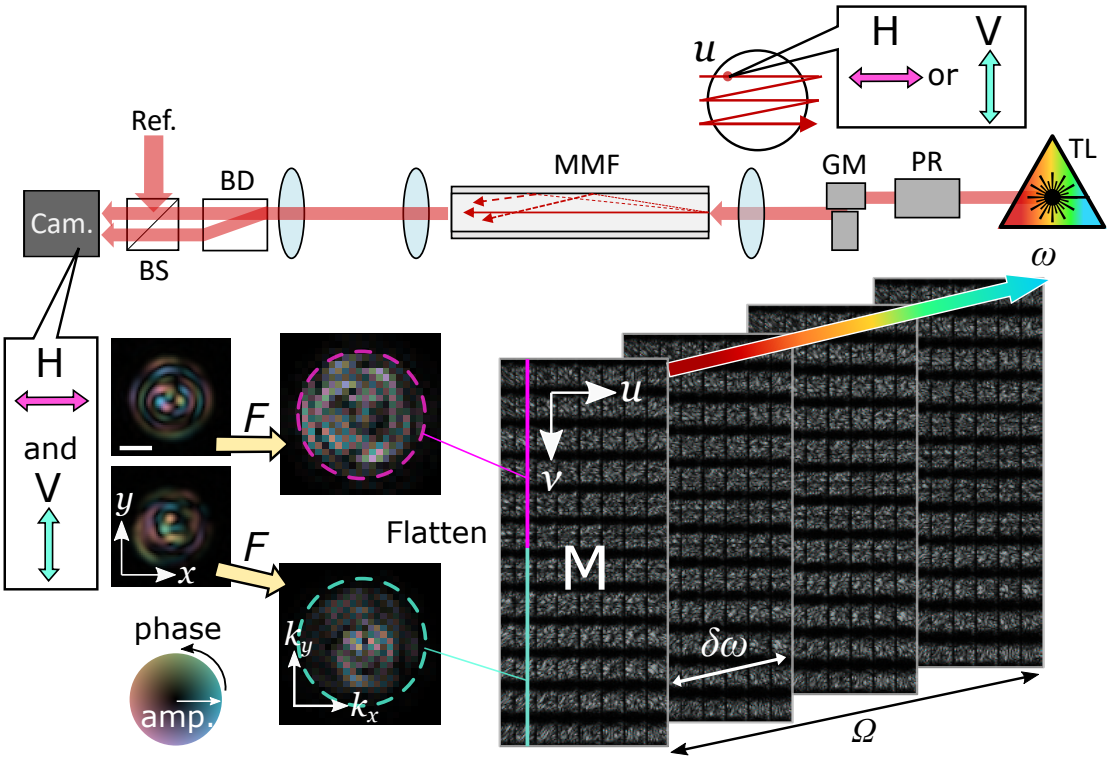

Figure 4.2.1: Measurements of the multipsectral transmission through a MMF. The fiber, though drawn as if it were straight, was in fact randomly coiled in experiments. TL: tunable laser. PR: phase retarder. GM: galvanometer scanning mirrors. BD: beam displacer. Ref.: reference wave. Cam.: camera. The focal spot is alternated between H and V by PR and scanned across the MMF input facet by GM, and the output facet is relayed onto the camera, where the two LP states are spatially separated by BD. Although the complex output mode is displayed in real space for better visual appearance, it is stored and analyzed in the Fourier domain. A subset of each TM is shown, where the colored solid vertical lines indicate the vector arranged as an output mode. The color map encodes the complex values, and the scale bar is 20 μm.

wavelength [87]. Since we recorded TMs at fixed pixels in the Fourier domain, the spatial channels were misaligned at different wavelengths. To measure a msTM through identical channels, we need to gauge the drifting modulation frequency and co-register the pixels. As shown in Fig. 4.2.2(a), we obtained multiple modulated MMF images corresponding to different input realizations at each wavelength, averaged the intensity of the images

in the Fourier domain, and isolated the corresponding interference lobes. We repeated the process at decreasing wavelength and tracked the center of the lobes across the laser spectrum. As shown in Fig. 4.2.2(b), we then fitted the center trajectory with linear regression, which informs required pixel shift in the Fourier domain for a given frequency. For each TM measured at a frequency ω, we imposed corresponding spatial channel registration, and the center position at varying frequency after the correction is shown in Fig. 4.2.2(c). While only correction to H polarized channels is shown, we conducted individual corrections to both polarization detections.

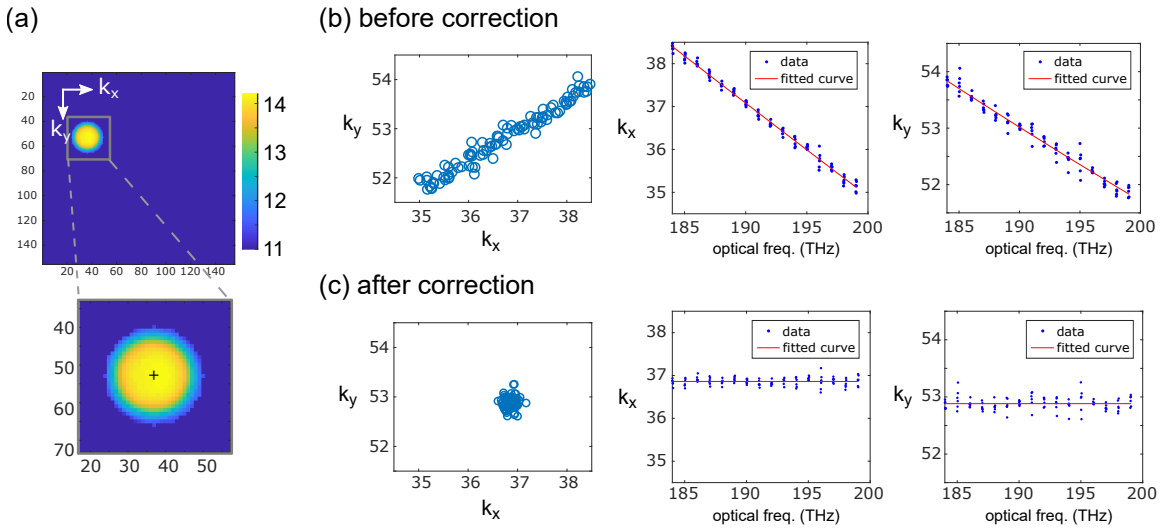

Figure 4.2.2: Correction to the drifting modulation frequency in multispectral off-axis holography. (a) The intensity of MMF outputs in the Fourier domain in logarithmic scale averaged over several input realizations at $\omega_o = 191$ THz. We extracted the interference lobe (inset) and tracked the lobe center (black cross) in terms of digitized (k_x, k_y) at varying frequency. (b) Before correction, the center shifts linearly in both k_x and k_y, where we can linearly fit the drifting. (c) After correction, the center position only fluctuates due to measurement noise.

4.2.3 Number of Modes and Matrix Correlation

The number of guided modes within the MMF can be quantified by performing singular value decomposition (SVD) on each measured TM, counting the singular values (SVs)

above a threshold defined as 5% of the largest SV. As shown in Fig. 4.2.3(a), there are ∼200 DOFs, or populated modes, in each monochromatic TM of ω within the laser tunable range, consistent with the theoretical values from a typical SI-MMF model, and the number of DOFs gradually increases with ω.

To quantify the spectral correlation between TMs at different frequencies and the full width half maximum (FWHM) bandwidth as spectral coherence length, $\delta\nu$, we defined the correlation between two matrices, $\mathbf{A}$ and $\mathbf{B}$, as the absolute value of the normalized Frobenius inner product

$$C(\mathbf{A},\mathbf{B}) = \left| \frac{\sum_{ij} a_{ij}^* b_{ij}}{\sqrt{\sum_{ij} |a_{ij}|^2 |b_{ij}|^2}} \right|, \tag{4.7}$$

where i and j are the matrix row and column indices, and a_{ij} and b_{ij} are the entries of $\mathbf{A}$ and $\mathbf{B}$, respectively. We then calculated the spectral correlation upon a $\Delta\omega$ spectral shift, $C(\Delta\omega = \omega - \omega_o) = C(\mathbf{M}(\omega), \mathbf{M}(\omega_o))$, of TMs at varying frequencies, ω, against the TM at the reference wavelength, ω_o. As plotted in the solid curves in Fig. 4.2.3(b), the original spectral correlation referenced at $\omega_o = 191$ THz manifests a fast decay with a FWHM of $\delta\nu =\sim 30.43$ GHz (∼0.26 nm), consistent with previously reported results with MMF in a similar geometry [46]. As a benchmark, we found a $98.7 \pm 0.14\%$ correlation between two repeatedly measured TMs at identical optical frequency. At first glance, the MMF has an independent transmission at spectral shift beyond $\delta\nu$ and hence low resemblance between different outputs upon even just sub-nanometer spectral perturbation.

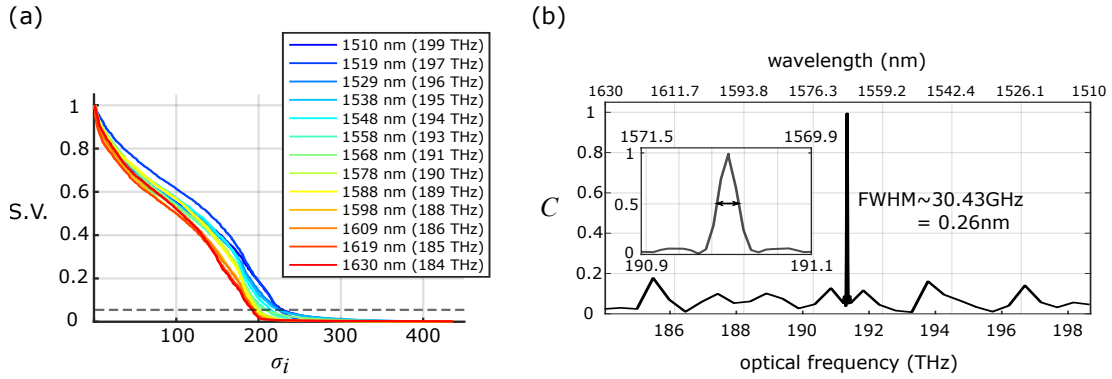

Figure 4.2.3: Characteristics of the 1m-long 50-µm-core SI-MMF (a) The number of the modes are ~ 200, determined by singular values of TMs and increases with decreasing wavelengths. (b) The spectral correlation of TMs referened at $\omega_o = 191$ THz. The original $\delta\nu = 0.26$ nm.

4.3 Constructing Dispersion Model

4.3.1 Linear Dispersion Estimation

To create a dispersion model, we first estimated first order dispersion at the reference frequency with a measured msTM at spectral sampling step size of $\delta\omega < \frac{\delta\nu}{2}$ in two steps: First, we aligned the phase offset of each complex TM in the msTM such that every consecutive pair of TMs have the same phase offset; Second, following Eq. 4.3, we computed $\mathbf{D}(\delta\omega)$ by solving a least squares optimization problem

$$\arg\min_{\mathbf{D}} \sum_{n=1}^{N-1} ||\mathbf{M}_{n+1} - \mathbf{D}\mathbf{M}_n||_F^2, \tag{4.8}$$

where $||\cdot||_F$ is matrix Frobenius norm (or L2-norm). The optimized $\mathbf{D}$ can be analytically derived

$$\mathbf{D} = (\sum_{n=1}^{N-1} \mathbf{M}_{n+1}\mathbf{M}_n^\dagger)(\sum_{n=1}^{N-1} \mathbf{M}_n\mathbf{M}_n^\dagger), \tag{4.9}$$

and forced to be unitary by making all singular values one. The overall process is illustrated in Fig. 4.3.1. With $\mathbf{D}(\delta\omega)$, we can compute $\mathbf{X}_1$ *est.* $= \text{logm}(\mathbf{D})/\delta\omega$, which serves as the initial guess for the optimization of higher order dispersion model. Alternatively, $\mathbf{D}$ can be used for fast construction of the linear dispersion model.

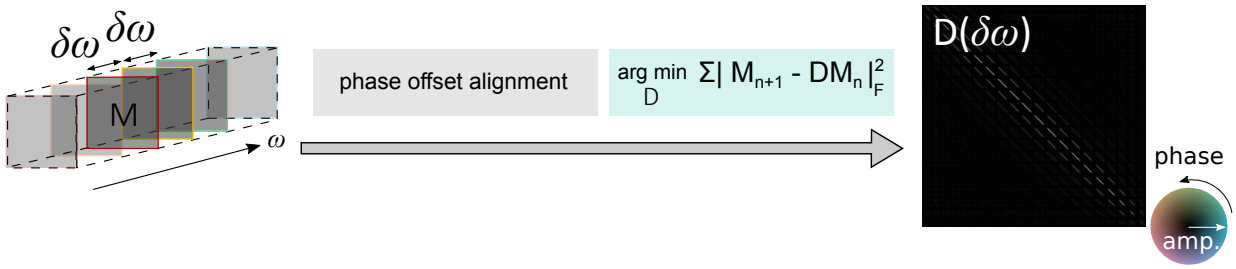

Figure 4.3.1: Data processing pipeline for linear dispersion estimation. We used a msTM with equidistant spectral step size to estimate **D** of linear dispersion.

4.3.2 Phase Wrapping Issue in Linear Model

In experiments, we measured TMs at discrete optical frequencies. To construct a dispersion model in Eq. 4 over continuous bandwidth, we need $\mathbf{D}(\omega, \omega_o)$ with correct eigenvalues without 2π phase wrapping ambiguity. With a measured msTM of small enough step size $\delta\omega$ such that the maximal phase difference of eigenvalues of $\mathbf{D}(\delta\omega)$ does not exceed 2π, we can derive the correct changing rate of individual eigenvalues (equivalent to the group delays of PMs).

To show the phase wrapping issue, we constructed two linear dispersion models of the same 1m-long 50-μm-core SI-MMF geometry with two sets of msTM measurements, respectively. The first set has two msTMs of $(\omega_s, \delta\omega, \Omega) = (190.9612, 0.0122, 0.1216)$ and $(192.3077, 0.3033, 3.033)$ THz, and the second set has two msTMs of $(\omega_s, \delta\omega, \Omega) = (190.4762, 0.0607, 0.6066)$ and $(192.3077, 0.3033, 3.033)$ THz. Note that the two sets of measurements only have difference in the spectral sampling rate of the first msTM, where the sampling rate is either above or below the Nyquist criterion. Fig. 4.3.2(a) shows the eigenvalues of $\mathbf{D}(\delta\omega)$ of the first msTM of each set on the complex plane: When above Nyquist sampling rate (top), the angular distribution of the meaningful eigenvalues does not cover the entire plane, and we can retrieve the relative phase offsets of the eigenvalues;

However, when below the Nyquist sampling rate (bottom), the eigenvalues spread all over the plane, and we cannot determine the phase offsets due to the 2π ambiguity. We then tested the two models with separately measured TMs at uncalibrated frequencies, which is associated with fractional matrix power of $\mathbf{D}(\delta\omega)$ by linearly scaling the eigenvalue phases by an real value. Fig. 4.3.2(b) shows the computational spectral correlation after dispersion compensation to the first order. When below the Nyquist sampling rate (bottom), the TM prediction at a frequency off the grid of $\delta\omega$ is inaccurate due to the incorrect phases of eigenvalues. Mathematically, if we develop the fractional matrix power in closed form by diagonalization, since we can add any integer of 2π to the phases of complex eigenvalues without changing the values, finding numerical roots based on commonly used De Moivre's Theorem may lead to a false solution if the condition is not satisfied. Generally speaking, the Nyquist rate increases with MMF length and NA, where a narrower spectral resolution of the laser source is required.

4.3.3 Fast Construction of Linear Dispersion Model

In Eq. 4.5, considering only linear dispersion, the spectral shift $\Delta\omega$ affects the eigenvalues of $\mathbf{D}$ by scaling their phases. Therefore, we can address linear dispersion in the eigenspace of $\mathbf{D}$ by finding correct phases for the corresponding eigenvalues. In practice, to create an accurate linear dispersion model with few TM measurements and without iterative optimization, we estimated individual $\mathbf{D}$s from two msTMs ($\omega_s = 190.9$ THz) of different spectral sampling rates, $\delta\omega_{large}$ and $\delta\omega_{small}$, respectively, and merged the two $\mathbf{D}$s in three procedures: First, we found the eigenspace of $\mathbf{D}$ by taking the eigenvectors of empirical $\mathbf{D}(\delta\omega_{large} = 60.6GHz)$ from the msTM with larger spectral step, which offers a higher measurement accuracy in the eigenvectors due to finite laser linewidth and system stability; Then, using these eigenvectors, we diagonalized the empirical $\mathbf{D}(\delta\omega_{small} = 2.44GHz)$ from the other msTM with smaller spectral step; Third, we extracted the phases of diagonal entries, corrected residual errors such that the phases when scaled by $\frac{\delta\omega_{large}}{\delta\omega_{small}}$ matched the

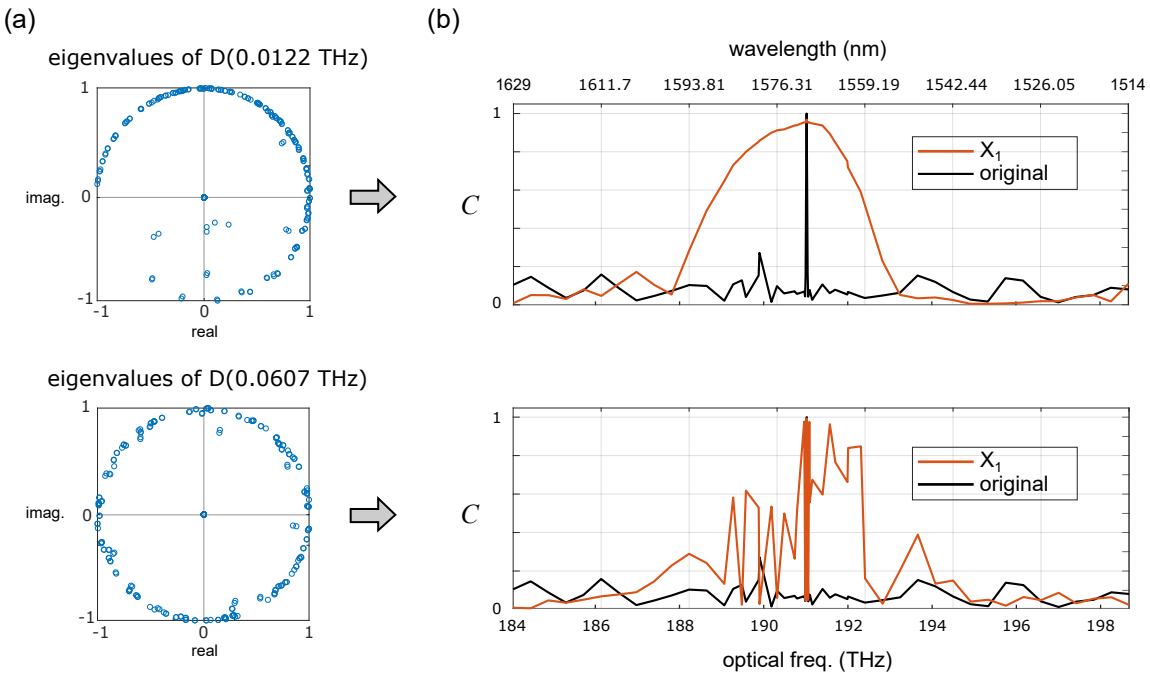

Figure 4.3.2: Evaluation of linear dispersion model with spectral sampling rate above (top) or below (bottom) the Nyquist criterion. (a) The eigenvalues of $\mathbf{D}(\delta\omega = 0.0122$ THz) distribute across three fourth of the complex plane, and the eigenvalues of $\mathbf{D}(\delta\omega = 0.0607$ THz) distribute across the entire complex plane. (b) The spectral correlation is continuous over ~30 nm, while the spectral correlation is poor in the sub-Nyquist sampling condition due to inaccurate phase estimation.

eigenvalues of $\mathbf{D}(\delta\omega_{large})$, and divided the values by $\delta\omega_{small}$. The eigenvectors and their phase changes per spectral shift determine the linear dispersion model. To compensate for linear dispersion due to a spectral shift $\Delta\omega$ and predict $\mathbf{M}(\omega)$, we calculated individual phase changes of the eigenvectors, assembled $\mathbf{D}(\Delta\omega)$ in the Fourier basis, and applied it to $\mathbf{M}(\omega_o)$. The overall process is illustrated in Fig. 4.3.3.

4.3.4 Optimization of High-order Dispersion Model

To improve the estimated dispersion model and consider higher order dispersion, we retrieved $\mathbf{X}_k$ in Eq. 4.4 up to K orders using additional msTM with large spectral step and span. While it may be intuitive to use the optimization in Eq. 4.8 again, the unknown phase

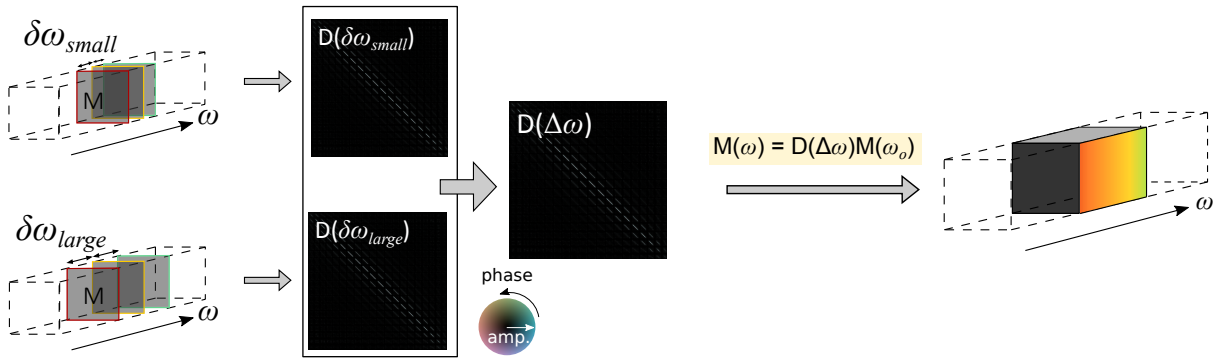

Figure 4.3.3: Data processing pipeline for fast construction of linear dispersion model. By using two msTMs of different step sizes, we can construct linear dispersion model with high accuracy and time efficiency.

offset imposed on each measured TM becomes difficult to align beyond the linear dispersion regime, jeopardizing the optimization in converging to the correct solution. Therefore, we used instead the complementary correlation, $1 - C^2$, between each pair of $\mathbf{M}(\omega)$ and $e^{\mathbf{X}(\omega,\omega_o)}\mathbf{M}(\omega_o)(\equiv \mathbf{D}(\Delta\omega)\mathbf{M}(\omega_o))$ as the metric and optimize for matrices $\mathbf{X}_k$

$$\underset{\mathbf{X}_k \in \mathfrak{g}}{\arg\min} \sum_{n=1}^{N} (1 - |tr(\mathbf{M}_n^{\dagger} e^{\sum_{k=1}^{K} \mathbf{X}_k \Delta\omega_n^k} \mathbf{M}(\omega_o))|^2), \tag{4.10}$$

where $\mathfrak{g}$ is the group of skew-Hermitian matrices, $\mathbf{M}_n$ is indexed $\mathbf{M}(\omega)$ with $\omega = \omega_o + \Delta\omega_n$ and is normalized by its own Frobenius norm, tr indicates the trace of TM products, and we summed over all N pairs of TMs. Note that the skew-Hermitian constraint on $\mathbf{X}_k$ is equivalent to unitary $\mathbf{D}$, $|tr(\cdot)|$ is the same as C, and the unknown phase offsets of TMs do not matter here anymore since the absolute norm ignores them. The constraint makes Eq. 4.10 a manifold optimization problem. We used the estimated first order dispersion $\mathbf{X}_1$ *est.* for $\mathbf{X}$ initialization, and simultaneously optimized for all $\mathbf{X}_k$. To achieve efficient computation, we employed approximated Reimannian gradient descent with an analytical gradient [84] to perform the optimization. The overall process is illustrated in Fig. 4.3.4.

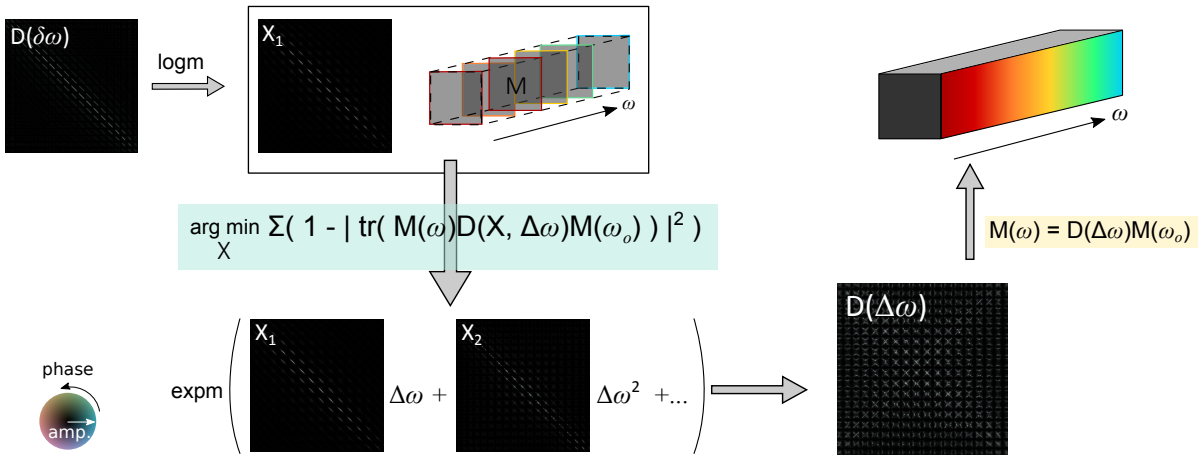

Figure 4.3.4: Data processing pipeline for optimization of high-order dispersion model. We computed $\mathbf{X}_1$ from estimated $\mathbf{D}$ and initialized the optimization process for finding higher-order dispersion, $\mathbf{X}_k$, with a msTM across large spectrum. With fitted $\mathbf{X}_k$ series, we can predict the TM at an arbitrary optical frequency.

4.3.5 Phase Wrapping Issue in Nonlinear Model

For high order dispersion optimization, we need spectral sampling over a large spectrum to measure dispersion nonlinearity. However, similar to the linear dispersion, a too small sampling rate may also result in incorrect $\mathbf{X}_k, k \geq 2$ convergence. To show this, we first compensated the linear dispersion of M(ω) and computed the eigenvalues of $\mathbf{D}(\delta\omega)$ with $\delta\omega = 0.933$ or 1.86 THz, as shown in Fig. 4.3.5(a), where the former spread only half of the complex plane, and the latter almost cover the entire plane. We then used msTMs of $N = 5$ at the two sampling rates for optimizing second order dispersion and tested the dispersion models. As plotted in Fig. 4.3.5(b), the spectral correlation with dispersion compensation to the second order is smooth over ~72 nm when using the msTM at $\delta\omega = 0.933$ THz. However, the spectral correlation is oscillating when using the msTM at $\delta\omega = 1.86$ Thz due to incorrect $\mathbf{X}_2$.

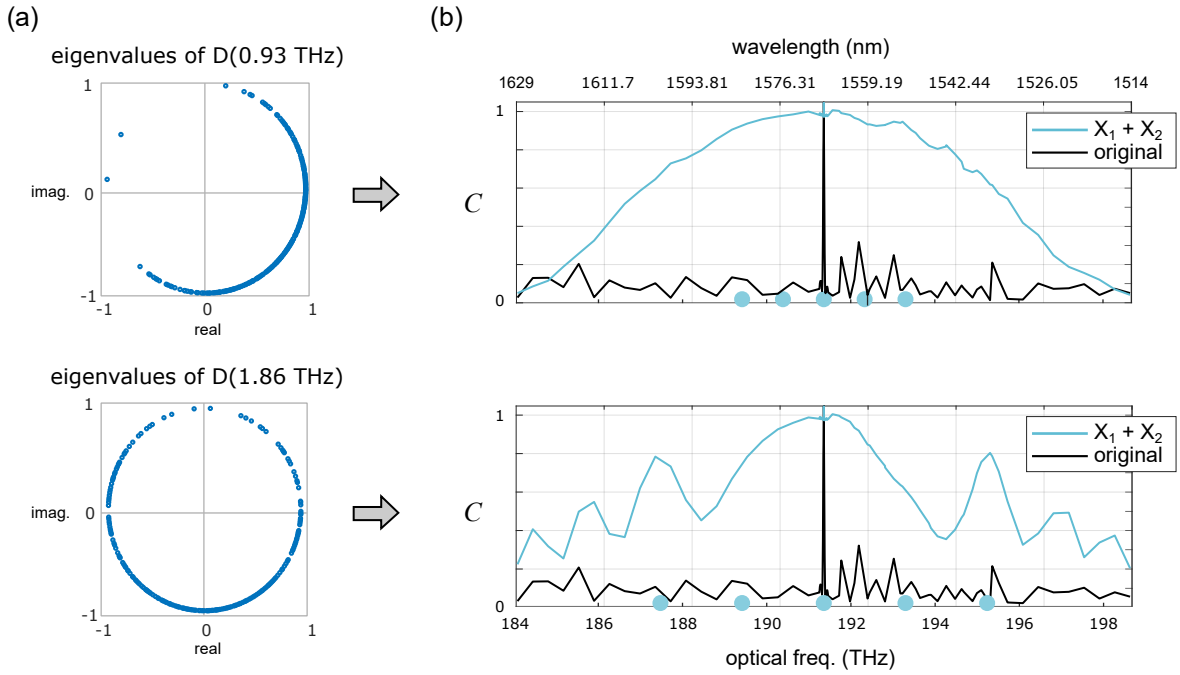

Figure 4.3.5: Evaluation of high order dispersion model with spectral sampling rate above (top) or below (bottom) the sampling criterion. (a) The eigenvalues of $\mathbf{D}(\delta\omega = 0.933$ THz) distribute across half of the complex plane, and the eigenvalues of $\mathbf{D}(\delta\omega = 1.86$ THz) distribute across the entire complex plane. (b) Accuracy of the constructed model using msTM of sampling step 0.933 (top) or 1.86 THz (bottom) for fitting the second order dispersion. The color dots label the spectral sampling points.

4.4 Ultra-wide Spectral Correlation

To create a dispersion model, we acquired two msTMs referenced at $\omega_o = 191$ THz with $(\omega_s, \delta\omega, \Omega) = (190.9, 0.01, 0.2)$ THz $(N = 21)$ and $(\omega_s, \delta\omega, \Omega) = (184, 0.467, 14)$ THz $(N = 31)$, respectively, for estimating the first order dispersion $\mathbf{X}_1$, and optimizing the higher order dispersion $\mathbf{X}_k$ (see mathematical details in Methods 4.3.1 and 4.3.4). To avoid the phase wrapping issue as explained in Section 4.3.2 and achieve a continuous model bandwidth, $\delta\omega$ of the first msTM was set to be smaller than the original spectral coherence length $\delta\nu = 30.43$ GHz. Nevertheless, the overall spectral measurements are sparse compared to the hundreds of TM measurements across 14 THz laser spectrum in the

step size of $\delta\nu$. We optimized $\mathbf{X}_k$ up to $K = 2$ orders, where the improvement on msTM fitting considering even higher order dispersion was found to be negligible after additional trials, and $\mathbf{X}_1$ has a matrix Frobenius norm 489.8 times larger than $\mathbf{X}_2$.

To validate the parametric model and evaluate the accuracy of predicted $\overline{\mathbf{M}}(\omega)$, we calculated its matrix correlation with separately measured $\mathbf{M}(\omega)$ as ground truth, $C(\mathbf{M}(\omega), \overline{\mathbf{M}}(\omega))$. To verify the spectral continuity, the frequencies of the ground truth TMs for testing are different from the fitting ones and off the grid of $\delta\omega$ referenced at ω_o by up to half of $\delta\omega$. Figure 4.4.1(a) plots the spectral correlation $C(\mathbf{M}(\omega), \overline{\mathbf{M}}(\omega))$ considering $\mathbf{X}_k$ to different K orders. We define the extended coherence length, $\delta\nu_e$, as the FWHM bandwidth of TM correlation after dispersion compensation. The coherence length is greatly improved to 33 nm considering the first order dispersion $\mathbf{X}_1$ (the orange and yellow curves are for estimation using Method 4.3.1 and thereafter optimization using Method 4.3.4 with $K = 1$, respectively), which is ∼127 times broader than the original $\delta\nu$. The initial estimation captures the linear dispersion and is quite accurate. After optimization with $K = 2$, despite the small matrix norm of $\mathbf{X}_2$, the correlation is significantly enhanced and covers the entire 115 nm (the purple curve), which is ∼442 times of the original $\delta\nu$. We also repeated the same experiment with different MMF of various types, lengths, coil radius, or from a different measurement system and observed the similar efficacy, which shows the generalization of our dispersion model (see Section 4.6).

To visually assess the dispersion model, we synthesized focusing through the MMF at test frequencies. The focus is clearly visible within 33 nm with $K = 1$ (the orange and yellow boxes), and, with $K = 2$, the entire 115 nm spectrum (the purple box). As a comparison, the original poor spectral correlation (the black curve) results in speckle patterns (the black box) when using $\mathbf{M}(\omega_o)$ to create focus at other wavelengths. We define the focus contrast (η) as the peak intensity over the average intensity of all available spatial channels, as illustrated in Figure 4.4.1 (b), and the dispersion model with $K = 2$ renders η at an example spatial channel ranging in 75–172 across the entire spectrum. We

also evaluated the correlation bandwidth of individual spatial channels by calculating the FWHM of smoothed η curve per each channel, which renders the spatial uniformity map of the model shown in Figure 4.4.1 (c). The correlation has the highest bandwidth 85 nm at the central core region and symmetrically degrades towards the cladding part ∼25 due to the more lossy transmission at the core periphery. As a result, the correlation after dispersion compensation covers all available spatial/polarization channels.

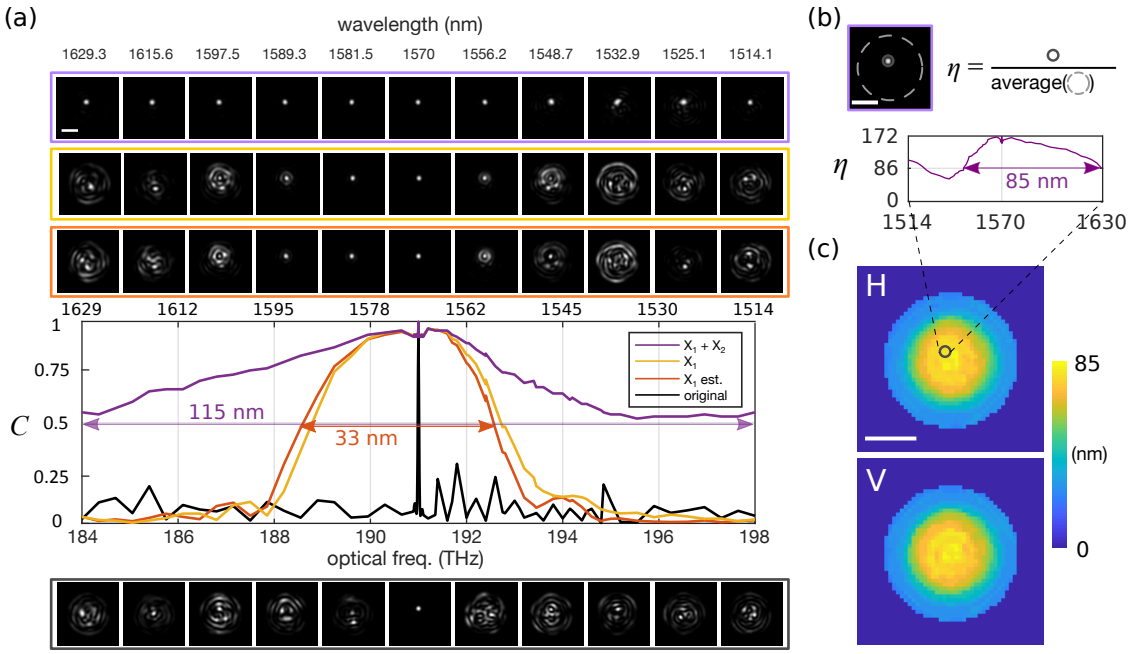

Figure 4.4.1: Ultra-wide hidden spectral correlation after dispersion compensation. (a) The black, orange, yellow, and purple plotted curves correspond to the spectral correlation of original TMs, considering dispersion with first-order estimation, first-order optimization, and second-order optimization, where the coherence lengths are $0.26, 33, 33$ and 115 nm, respectively. The insets also show corresponding synthetic focusing through the MMF at varying wavelengths (color-coded boxes), where the second order enables excellent focus contrast across the entire spectrum (purple box). (b) The focus contrast η at a spatial channel at varying wavelength with dispersion model with $K = 2$. The fiber facet is masked from the background (gray dashed circular support). (c) The spatial uniformity map of reconstructed channels at fiber core in H and V polarization. The scale bars are 20 µm.

4.5 Spectral-variant PMs

The PM theory is designed to tackle only linear dispersion, with the assumption of constant $\mathbf{m}$ matrix in Eq. 4.2. In Eq. 4.4, when $\mathbf{X}_k$ commutes to each other, i.e., $[\mathbf{X}_k, \mathbf{X}_{k'}] = 0, k \neq k'$, they share the same eigenvectors, and the PMs will maintain their profiles over the entire spectrum. However, in general, the $\mathbf{X}_k$ series are not commutative, leading to frequency-dependent $\mathbf{m}$ and high order dispersion on PMs. The evaluation of the dispersion influence on PMs is experimentally challenging due to the need for measuring MMF response to PM input coupling at all frequencies over continuous spectrum [88]. Fortunately, with the accurate dispersion model as presented in the previous section, we can numerically characterize MMF dispersion and conveniently compute for all spectral-variant PMs.

To obtain local PMs at ω, we first computed

$$\mathbf{D}(\delta\omega) = \overline{\mathbf{M}}(\omega + \delta\omega)\overline{\mathbf{M}}(\omega)^{-1}, \tag{4.11}$$

whose eigenvectors are the output PMs, and eigenvalues are associated with the group delays. To compensate for the relative optical path-length difference between the H and V polarization channels due to the use of the optical beam displacer on the detection pathway (similar to [88]), we numerically corrected the $\mathbf{D}(\delta\omega)$ by applying a defocusing operator to the V polarization channel. We then collected the first 200 eigenvectors of $\mathbf{D}(\delta\omega)$ and their eigenvalues. We repeated the process for varying frequencies ω and calculated the spectral correlation of each PM as the normalized complex vector inner product with itself at $\omega_o = 191$ THz. The group delay, τ_{pm}, of an output PM at ω is calculated by taking the phase of its corresponding eigenvalue, and dividing the value by $\delta\omega$. The fundamental mode is visually identified from its spatial profile, and the arrival time is offset to 0 ps. The PMs with spurious delays due to noisy eigenvalues are discarded.

The normalized commutativity between $\mathbf{X}_1$ and $\mathbf{X}_2$ is $|[\mathbf{X}_1, \mathbf{X}_2]|_F/(|\mathbf{X}_1|_F|\mathbf{X}_2|_F) = 0.0033$. We first computed $\mathbf{m}(\omega)$ following Eq. 4.2 and plotted the normalized commutativity

referenced at $\omega_o = 191$ THz in Fig. 4.5.1(a), where the lever-up indicates the non-commutative $\mathbf{m}$. We then studied individual PMs and defined the permanence of a PM, $\overline{C}$, as the averaged spectral correlation across the entire 115 nm spectrum referenced at ω_o. As plotted in Fig. 4.5.1(b), the permanence of the 200 PMs ranges within 0.99–0.39, where the PMs are sorted accordingly. The decreasing permanence clearly reflects the non-commutative $\mathbf{m}$ and hence the limited PM bandwidth. Figure 4.5.1(c) shows several output PMs of different permanence in both H (cyan) and V (magenta) polarization at varying wavelengths, where the stronger polarization is plotted in the large inset. Visually, the profiles resemble theoretical Laguerre-Gaussian modes in SI-MMF, and the major effect of spectral perturbation on PMs is mode mixing due to degenerate propagation speed. In Fig. 4.5.1(d), we illustrate the higher order PMs dispersion by plotting the spectral-variant group delays of individual output PMs from the corresponding eigenvalues of the group-delay operator, and time is offset by the delay of the fundamental mode. The span of the group delays is ∼52 ps, consistent with the waveguide theory. Interestingly, besides the different nonlinear delays, the PMs exhibit both positive and negative dispersion. In addition, we observed degeneracy effects (dashed circles) between PMs due to unstable eigen-solution, similar to the previous study [88]. As a result, the dispersion model enables the numerical analysis of spectral-variant PMs featuring distinctive behaviors. The PM analysis for different MMF can be found in Section 4.6.

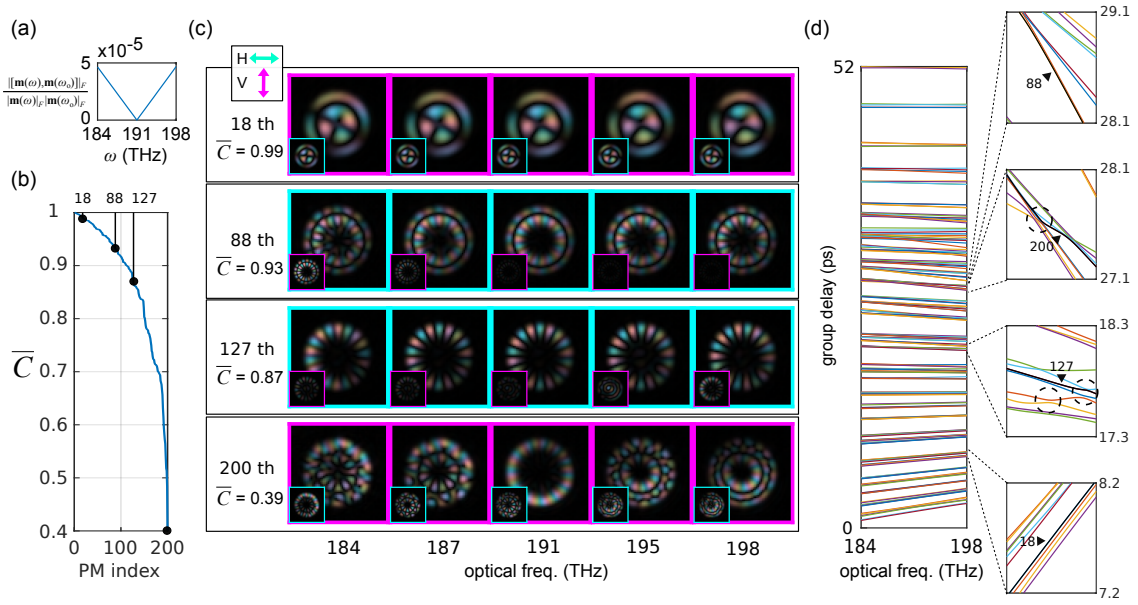

Figure 4.5.1: Characteristics of spectral-variant PMs. (a) The permanence of ordered 200 output PMs computed by averaging the spectral correlation across the entire laser spectrum. (b) Complex profiles of the 18^{th}, 88^{th}, 127^{th}, and 200^{th} output PMs in both H and V polarization and the corresponding permanence at varying wavelength. (c) The group delays of individual PMs considering higher order dispersion based on our model (left) and the zoom-in plot of different group delays of the example PMs (right). The scale bar is 20 µm.

4.6 Generalization of Spectral Memory Effect

We verified the generalizability of our parametric dispersion model by testing it on different SI- and GI- MMF, as specified in Table 4.1. For each MMF, we constructed the corresponding dispersion model by using msTMs centered at 191 THz (1570 nm). We truncated the model to the k^{th} order dispersion if no improvement was observed to the $k+1^{th}$ order. We then evaluated the dispersion model with separately measured msTMs, and calculated the spectral correlation before and after dispersion compensation. The best attainable FWHM spectral bandwidth, $\delta\nu_e$, is recorded in Table 4.1. Therefore, we concluded that the model is valid for the various MMF regardless of different refractive index profile, geometry, and length.

index	MMF spec	refractive index	core size (um)	NA	length (m)	mode #	radius of curvature (cm)	correlation BW (nm)
a	FG025LJA	SI	25	0.1	1	6	11	115
b	FG025LJA	SI	25	0.1	2	6	13	115
c	FG025LJA	SI	25	0.1	3	6	11	115
d	FG050LGA	SI	50	0.22	1	200	14	115
e	FG050LGA	SI	50	0.22	1	200	2.5	58
f	FG050LGA	SI	50	0.22	2	200	14	40
g	FG050LGA	SI	50	0.22	3	200	14	1.5
h	GIF625 (OM1)	GI	62.5	0.275	1	300	11	110
i	GIF625 (OM1)	GI	62.5	0.275	3	300	11	8
j	GIF50E (OM4)	GI	50	0.2	10	200	14	0

Table 4.1: Specifications and correlation bandwidths of various MMFs

4.6.1 Spectral Memory in Few-mode Fiber

With the corresponding constructed dispersion model of different MMF, we computed and studied the characteristics of their spectral-variant PMs. Here we show two representative results of the 1m-long few-mode fiber (FMF, indexed as "a" in Table 4.1) and the 1m-long GI-MMF (indexed as "h"). For the FMF, as shown in Fig. 4.6.1(a), we achieved a correlation above 0.8 over the full 115 nm spectrum after the dispersion compensation to the third order, whereas the original correlation has multiple lobes and a coherence length of $\delta\nu = \sim$0.06 THz. We identified 6 PMs in the FMF, with the corresponding permanence and mode profile shown in Fig. 4.6.1(b) and (c), and the PMs degenerate into H and V polarization. The group delays have a range of $\sim$1.4 ps.

4.6.2 Spectral Memory in Graded-index Fiber

For the GI-MMF, as shown in Fig. 4.6.2(a), the correlation with estimated linear dispersion (orange curve) has a pyramid shape, different to that in SI-MMFs. This is observed in other GI-MMFs and may be due to the parabolic refractive index profile and propagation properties. Nevertheless, we achieved 110 nm correlation bandwidth after

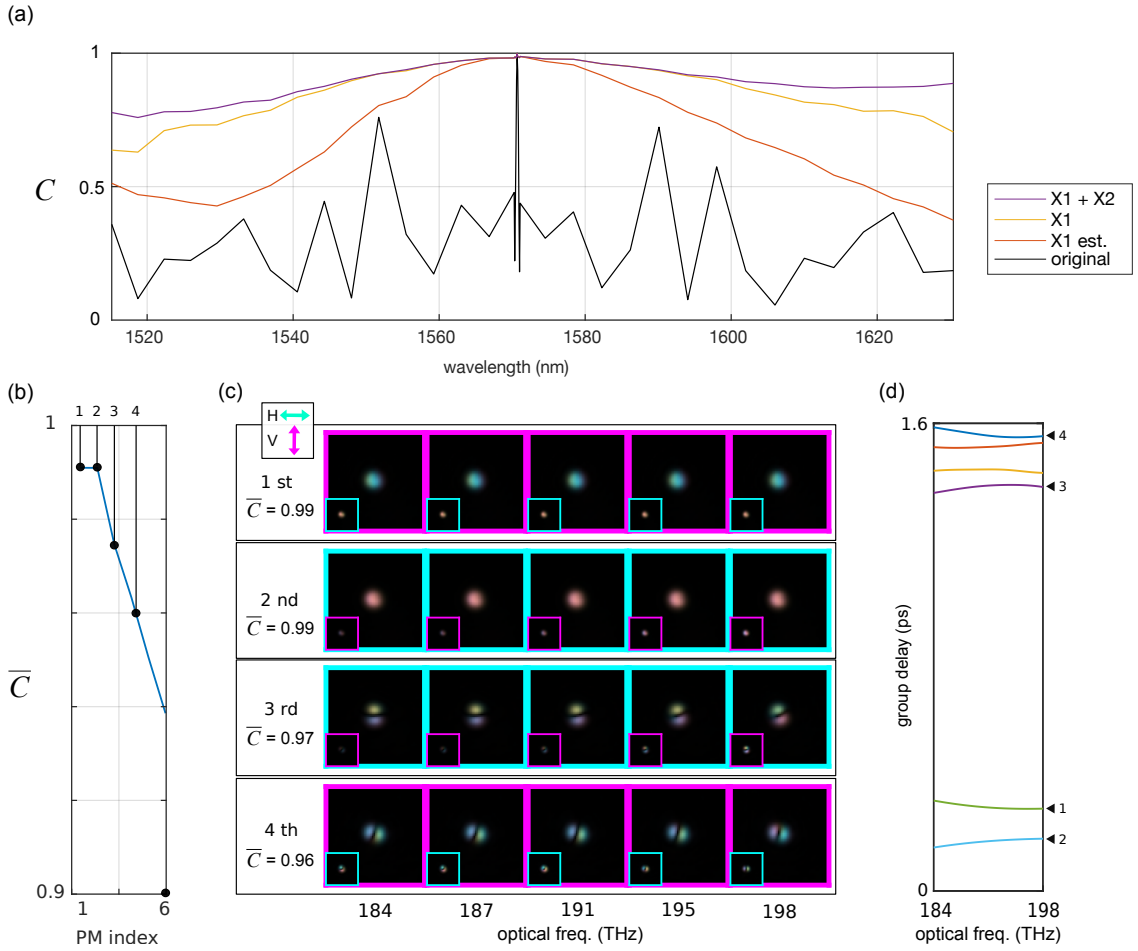

Figure 4.6.1: Computational spectral correlation in the 1m-long few-mode MMF ("a" in Table 4.1). (a) The spectral correlation before and after dispersion compensation to different orders: The orange is with initial linear dispersion estimation; The yellow is with first order dispersion optimized; The purple is with correction to the second order. (b) The permanence of the 6 spectral-variant PMs. (c) The complex profile of selected PMs across varying frequency (d) The group delays of individual PMs, with zoom-in on the selected PMs. The scale bar is 20 μm.

the dispersion compensation to the third order. The permanence of each PM is shown in Fig. 4.6.2(b), where the average permanence is much reduced compared to the 1m-long 200-mode SI-MMF (indexed as "d") due to strong mode mixing and degeneracy within each mode group. We visualized the PM profiles in Fig. 4.6.2(c), which are scrambled speckle patterns instead of theoretical Hermite-Gaussian modes. The group delays are plotted in

Fig. 4.6.2(d) and span across ∼5 ps. The results are consistent with theory and literature [45, 88], but the computational methods here avoid extensive experimental measurements.

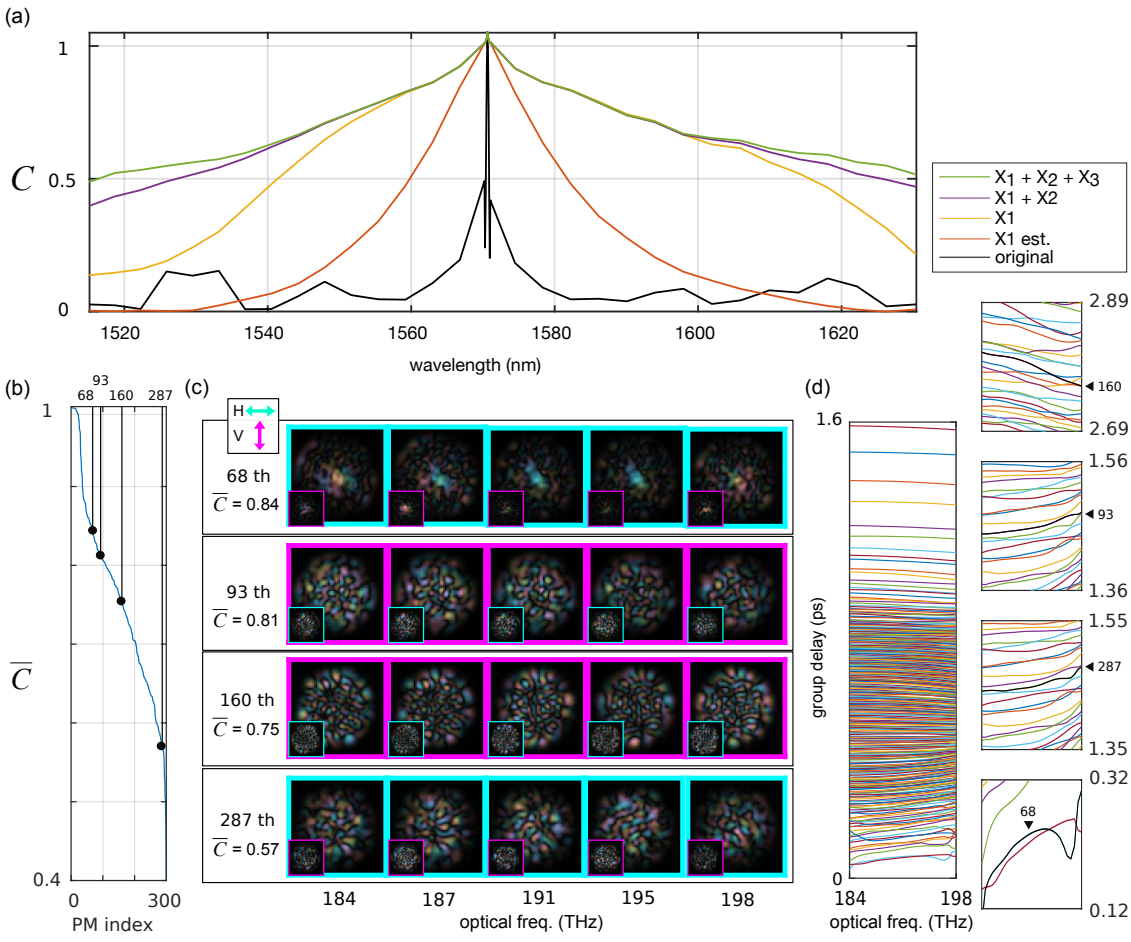

Figure 4.6.2: Computational spectral correlation in the 1m-long GI-MMF ("h" in Table 4.1). (a) The spectral correlation before and after dispersion compensation to different orders: The orange is with initial linear dispersion estimation; The yellow is with first order dispersion optimized; The purple is with correction to the second order; The green is with correction to the third order. (b) The permanence of the 300 spectral-variant PMs. (c) The complex profile of selected PMs across varying frequency (d) The group delays of individual PMs, with zoom-in on the selected PMs. The scale bar is 20 µm.

4.7 Efficient Reconstruction of Spatio-spectral Channels

So far, we derived the dispersion model, revealed an underlying spectral correlation beyond the PM bandwidth, and studied spectral-variant PMs. However, the data acquisition time scales with the number of measurements, and TM measurements are prone to perturbation on MMF such as bending or temperature change [89, 90]. Efficient msTM reconstruction with fewer measurements may thus be important for practical applications. Here, we investigate the trade-off between the number of calibrations, h, and the TM reconstruction fidelity in two conditions to develop speed- or bandwidth-efficient calibration scheme. All results are tested using other independently measured msTMs as ground truth.

4.7.1 Speed-driven

The iterative optimization for solving high order dispersion may take tens of minutes to reach convergence. In applications where speed overweighs the bandwidth, fast construction of linear dispersion from a minimal number of measurements will be desirable. We therefore developed an analytical framework for reconstructing TMs considering the first order dispersion by using two msTMs, each having N spectral steps but different $\delta\omega$ (see Methods 4.3.3). The number of total TM measurements was $h = 2N - 1$ (subtracted by 1 because of a duplicated TM at ω_s), and the post processing only took few seconds to complete. As plotted in Fig. 4.7.1(a), the spectral correlation using $h = 21$ measurements (green curve) is smooth and has a $\delta\nu_e = 34$ nm. On the contrary, the spectral correlation using only $h = 3$ measurements (blue curve) achieves a $\delta\nu_e = 10$ nm, which greatly reduces the measurement effort. We selected $(h, \delta\nu_e) = (5, 30)$ to strike a balance (orange curve), which has the best efficiency ($\delta\nu_e/h = 6$ nm) and relaxes the effort by a factor of 23 compared to the brute force approach: msTM measurement with original coherence length $\delta\omega$ as spectral step (efficiency $\delta\nu/1 = 0.26$ nm). The insets visualize the reconstruction accuracy corresponding to different h with synthesized focusing through the MMF (blue,

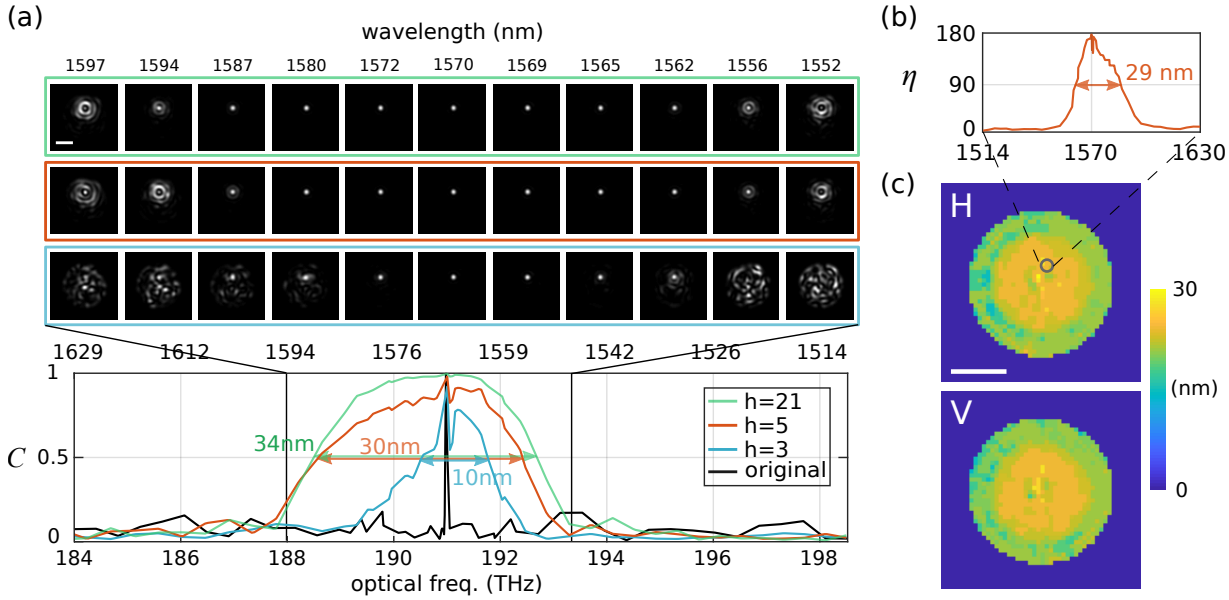

Figure 4.7.1: Efficient TM reconstruction with dispersion model to the first order. (a) The spectral correlation of MMF transmission and focusing through MMF using $h = 3, 5, 21$ number of TM measurements. With $h = 5$, we computed (b) the focus contrast η at each spatial channel at varying wavelength, and (c) the spatial uniformity map of reconstructed channels in H and V polarization. The scale bars are 20 µm.

orange, and green boxes). With $h = 5$, we computed the focus contrast at individual channels, as exemplified in Fig. 4.7.1(b), and plotted the spatial uniformity map in Fig. 4.7.1(c). The model covers all available channels with bandwidth varying from $24 - 28$ nm at the center of fiber core to ~20 nm at the periphery.

4.7.2 Bandwidth-driven

In applications where speed is less prioritized, we consider high order dispersion to attain broader bandwidth coverage. In a separated experiment, we first constructed linear dispersion model using 5 TMs following the aforementioned speed driven approach, and then selected subsets ($N = 4, 8,$ or 12) from the msTM of $(\omega_s, \delta\omega, \Omega) = (184, 0.933, 7)$ THz to optimize dispersion to the second order. As a result, we have $h = 5 + N$. The spectral sampling rate $\delta\omega$ here is determined to avoid phase wrapping issue in high order

$\mathbf{X}_k$ (see Section 4.3.5). Figure 4.7.2(a) plots the spectral correlation and extended coherence length with varying h and the corresponding spectral points for optimization. We chose $h = 13$ ($\delta\nu_e/h = 8.53$ nm), which gives the best bandwidth efficiency and is 32.8 times more efficient than the brute force measurement approach. Similar to Fig. 4.7.1, the insets visualize the reconstruction accuracy corresponding to different h. The focus contrast using $h = 13$ is exemplified in Fig. 4.7.2(b), and the spatial uniformity map is plotted in Fig. 4.7.2(c). The model bandwidth varies from $70 - 110$ nm at the center of MMF core to $\sim$23 nm at the periphery.

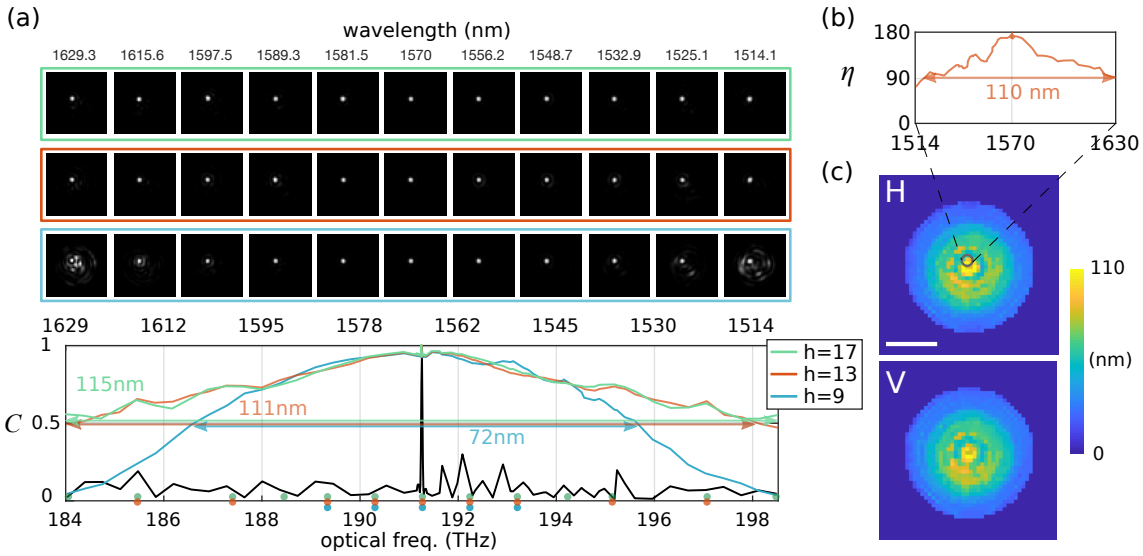

Figure 4.7.2: Efficient TM reconstruction with dispersion model to the second order. (a) The spectral correlation of MMF transmission and focusing through MMF using h number of TM measurements. The colored dots are the selected frequencies for optimization corresponding to h. With $h = 13$, we computed (b) the focus contrast η at each spatial channel at varying wavelength, and (c) the spatial uniformity map of reconstructed channels in H and V polarization. The scale bars are 20 µm.

4.8 Discussion

We established an architecture modeling the dispersion in MMF transmission based on exponential mapping, which recaptures local dispersion structure. The model not only

accommodates PM theory under linear dispersion, but also enables efficient parameterization of high order dispersion beyond the PM regime. The discovery of the surprisingly wide spectral correlation after dispersion compensation may shed new light on the traditional concepts of transmission through complex media, prompting the need for re-definition of spectral DOFs in MMF based on, e.g., statistical analysis on the matrix $\mathbf{X}$.

While the results are promising, the optimal spectral sampling rates and number of TM measurements subject to different noise levels still need in-depth explorations. For example, high spectral sampling rate is needed to estimate first order dispersion of longer MMF, which relies on narrower laser linewidth. Wavelength accuracy, repeatability, and system stability will also directly influence the fidelity of msTM measurement. On the other hand, when finding high order dispersion, non-convex optimization may lead to local minimum and be a potential limitation in constructing a dispersion model. While the convexity of Eq. 4.10 can be verified with definiteness of the corresponding Hessian matrix, such calculation is challenging, and the result may also depend on the data structure. Furthermore, similar to other optimization problems in machine learning tasks, overfitting may be another issue and impact the model accuracy. Therefore, existing techniques such as stochastic gradient descent, momentum, re-initialization, early stopping, and regularization could be helpful in optimizing high order dispersion.

Temporal focusing through MMF with arbitrary delays has been demonstrated by exploiting measured msTMs [91], where the MMF of the same geometry as here was fully characterized over a similar spectrum with more than a thousand TM measurements. Recently, a rapid multispectral transmission characterization system based on hyperspectral imaging has been introduced [92], which accelerated the data acquisition by nearly 2 orders of magnitude. Beneficially, our computational dispersion-model-based calibration method may relax hardware complexity and bring extra flexibility in system design by avoiding complicated optics such as microlens array and grating, and reduce data storage, e.g., by using only tens of measured TMs to calibrate the MMF transmission over 115 nm

spectrum. Combined with a compressive sensing technique for TM measurement [93], real-time reconstruction of chromatic transmission through MMF may be possible. The computational method can be readily replicated and facilitate calibration for MMF-based spectroscopy and nonlinear endoscopy [35, 94]. In addition to MMF-based applications, efficient multispectral calibration has great potential for multiphoton or multicolor bio-imaging, where the calibration time is critical for delivering ultrashort pulses into scattering tissues *in vivo*, and also holds promise for both fundamental and applied studies of the light transport in complex media such as in mesoscopic physics.

In free space propagation, the Fresnel diffraction theory corresponds to a diagonal $\mathbf{D}$ matrix in the Fourier basis modeling the dispersion, with quadratic defocus phase term on the matrix main diagonal. Interestingly, in transmission through the 1-m-long SI-MMF, reshaping the main diagonal of $\mathbf{D}$ to 2D spatial coordinates in the Fourier domain leads to a pattern similar to a quadratic phase front. This indicates that the MMF dispersion is associated with a defocusing effect, another observation of the chromato-axial ME. Nevertheless, the $\mathbf{D}$ matrix of the MMF has non-negligible off-diagonal elements, signifying the complicated cross-coupling between spatial channels upon spectral perturbation. While the chromato-axial ME is valid across only few nanometers in straight MMF of several centimeters long [95], our method compensates for additional waveguide dispersion and achieves orders of magnitude broader coherence bandwidth in full channels of meter-long MMF with random coiling.

In optical communication systems, MMF features throughput and cost advantages over single mode fiber (SMF), and space-division and wavelength-division multiplexing (SDM and WDM) with MMF have recently been proposed to surpass the Shannon capacity limit of data delivery in single optical fiber [96–98]. The created model can resolve dispersion in the transmission through MMF and may benefit SDM and WDM in the following ways: Combined with wavefront-shaping techniques on the transmitter side, the efficient fiber calibration may facilitate physical generation of arbitrary state at multiple

wavelengths in parallel, or temporal pulse shaping for delivering signals that is favorable to detection; Alternatively, to economize resources on the transmitter side, the efficient TM reconstruction can be applied on the receiver side and expedite multispectral digital signal processing (DSP). As shown in Supplementary Materials, we have also achieved broad spectral correlation bandwidth in different GI-MMFs, which have even higher number of guided modes than the SI-MMF here. Therefore, we expect the computational method to be suitable for GI-MMF in current SDM applications.

4.9 Conclusion

In this chapter, we created a parametric dispersion model of transmission through MMF, which may bring new insights to the design of multispectral imaging and sensing techniques with complex media, where the independent spectral DOFs are previously overvalued and may need re-evaluation. Furthermore, the demonstrated computational spectral correlation dramatically reduced measurement redundancy by an order of magnitude and led to bandwidth- or speed-driven calibration approach, which may streamline multispectral characterization of photonic systems in many applications.

Randomness is the true foundation of mathematics.

— Gregory Chaitin

5

Depth Ranging by Random Encoding with MMF

Contents

Computational imaging with random encoding patterns obtained by scattering of light in complex media has enabled simple imaging systems with compelling performance. Here, we extend this concept to axial reflectivity profiling using spatio-temporal coupling of broadband light in a MMF to generate the encoding functions. Interference of light

transmitted through the MMF with a sample beam results in path-length-specific patterns that enable computational reconstruction of the axial sample reflectivity profile from a single camera snapshot. Leveraging the versatile nature of MMFs, we demonstrate depth profiling with bandwidth-limited axial resolution of 13.4 µm over a scalable sensing range reaching well beyond one centimeter. These results have been published in Optics Express [99].

5.1 Random Encoding with Complex Media

Integration of computational reconstruction into the process of image formation can offer increased measurement flexibility compared to conventional imaging systems whose performance generally depends on well-engineered optics [100, 101]. Shifting accurate design requirements from the optical and mechanical domains to the entire imaging process including computational reconstruction may drastically mitigate physical measurement limitations and stimulate the advent of simpler or more efficient imaging systems [100, 102]. Complex or disordered media that generate random patterns to serve as encoding functions for computational reconstruction have been shown to enable imaging with improved lateral resolution [103–105], extended field of view [103, 106], increased depth of focus [107], of 3D objects [108, 109], at multiple wavelengths [110], with higher frame-rate [111], or at X-ray wavelength [112], which otherwise cannot be achieved without substantially more sophisticated hardware. In a similar fashion, random temporal fluctuations have been exploited for temporal ghost imaging [113–116]. Despite these advances, strategies for encoding the axial dimension are scarce.

Here we demonstrate a new strategy for axial reflectivity profiling by computational coherence gating with micron-scale resolution and centimeter-long sensing depth. Using broadband light, the closely spaced yet distinct propagation constants of the MMF's various spatio-temporal modes yield a set of spatially distributed encoding functions, which can be reshaped into a random encoding matrix (REM) and serve for depth referencing. Interference with a sample signal that is delayed by reflection at a specific sample depth only

occurs for the path-length-matched encoding function, creating a distinct speckle pattern unique to this exact depth position. A general one-dimensional (1D) sample reflectivity profile produces the linear superposition of the associated speckle patterns. By calibrating the random encoding functions, the 1D sample depth profile can be computationally reconstructed from a single recording of the interference pattern without the need for any mechanical or optical scanning. We demonstrate proof-of-concept axial profiling with a sensing depth range scaling from several millimeters to well beyond one centimeter by varying the physical length of the MMF, relaxing the challenging hardware requirements of achieving similar performance with conventional spectrometer-based coherence gating.

5.2 MMF Generated Random Encoding Matrix

5.2.1 Experimental Setup

To create a broadband light source with sufficient power, we cascaded two semiconductor optical amplifiers (SOAs) and obtained a broad bandwidth (65 nm FWHM) centered at 1290 nm with 10 mW. Light from the short-temporal-coherence broadband source is split into a sample and a reference arm, as shown in Fig. 5.2.1. In the sample arm, light is guided through single mode fiber (SMF) and a circulator to a sample, with an average power of 3.8 mW after collimation. The same fiber receives the backscattered light that is coupled back into the same single spatial mode. In the reference arm, light is guided through SMF and a circulator to reflect off a gold-coated mirror. The light coupled back into the same single spatial mode is then delivered to a segment of step-index MMF (core dia. = 105 µm, 0.22 NA, Thorlabs). Light emerging from the SMF in the sample arm and the MMF in the reference arm interferes in an off-axis configuration for holographic recording, where the reference light is offset by a chromatic phase tilt with respect to the sample light by means of a plane ruled reflective blazed grating (60 lines/mm, Richardson Gratings). Only the first diffracted order of the reference light is intercepted to interfere

with the sample light. Each wavelength in the reference arm receives from the grating the same offset in transverse momentum, thereby resulting in a modulated interference pattern with a constant modulation frequency independent of wavelength. The modulated interference pattern is recorded with an InGaAs camera (OW1.7-VS-CL-LP-640, Raptor Photonics) with an integration time of 2 ms after passing through a linear polarizer. Digital processing of each captured frame isolates one of the two complex-valued interference terms directly in the in-plane momentum domain within a circular aperture of radius k_r and offset from the zero frequency by k_0. Whereas k_r is imposed by the NA of the MMF, k_0 comes from the grating-induced phase tilt. The single detected polarization state corresponds to $\sim$790 theoretically available modes in the MMF. In our experiments, MMF segments of 206 cm, 54 cm, or $54 + 152$ cm in length have been used in the reference arm.

During an initial REM calibration procedure, interference patterns are recorded for varying path length offsets between a gold-coated mirror in the sample arm and the reference arm mirror, which is translated with a stepping stage (SGSP20-20, Sigma-Koki) at a sampling step size dz. A neutral density filter, measured to provide 32.7 dB double-pass attenuation, was inserted in the sample arm to avoid camera saturation. Each interference pattern corresponds to an independent realization of a random speckle pattern if its path length differs by more than the source coherence length from other path lengths. To guarantee a continuous sensing range, dz was set below the coherence length. Rearranging column by column the ensemble of vectorized random encoding functions recorded over the translation range of the stepping stage provides a REM that represents the linear transformation from the sample depth space to the encoding space.

The REM of MMF here has some similarities with the TM introduced and elaborated in the previous chapters: they are both complex matrices with columns of vectorized speckle pattern images, and DOFs confined by the number of modes supported by the MMF. However, a REM is measured with a broadband light source and a single input realization of the MMF. Each column of REM corresponds to light at a certain optical

path length. On the other hand, a TM is measured with monochromatic laser light source and complete input realizations of the MMF. Each column of TM is the interference of light propagating through all possible optical paths from a certain input realization. In Chapter 4, we introduced multispectral TM (msTM), which is a 3D matrix comprising TMs at each spectral step. As an alternative to the direct measurement described here, if we slice a msTM along the spectral dimension at an MMF input realization, and convert the row basis from spectral to time domain (which can then be scaled to optical path length), we can also acquire the corresponding REM to the input realization. Figure 5.2.2 illustrates the relationship between msTM, TM, and REM.

5.2.2 Imaging with Random Encoding Matrix

Due to the short-temporal-coherence source, the sample light from depth z only interferes with the guided modes in the reference arm that have matching path length $2z$. The interference patterns, $\vec{\nu_s}$, can be modeled as

$$\vec{\nu_s}(k_x, k_y) = \iint A(k)\, dk\, dz \cdot \sum_n \phi_n(k_x, k_y, k) e^{i\beta_n(k)L} f(z) e^{-2ikz}, \tag{5.1}$$

which describes the interaction between the reflectivity profile $f(z)$ and the guided PIMs ϕ_n as a function of coordinates in the in-plane momentum domain, k_x, k_y and wavenumber k with corresponding propagation constants β_n traveling along a MMF with physical length L. $A(k)$ is the source power spectrum. Eq. 5.1 assumes straight MMF for simplicity and no modal cross-talk along the fiber. In this study, we measured the interference pattern directly in the in-plane momentum domain and converted it into a column vector for image reconstruction. An example of a REM obtained with a 54 cm long MMF in the reference arm and $dz = 10$ µm as well as a few constituent random encoding functions are shown in Figs. 5.2.3(a) and 5.2.3(b).

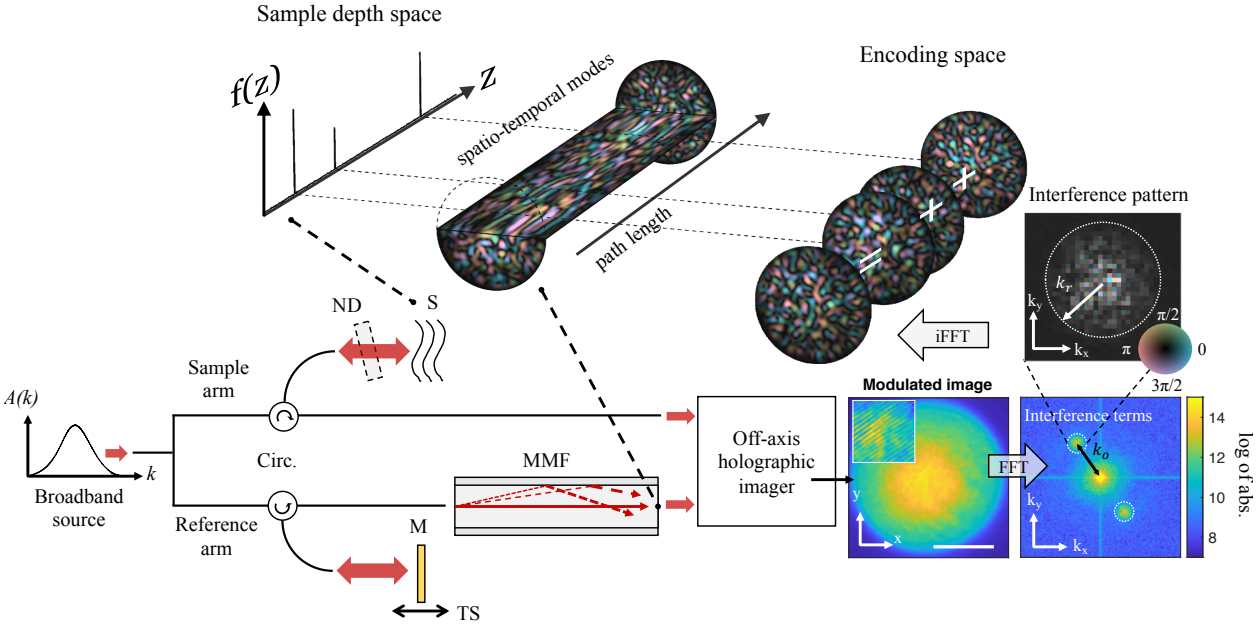

Figure 5.2.1: Schematic view of the axial profiling system with MMF-generated random encoding functions. Circ.: Circulator. M: Mirror. TS: Translational stage. ND: Neutral density filter (only present in MMF calibration and characterization phases). S: Sample. All light coupled from fiber to free space is collimated. The off-axis holographic imager comprises image relay optics, a reflective grating, and a camera. The MMF facet is relayed onto the reflective grating for chromatic phase offsetting, and the first-order diffracted light is relayed onto the camera. In the other interferometer arm, the sample light is expanded before combination with the reference light to match the image of the MMF facet for holographic recording. The inset panels show a modulated interference pattern in pixels in the camera coordinates and in the in-plane momentum domain, respectively. The scale bar in the inset is 50 µm. The off-axis configuration allows isolating one of the two interference terms directly in the momentum domain to define a random encoding function during the REM calibration phase (sample is a mirror) or to encode the sample depth profile during imaging. The color map encodes complex values.

Mathematically, the 1D reflectivity depth profile of the sample $\vec{\nu_d}$ is transformed by the random encoding functions that constitute the REM into a column vector $\vec{\nu_s}$:

$$\vec{\nu_s} = \mathbf{M}_{REM}\, \vec{\nu_d}, \tag{5.2}$$

where $\vec{\nu_s}$ is obtained by vectorizing the measured sample interference pattern in the momentum domain acquired from a single camera snapshot. To analytically reconstruct an

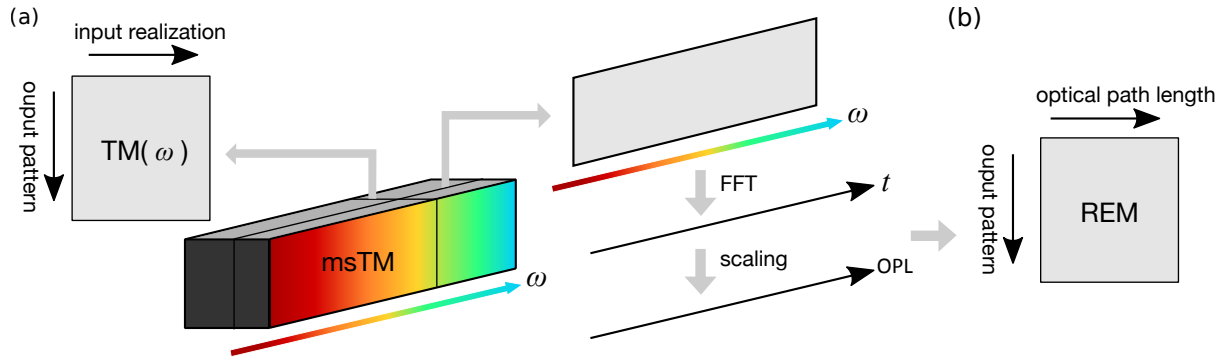

Figure 5.2.2: (a) A 3D msTM is assembled by stacking monochromatic 2D TMs at varying wavelength along the spectral dimension. We can slice a 2D matrix from the msTM along the spectral dimension at an input realization. By converting the spectral basis to temporal basis based on Fourier Transformation and scaling to optical path length (OPL), we can derive a corresponding (b) REM at the input realization.

estimate of the underlying sample reflectivity profile, ideally, we would need the inverse of the REM. However, the true inverse of a matrix only exists when the matrix is non-singular. Our measured REM, in general, is non-square and is further corrupted by noise. As a result, we resorted to signal reconstruction by using approximated matrix inversion such as Hermitian transpose or Tikhonov regularization. The Tikhonov regularization parameter was chosen as 7% of the greatest singular value based on Picard plot, L-curve, and generalized cross-validation methods [47].

5.2.3 Sensitivity Matrix

To see how the light coupled into the MMF in the reference arm populates different guided modes, we computed the energy of individual random encoding functions, which corresponds to the square of the Euclidean norm of the column vectors in the calibrated REM. The energy trace visualizes the energy distribution among the random encoding functions. We interpreted the axial range within 1% to 99% of the total axially integrated energy as the axial sensing depth range. Moreover, SVD analysis of the calibrated REM enables inspection of the available DOFs. The 7% cutoff from the Tikhonov regularization

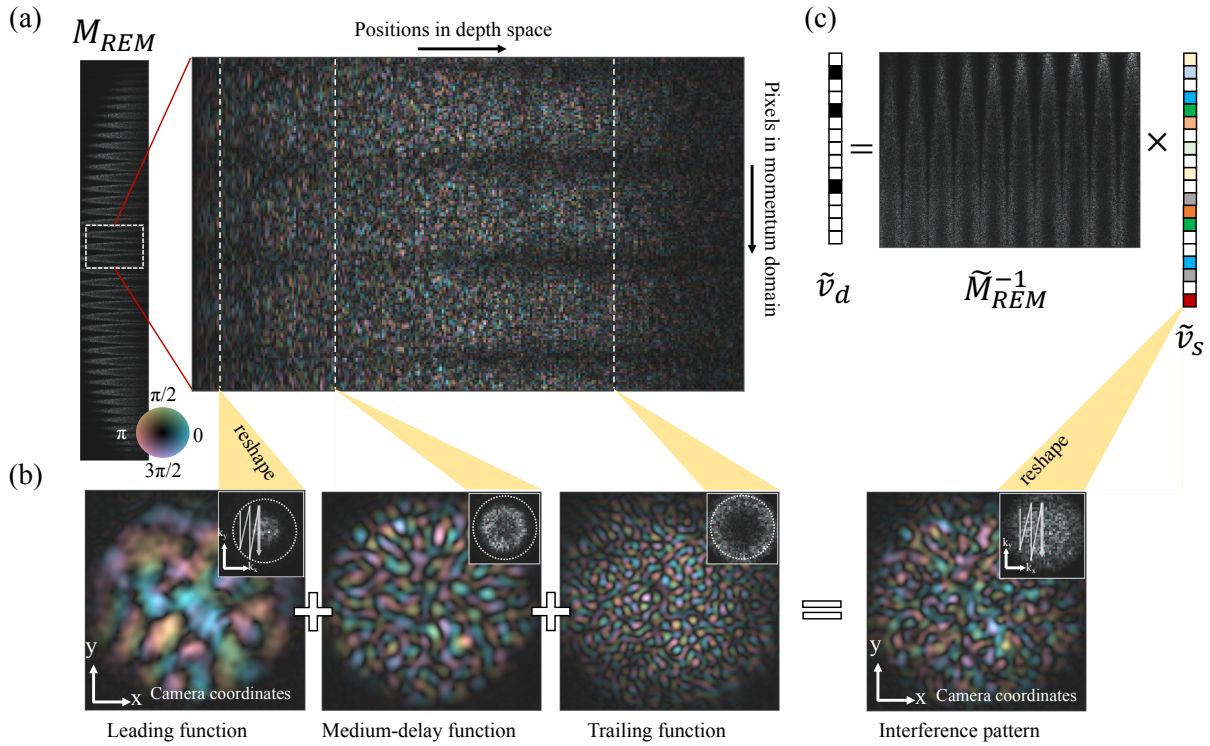

Figure 5.2.3: (a) An experimental random encoding matrix (REM) with rows indexed in the vectorized momentum domain and columns indexed in the axial sample positions ($dz = 10$ µm). The color map encodes complex values. (b) Three examples of random encoding functions. By transforming the interference term from the momentum domain back to camera coordinates, we can visualize the spatial profile of the corresponding random encoding function. The inset of each function shows the interference term in the momentum domain, which is vectorized to form a column of the calibrated REM. The leading function comprises low-order guided modes that experience the shortest path length and encode shallow sample depth. In contrast, the trailing function comprises high-order guided modes, which experience a longer path length and encode deeper sample information. (c) Obtained by a single snapshot, an REM-encoded reflectivity profile is represented by a column vector $\tilde{\nu}_s$, which is a vectorized interference pattern in the momentum domain that equals the superposition of random encoding functions weighted by the reflectivity profile, and tilde indicates the measured quantities. The corresponding complex field in camera coordinates is also shown. Applying the approximated inversion of the calibrated REM, $\tilde{\mathbf{M}}_{REM}$, to the column vector $\tilde{\nu}_s$ reconstructs the 1D reflectivity profile $\tilde{\nu}_d$.

determines the number of meaningful singular values, which is related to the number of populated guided modes. We further defined as a sensitivity matrix (**S** Matrix) the product of the approximated inverse of the REM with a second identically but independently

calibrated REM. The columns of the sensitivity matrix reveal the axial position of the calibration mirror for each recorded position, subject to both calibration and measurement noise. Hence, the sensitivity matrix should be close to the identity matrix such that the reconstructed sample depth profile corresponds to the ground truth. The properties of the sensitivity matrix entirely define the performance of the depth profiling system. The on-diagonal energy of the sensitivity matrix reveals the system's signal roll-off, specifying how fast the signal level drops with increasing depth owing to the larger propagation loss of higher-order modes. On the other hand, the off-diagonal elements of the sensitivity matrix define the background signal, composed of residual correlations and noise. For quantitative evaluation, we averaged the energy of the matrix elements in the off-diagonal bands separated 2 to 8 coherence lengths from the matrix diagonal in row-wise direction. The ratio between the on-diagonal and the off-diagonal energy of the sensitivity matrix at an axial position expresses the SNR of the attenuated mirror reflection at that depth. Considering the double-pass attenuation of the neutral density filter, 32.7 dB, offers a measure of system sensitivity by comparing the noise level to the hypothetical signal of a perfect reflector.

5.3 Imaging Performance Characterization

To leverage the random encoding functions generated by a MMF for imaging axial reflectivity profiles, it is crucial to understand how the spatio-temporal coupling and modal delay in the fiber structure the REM. To investigate these characteristics, with the neutral density filter and the gold-coated mirror placed in the sample arm, we examined the energy distribution, the sensitivity matrix, and residual correlation among the encoding functions while varying physical parameters such as coupling regime, mode mixing, and MMF length, before performing proof-of-principle sample imaging of custom-made phantoms.

5.3.1 Coupling Regime of the MMF

First, we employed a 206 cm long MMF in the reference arm with light coupled concentrically, which we refer to as central coupling regime. In the energy trace in Fig. 5.3.1(a), the leading random encoding function from the fastest MMF-guided mode appears as a dominant signal peak at the beginning of the energy trace. The energy trace decays sharply afterwards, indicating that the fastest lower-order guided modes carry most of the coupled optical energy. The sensing depth range was calculated as 6.4 mm. The SVD analysis of the calibrated REM, which visualizes the amplitude of the singular values, found only 297 populated modes, many fewer than the ∼790 available modes. This may be due to the fact that most light is coupled into lower-order modes in the launch condition. We then compared the sensitivity matrices obtained with the Hermitian transpose and Tikhonov-regularized reconstruction, respectively, and averaged the SNR within the first 6 mm of the available depth range. While the Hermitian transpose led to a rapid signal roll-off of −4.5 dB/mm and a low averaged SNR of 18.9 dB, Tikhonov-inversion offered a milder signal roll-off, −1.9 dB/mm, and a better averaged SNR of 26.0 dB. This suggests that the calibrated REMs are not even approximately unitary and numerically compensating for part of the experienced loss improves the reconstruction. We only used Tikhonov inversion for reconstruction of depth profiles and computation of the sensitivity matrix hereafter.

In the central coupling regime, the sensing depth range was confined due to the limited number of populated modes. To promote the population of higher-order modes, we coupled light into the MMF through two layers of Scotch tape, added into the fiber connector, to weakly scatter the transmitted light and excite higher-order modes. We termed this launch condition speckle coupling regime. Although this, indeed, resulted in increased coupling to higher-order modes, the resulting energy trace was very uneven. To homogenize the energy distribution between the guided modes, we further induced mode mixing along the MMF with a fiber mode scrambler (FM-1, Newport). While mode scrambling with the central coupling regime offered better energy distribution than without scrambling, we

found the combination of both speckle coupling regime and scrambling to be the most efficient for obtaining a smooth energy distribution. As shown in Fig. 5.3.1(b), with the speckle coupling regime and mode mixing, the energy was more uniformly distributed among the available random encoding functions, thereby extending the sensing depth range to 11.1 mm. SVD analysis revealed 468 populated modes. Furthermore, we found a signal roll-off of only −0.6 dB/mm within the first 6 mm depth range, much smaller than that in the central coupling regime. Inspecting the sensitivity matrix, the averaged SNR was slightly improved to 26.9 dB. In the following experiments, we used the speckle coupling regime and applied mode scrambling to optimize the sensing depth range and SNR.

5.3.2 Bandwidth-limited Axial Resolution

The resolving power to differentiate axially offset reflections depends on how fast the encoding functions decorrelate as a function of depth. We computed the function correlation matrix (FCM) as the normalized correlation between the encoding functions, E, at individual axial positions z_1 and z_2 as

$$C(z_1, z_2) \equiv \frac{\int E(k_{x,y}, z_1) \cdot E^*(k_{x,y}, z_2) dk_{x,y}}{\sqrt{\int |E(k_{x,y}, z_1)|^2 dk_{x,y}} \cdot \sqrt{\int |E(k_{x,y}, z_2)|^2 dk_{x,y}}}, \tag{5.3}$$

where the superscript * indicates complex conjugation. We measured random encoding functions at a sampling step size of 1 µm over a 200 µm axial range both for a 206 cm and 54 cm long MMF in the reference arm and calculated the resulting correlations. Because of phase drift in the interferometer, there exist random phase offsets between the various measured encoding functions. However, owing to the close correlation in these densely sampled encoding functions, it is straightforward to estimate and correct for the phase offsets.

By analyzing correlation traces $C(z_1, \Delta z)$ of the FCM in terms of the axial offset $\Delta z = z_1 - z_2$ we can assess the system resolving power. Figure 5.3.2 shows the average real part of correlation traces across the evaluated axial range, exhibiting FWHMs of 19 µm and 16 µm, respectively, for (a) 206 cm and (b) 54 cm long MMF. The obtained

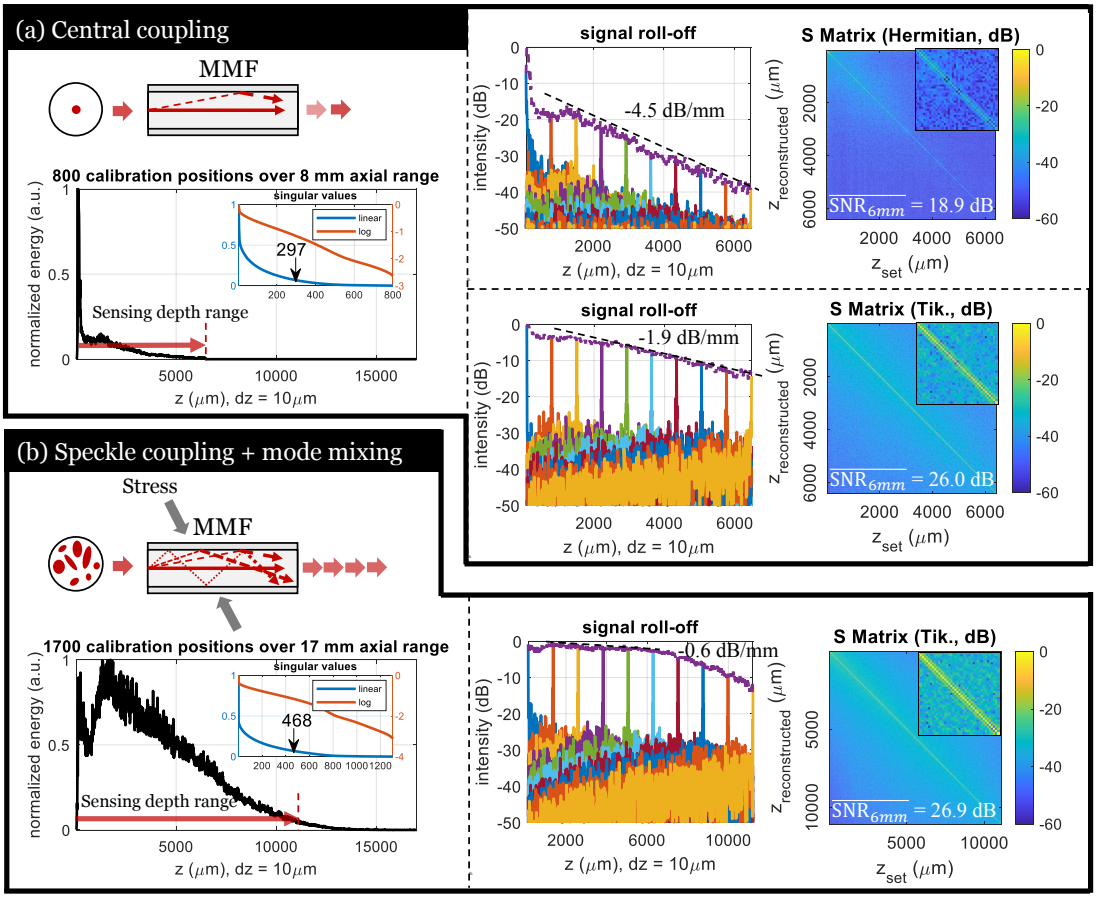

Figure 5.3.1: Analysis of system performance under different operating regimes. (a) Under the central coupling regime, a limited number of guided modes is populated, as also revealed by the singular values of the measured REM (inset). If we use 7% as a cutoff value in the SVD, there are 297 guided modes populated. The sensing depth range is 6.4 mm. The Tikhonov inversion outperforms the Hermitian inversion by improving the averaged SNR over the first 6 mm from 18.9 dB to 26.0 dB. (b) Under the speckle coupling regime and mode mixing, 468 modes are populated according to the SVD analysis. Also, the energy distribution among the random encoding functions is more uniform compared to that in the central coupling regime, leading to a sensing depth range of 11.1 mm . The signal level decays at a much slower rate. Finally, the averaged SNR over the first 6 mm is 26.9 dB. The inset of sensitivity matrix (S Matrix) shows a magnified central section. The sampling step size in both cases was 10 µm.

correlation traces exhibit a slight variation as a function of depth z_1, more so for the longer MMF. Nevertheless, they remain remarkably constant and can be approximated as the autocorrelation of the axial PSF of the profiling system, given by the Fourier transformation

of the source spectrum, i.e, its axial coherence function. The autocorrelation of the coherence function indeed closely matches the central peak of the experimental FCM, suggesting that the axial resolution is bandwidth-limited. Considering the close-to-Gaussian shape of the employed spectrum, the FWHM of the correlation peak is $\sqrt{2}$ times the width of the underlying PSF and we estimated the axial resolution to be 13.4 µm and 11.3 µm for the 206 cm and 54 cm long MMF, respectively. In contrast to the coherence function, the real part of the experimental correlation traces feature quite prominent side-lobes, which are of negative sign, as disclosed in the phase maps shown in Fig. 5.3.2. This may be attributed to spectral distortion in either arm of the interferometer that impacts the originally close to ideal shape of the spectrum.

5.3.3 Scalable Sensing Depth Range

The available DOFs are determined by the number of populated modes, which can be controlled by tailoring the input coupling regime and mode-mixing process. Meanwhile, the axial resolution is determined by the decorrelation distance between random encoding functions, which corresponds to the temporal coherence length of the source. Dividing the sensing depth range by the decorrelation distance provides the number of resolvable depth positions. To investigate the relation between the number of DOFs and resolvable depth positions in more detail, we conducted experiments with a 54 cm MMF and a 152 cm MMF, concatenated to the 54 cm fiber. In the first experiment, the 54 cm MMF was used alone, while in the second experiment, the 54 cm MMF was concatenated with the 152 cm MMF through a conventional FC/PC fiber connector (ADAFCB1, Thorlabs), resulting in a total MMF length of 206 cm. To populate a multitude of guided modes and homogenize the energy distribution among random encoding functions, we employed the speckle coupling regime and induced mode mixing with the fiber mode scrambler in the common 54 cm MMF in both experiments. The additional 152 cm MMF in the second experiment was loosely looped and placed on the optical table to avoid additional strong modal interactions

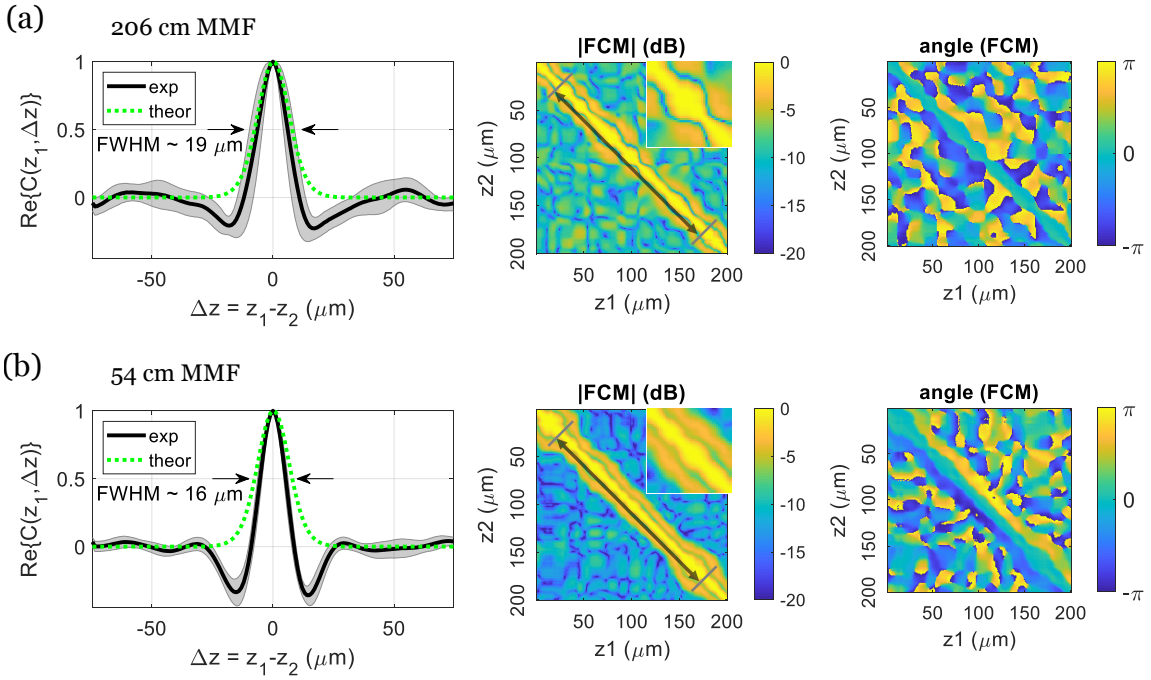

Figure 5.3.2: Experimental demonstration of bandwidth-limited axial resolution. Correlations between the random encoding functions obtained with a (a) 206 cm and (b) 54 cm long MMF. Each column of the FCM corresponds to a correlation trace at depth z_1 and, hence, the auto-correlation of the axial PSF. The $\mathfrak{Re}\{\cdot\}$ means the average real part of arguments, and the black curves are the aligned correlation traces averaged over the evaluated axial range indicated by the black double-sided arrows, and the shaded area indicates the standard deviation. The green curves are the theoretical correlation traces generated by Fourier transforming the elemental-wise square of the source spectrum. The inset shows the magnified central area of the FCM. The sampling step size in both cases was 1 µm.

and energy exchange during light propagation. As shown in Fig. 5.3.3, the 54 cm and 206 cm MMF offered 3.25 mm and 13.4 mm sensing depth range, respectively, corresponding to 288 and 1000 resolvable depth positions. In contrast, SVD analysis of the calibrated REMs indicated 346 and 660 DOFs, respectively. The average SNR over the first 3 mm in the sensitivity matrix is 45.6 dB for the 54 cm MMF, much higher than the 27.1 dB for the 206 cm MMF. This suggests a trade-off between sensing depth range and average SNR. Furthermore, inspecting the constructed FCMs, we find that the 206 cm MMF resulted

in a higher residual correlation, 0.0792, defined as the averaged correlation of off-diagonal elements within 2 to 30 coherence lengths away from the diagonal of the FCM. A higher residual correlation indicates more off-target signals that contribute to the background signal, which compromises the SNR. Consequently, increasing the number of resolvable depth positions beyond the number of available degrees of freedom comes at the expense of reducing system sensitivity. The experimental results are summarized in Table 5.1.

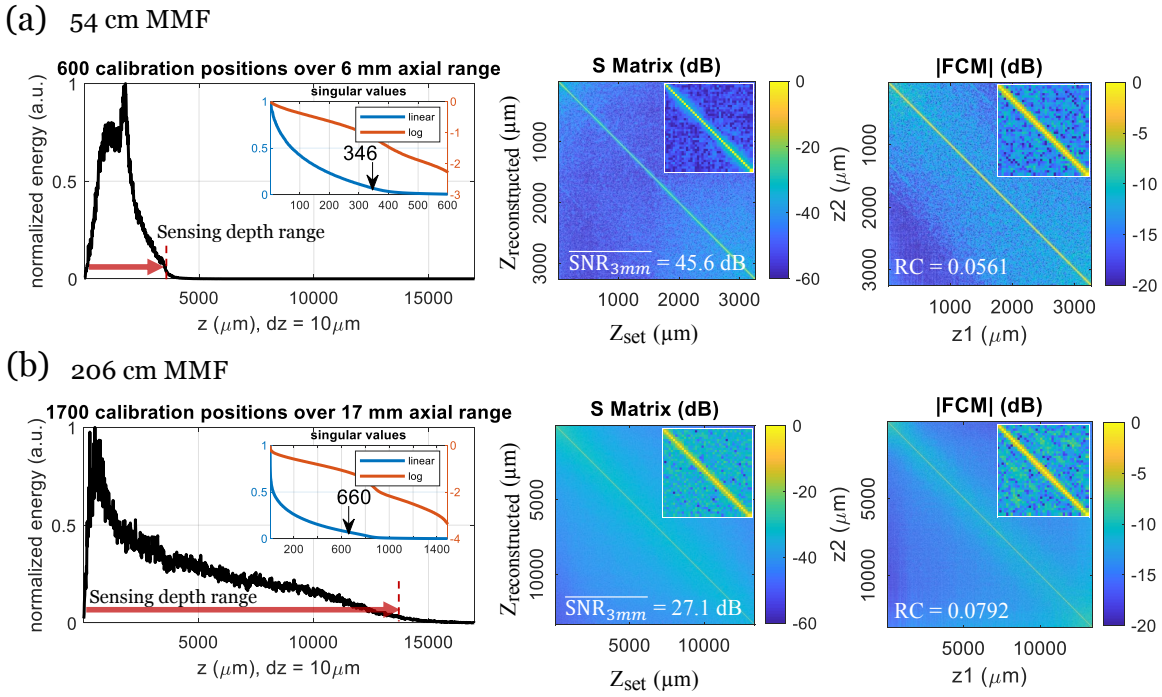

Figure 5.3.3: Comparison of the sensing depth range, system SNR, and residual correlation between a (a) 54 cm and (b) 206 cm long MMF. (a) The 54 cm MMF had a limited sensing depth range of 3.25 mm. In the constructed sensitivity matrix, an increased noise floor in axial locations with low energy coupling is noticeable. (b) 206 cm MMF length leads to an extended sensing depth range of 13.4 mm yet a lower averaged SNR. Comparing the FCMs of the 206 cm MMF to that of the 54 cm MMF, besides a higher residual correlation, correlation at large axial offsets is also stronger. The sampling step size in both cases was 10 μm.

Table 5.1: Trade-off between sensing depth range and SNR

	$L = 54$ cm	$L = 206 (= 54 + 152)$ cm
Sensing depth range	3.25 mm	13.4 mm
Number of resolvable depth positions	288	1000
Degrees of freedom	346	660
Signal-to-noise ratio (SNR)[a]	45.6 dB	27.1 dB
Residual correlation	0.0561	0.0792

[a] SNR of a mirror, attenuated by 32.7 dB.

5.4 Depth Profiling with a Random Encoding Matrix

Finally, we demonstrate 1D depth profiling and 2D cross-sectional imaging of custom-made phantoms placed in the sample arm. The samples consisted of stacks of glass slides, spaced by air gaps of different thickness. To optimize the efficiency of sample light collection, the specular reflections from sample interfaces were aligned with the illumination. We chose to fabricate these samples for profiling tests because the true physical locations of air-glass reflective interfaces were readily measurable as the ground truth for performance verification. Also, the air-glass interfaces acted as perfect Dirac delta functions for testing the system axial resolution.

For 1D depth profiling, the 206 cm MMF was used. The testing sample was a stack of two glass slides separated by a coverslip-thick air gap and with an overall physical thickness of about 2.3 mm, as shown in Fig. 5.4.1(a). Each single camera snapshot can be reconstructed into an entire depth profile, where the signal intensity indicates the sample reflectivity. As shown in Fig. 5.4.1(b), four clear signal peaks precisely mark the air-glass interface locations, as could be validated from the sample design. Furthermore, the FWHM of the signal peaks just slightly exceeds the sampling step size, 12 µm, consistent with the bandwidth-limited axial resolution.

To visually compare the imaging performance between use of short and long MMFs with their corresponding sensing depth ranges, we conducted cross-sectional 2D imaging of a

1D-structured sample with either the 54 cm or 206 cm MMF. In the experiment, an objective lens (LSM02, Thorlabs) for light focusing was inserted into the sample arm and in front of the sample, which comprised four glass slides separated by air gaps of different thickness and had an overall physical thickness of about 11 mm. A dispersion compensator (LSM02DC, Thorlabs) was inserted into the reference arm before the gold-coated mirror to compensate the chromatic dispersion introduced by the objective lens. The sample was translated in the lateral direction by a stepping stage (SGSP20-20, Sigma-Koki), and a camera snapshot to construct the corresponding depth profile was acquired at each lateral location. The sample and the scan range remained identical when switching between the two MMF lengths. As shown in Fig. 5.4.1(c), although the 54 cm MMF offered a limited depth range unable to cover the entire sample thickness, it provides superior SNR in the first 3 mm compared to the 206 cm MMF. On the other hand, despite the inferior SNR, the 206 cm MMF provided almost three-fold additional sensing depth range, enabling full-depth profiling of the sample.

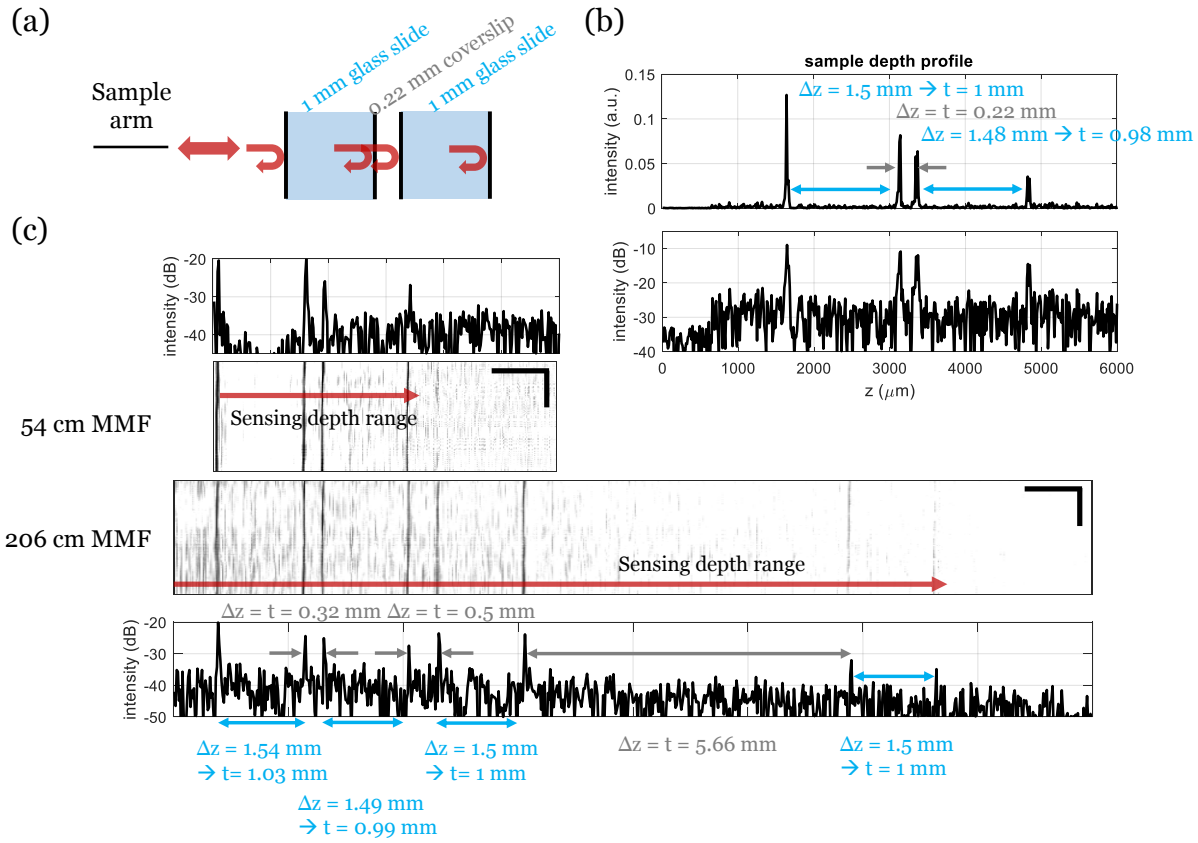

Figure 5.4.1: Examples of sample depth profiling. (a) Schematic of the multi-layer sample. (b) The reconstructed depth profile shows four reflectivity peaks corresponding to the air-glass interfaces. The spacings between the peaks are consistent with the physical thickness of the glass slides and the coverslip when assuming a refractive index of glass of 1.5. The sampling step size was 12 µm. (c) Cross-sectional image of another sample acquired with either the 54 cm or the 206 cm MMF. For each case, a selected depth profile is plotted in log scale to show the relative intensity of sample reflectivity. Reflectivity peaks are consistent with physical locations of air-glass interfaces of the sample. Using the 206 cm MMF allows full-depth imaging of the sample yet suffers from inferior SNR compared to using the 54 cm MMF. The sampling step size in lateral and axial directions was 10 and 20 µm, respectively, and the scale bars are 1 mm.

5.5 Discussion

We presented a depth profiling system with micron-resolution and centimeter-long depth sensing range by performing computational coherence gating with random encoding

functions generated from modal interference in a MMF. The ability to easily control the spatio-temporal coupling within the MMF affords a remarkable flexibility in adjusting the axial sensing range.

In theory, the physically available sensing depth range depends on the difference in the group delay between the fastest and the slowest guided mode. Based on geometric optics, with the fastest guided mode propagating parallel to the cylindrical axis and the slowest one zigzagging down the length of MMF at the critical angle $\theta_c = sin^{-1}(n_2/n_1)$, where n_1 and $n_2 = n_1 - \Delta n$ are the refractive indices of the fiber core and the cladding, we can estimate the maximal sensing depth range available with a given length of MMF L by their relative delay:

$$\Delta z_{\max} \sim (n_2/n_1) \times \Delta n \times L. \tag{5.4}$$

With 206 cm or 54 cm long step-index MMF, the maximal sensing depth ranges are 35 mm and 9.2 mm, respectively.

In our experiments, we first demonstrated that the sensing depth range and averaged SNR improve with the number of populated modes. While the speckle coupling regime and mode mixing help to populate higher-order modes, Tikhonov-inversion numerically corrects for unequal energy distribution among the random encoding functions. The Hermitian transpose is not an ideal reconstruction technique since the system is lossy and not unitary. Even with Tikhonov inversion, the achieved sensing depth range, 11.1 mm, is well below the theoretical lossless approximation of 35 mm for the 206 cm MMF. Several reasons can explain the restricted sensing depth range: The speckle input in the speckle coupling regime was not optimized to populate all guided modes (468 experimentally populated modes vs. 790 theoretically available modes). Mode mixing in the strong mode coupling regime, where light is coupled between guided modes of very different propagation constants, causes large path lengths to be averaged with shorter ones, thereby leading to a reduced sensing depth range [46]. Also, higher-order guided modes are more likely to experience propagation loss upon fiber deformation and scrambling, and coupling energy to random encoding functions

at large pathlength offsets is challenging. Finally, the detection of a single polarization state likely leads to additional loss. Engineering the input wave front coupling into the MMF and employing full polarization detection may offer more uniform energy distribution.

The number of resolvable depth positions can be calculated as the sensing depth range divided by the decorrelation distance. Based on Eq. 5.4 and the source coherence length, the number of the maximal resolvable depth positions with 206 cm MMF is 3097, which is significantly larger than the total number of available guided modes, ∼790 in a single polarization state. Since the delay of the random encoding functions is not continuous due to the discrete distribution of the propagation constants of the MMF's guided modes, it is conceivable that this would fragment the sensing range. However, we did not observe any discontinuity within the experimental energy trace or sensitivity matrix. This may suggest that sufficient mode mixing is taking place to maintain a continuous sensing range. Notwithstanding, our experiments revealed a trade-off between sensing depth range and sensitivity. When the number of resolvable depth positions exceeds the number of the REM's singular values with appreciable amplitude, the signal reconstruction becomes ill-conditioned and more sensitive to noise, as shown in Table 1. To operate the system in a well-conditioned regime, where its REM is highly invertible and the sensing depth range is maximized to use all degrees of freedom, the number of resolvable depth positions should match the degrees of freedom. Therefore, considering a MMF with all available modes equally populated, the optimal sensing depth range, Δz_{opt}, can be determined by the number of total available guided modes of a MMF, N_{mode}, and the source coherence length, l_{coh},

$$\Delta z_{\text{opt}} = N_{\text{mode}} \times l_{\text{coh}}. \tag{5.5}$$

Specifically, for the depth profiling system operating with the $\Phi = 105$ µm, 0.22 NA MMF, the number of total available modes in a single polarization state is 790, and the optimal sensing depth range is 10.3 mm, which corresponds to 61 cm MMF according to Eq. 5.5, assuming all available modes are equally populated.

Our imaging strategy using random encoding functions generated by a MMF does not rely on sample sparsity. Although the properties of the generated encoding functions would likely be suitable for subsampling of sparse signals, the set of encoding functions spans the entire depth range, allowing direct inversion and, hence, reconstruction of the full depth information. However, digital post-processing for distortion compensation, aberration cancellation, or noise suppression to improve measurement performance would be possible through refined inversion strategies and inclusion of regularization in the image reconstruction. Using the random encoding functions obtained from complex media for computational imaging can circumvent physical constraints encountered by conventional imaging systems and facilitate the development of novel measurement architectures leading to smaller, faster, or cheaper devices. For instance, in a grating-based spectrometer for spectral-domain optical coherence tomography (SD-OCT), a large sensing range demands a diffraction grating with high spectral resolution, and the number of resolvable positions is linearly proportional to the dimension of the utilized line scan camera. A typical SD-OCT with millimeter sensing range and micron-scale axial resolution already employs line scan cameras with thousands of pixels. The specifications to enable centimeter imaging range with SD-OCT comparable to our depth-profiling system would be difficult to meet with commercially available line scan cameras. Previously, linear OCT has been proposed as a path to cheaper and simplified coherence gating by using spatial multiplexing. However, to achieve centimeter-long imaging range, it would still require a similar unpractically long linear image sensor or a sophisticated free-space interferometer [117, 118]. While the initial implementation of our system used carefully designed achromatic off-axis holography, we verified experimentally that similar results can be obtained by simply tilting the MMF reference fiber, equivalent to replacing the reflective grating with an angled mirror. This suggests that even lens-less off-axis interference between the light from the single mode fiber and the MMF should result in comparable random encoding functions, offering a striking simplification of the system design. Indeed, the achromatic interference pattern is

only needed when attempting to demodulate the broadband interference term into spatial camera coordinates. This is unnecessary for our sensing matrix which is constructed in the in-plane momentum domain, although extended bandwidth will radially blur the interference term and increase the number of elements in each column of the REM, eventually affecting the reconstruction stability.

5.6 Conclusion

In this chapter, we introduced a depth profiling system that performs computational coherence gating by employing a set of random encoding functions generated from a MMF. The reflectivity at each axial position within a sample is encoded by interference with the corresponding random encoding function. With a calibrated REM, 1D reflectivity depth profiles of a sample can be non-adaptively reconstructed from a single camera snapshot without mechanical or optical scanning. Tailoring the physical length and coupling regime of the MMF, we demonstrated a scalable sensing depth range from 3.25 to 13.4 mm, while achieving high axial resolution of 13.4 µm.

I am very seldom interested in applications. I am more interested in the elegance of a problem. Is it a good problem, an interesting problem?

— Claude Shannon

6

Proximal Calibration Method towards Flexible MMF Endoscopy

Contents

Optical multimode fiber (MMF) may serve as narrow-gauge imaging probes that extend the reach of optical endoscopy based on computational reconstruction considering the fiber transmission. However, calibrating the fiber in an endoscopic setting is exceedingly challenging, limiting the flexibility of probes and wide-spread applications. Here, we demonstrate a

solution by recovering the fiber transmission from proximal measurements using optimization techniques and insights from waveguide physics. Final manuscript in preparation.

6.1 Reciprocal Symmetry and Solution Ambiguity

The implementation of a flexible MMF endoscope remains technically challenging despite recently proposed strategies [22, 37, 39, 78, 119–121] and the lack of flexibility is the enduring bottleneck for MMF imaging applications. Because the transmission through MMF is notoriously sensitive to physical fiber deformation, a flexible MMF endoscope would demand repeated on-site calibration without open distal access in practical endoscopic settings. Imaging through MMF with certain flexibility based on data-driven approaches has been reported, yet relying on a transmissive regime that requires open distal access [120, 121]. Although calibrating MMF with only proximal access is a desirable strategy, robust experimental MMF proximal calibration methods remain to be demonstrated. Understanding the reciprocal nature of light propagation through a MMF and the underlying symmetry constraints may help tackle this challenge. In the context of proximal MMF calibration, where the measurement of $\mathbf{T}_{2X}$ may be available, the demonstrated reciprocal symmetry in Section 2.4 precludes straightforward recovery of $\mathbf{T}_{fw}$ or $\mathbf{T}_{bw}$, which is needed for imaging through the MMF [20, 22, 29, 34]. To appreciate this limitation, we can factor $\mathbf{T}_{fw}$ into its symmetric and anti-symmetric parts based on the second polar decomposition [122],

$$\mathbf{T}_{fw} = \mathbf{AL}, \tag{6.1}$$

where $\mathbf{A}$ is orthogonal ($\mathbf{A}^T = \mathbf{A}^{-1}$) and $\mathbf{L}$ is transpose symmetric ($\mathbf{L}^T = \mathbf{L}$). In this case, Eq. 2.9 becomes

$$\mathbf{T}_{2X} = \mathbf{L}^2. \tag{6.2}$$

The orthogonal parts cancel each other upon forward and backward transmission, preserving only the symmetric part in the round-trip transmission measurement. Equation 6.2 states

a fundamental restriction: while the symmetric part of $\mathbf{T}_{\text{fw}}$ can be uniquely retrieved by taking the matrix square-root of the proximally measured $\mathbf{T}_{\text{2X}}$ [123] (if it has no negative real eigenvalues), the orthogonal part, $\mathbf{A}$, vanishes due to the intrinsic propagation property imposed by the optical reciprocity. Put differently, although a square, complex-valued matrix of dimension M has $2M^2$ unknown coefficients, the transpose symmetry reduces this number to $M^2 + M$, masking the additional $M^2 - M$ of the orthogonal component. This leads to the symmetric degeneracy of $\mathbf{T}_{\text{fw}}$ even though $\mathbf{T}_{\text{2X}}$ is known. This explains why $\mathbf{T}_{\text{fw}}$ cannot be directly retrieved from $\mathbf{T}_{\text{2X}}$, which complicates strategies for MMF proximal calibration.

6.2 Physics-informed Proximal Calibration Method

6.2.1 Distal Calibration Elements and Triplet Measurements

To eliminate the degeneracies, we propose a proximal calibration method, as illustrated in Fig. 6.2.1(a): A calibration element at the MMF distal end that is capable of at least three different realizations, where the round-trip TM, $\mathbf{C}_{i=1,2,3}$, of each element realization has sortable eigenvalues and distinctive eigenvectors [124]. We then measure from the MMF proximal end a triplet of round-trip TMs, $\mathbf{M}_{i=1,2,3}$, with the corresponding distal calibration element realizations. The light forward propagation through the MMF, followed by the distal element and reflection, and backward propagation along the reciprocal path can be modeled as TM multiplications,

$$\mathbf{M}_i = \mathbf{T}_{\text{fw}}^{\text{T}} \mathbf{C}_i \mathbf{T}_{\text{fw}}, \ i = 1, 2, 3. \tag{6.3}$$

Together with the prior knowledge of the distal calibration element, we previously showed with numerical evidence that the single-pass TM of the MMF in an arbitrary physical conformation could be retrieved analytically [124]. Nevertheless, a real-world MMF is lossy, where its TM is low-rank, creating an ill-posed problem subject to measurement noise. The method or other analytical approaches [37], which attempt exact matrix inversion

or factorization, are therefore not feasible in a realistic condition. As a result, we need modifications to the numerical algorithm.

We alternatively resort to an adaptive method by minimizing a cost function, which is the difference between the measurements and analytical model and searching for a complex $\mathbf{T}_{\text{fw}}$ matrix,

$$\overline{\mathbf{T}}_{\text{fw}} = \arg\min_{\mathbf{T}_{\text{fw}}} \sum_{i=1}^{3} || \mathbf{M}_i - \mathbf{T}_{\text{fw}}^{\text{T}} \mathbf{C}_i \mathbf{T}_{\text{fw}} ||_F^2, \tag{6.4}$$

where the overline indicates optimal value, and F is the Frobenius norm. This is similar to the simulation work by Gordon et al. [39], where multiple color filters and passive metasurface reflectors were designed as distal calibration elements, and operations at three wavelengths served as three different realizations. The advantage of our configuration here is that the requirement of distal calibration element is much relaxed, and no complicated design is needed. Unfortunately, directly optimizing the problem without a good initial estimate generally results in false solutions corresponding to local minimums, which, empirically speaking, are far away from the true solution. Therefore, we investigate additional constraints that can be integrated to the problem to avoid false solutions. For simplicity, we drop the subscript of $\mathbf{T}_{\text{fw}}$ and use $\mathbf{T}$ to specify the forward TM from here on.

6.2.2 Optimization with Waveguide-physics-based Constraint

According to waveguide theory, an ideal and straight MMF has a set of N guided propagation invariant modes (PIMs) with different propagation constants, and each PIM is an eigenvector of the MMF TM and does not interact with others. Under a general condition of mild fiber bending and looping, most modal interactions between PIMs are those with similar propagation constants due to momentum conservation, and this is often termed as weak coupling regime (scattering mean free path $<$ fiber length). As a result, while a practical MMF is considered as a complex media with chaotic transmission, there are underlying physical constraints structuring the TM, which can be revealed when the TM

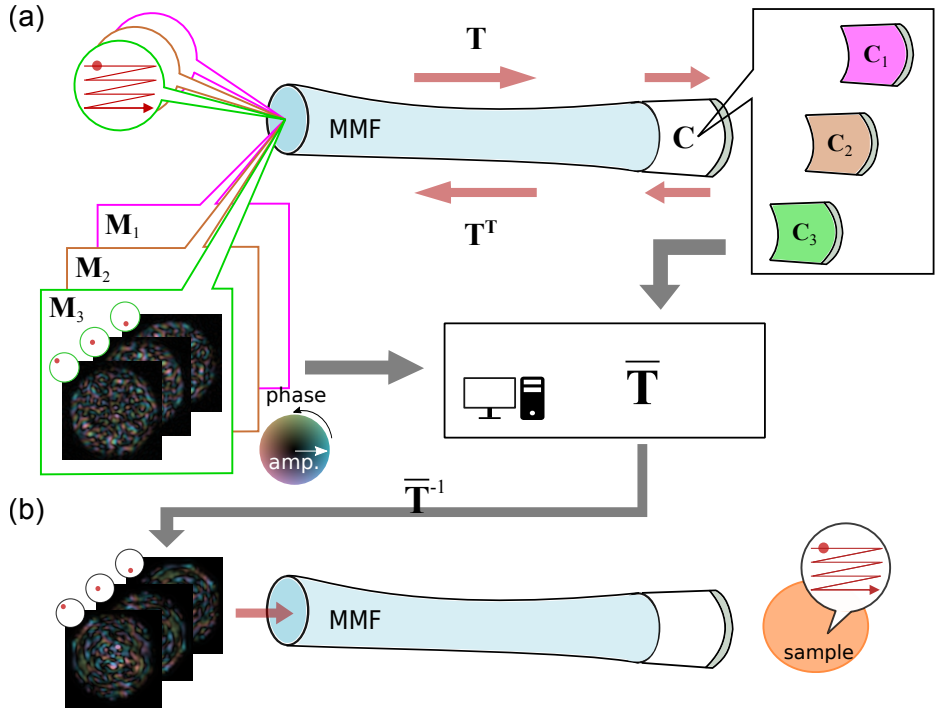

Figure 6.2.1: Overview of the proposed proximal calibration method. (a) Using a distal calibration element **C** and the knowledge of transmission sparsity, we retrieved the MMF forward transmission **T** from proximal measurements **M** based on optimization. The color maps encode complex values. (b) The reconstructed MMF transmission allows focusing and imaging through the fiber.

is in the PIM representation. Incorporating the constraints into Eq. 6.4 may help to avert false solutions. This is similar to compressive sensing and regularization strategies, where the signal sparsity facilitates reconstruction in underdetermined linear systems [125, 126].

To represent TMs in PIM basis as illustrated in Fig. 3.1.1(a), we numerically generated a set of theoretical PIMs based on the MMF specifications, grouped the vectorized PIMs into **E** in a descending propagation constants order, and projected **T**, $\mathbf{M}_i$, and $\mathbf{C}_i$ from the original recording coordinates to the modal space

$$\begin{aligned} \mathbf{X} &= \mathbf{E}_d^{\dagger}\mathbf{T}\mathbf{E}_p \\ \mathbf{P}_i &= \mathbf{E}_p^{\mathrm{T}}\mathbf{M}_i\mathbf{E}_p \\ \mathbf{D}_i &= \mathbf{E}_d^{\mathrm{T}}\mathbf{C}_i\mathbf{E}_d, \end{aligned} \tag{6.5}$$

where we used subscripts p and d to denote PIMs on the proximal and distal ends, $\mathbf{E}_p$ and $\mathbf{E}_d$, respectively. Due to the projection, $\mathbf{X}$, $\mathbf{P}_i$ and $\mathbf{D}_i$ are square matrices. Numerical corrections are necessary to compensate physical misalignment (see Section 2.2.4). In the modal space under the weak coupling regime, $\mathbf{X}$ has diagonal-ish structure. To leverage the waveguide structure in the optimization problem, we designed and generated a real-valued and elemental-wise regulator $\mathbf{S}$ that penalizes the off-diagonal elements, which represent the less likely coupling between modes of much different propagation constants. Strictly speaking, we are not performing basis transformation on the round-trip TMs, $\mathbf{P}$ and $\mathbf{D}$, as the complex $\mathbf{E}_p$ matrix is unitary but not orthogonal, and this is to preserve the transpose symmetry of the round-trip TMs in the projected modal space. Plugging the changes into the original optimization problem including the regulator, we have a modified cost function

$$\overline{\mathbf{X}} = \arg\min_{\mathbf{X}} \sum_{i=1}^{3} || \mathbf{P}_i - \mathbf{X}^{\mathrm{T}} \mathbf{D}_i \mathbf{X} ||_F^2 + \lambda || \mathbf{S} \odot \mathbf{X} ||_F^2, \tag{6.6}$$

where $\overline{\mathbf{X}}$ is the speculated $\overline{\mathbf{T}}$ in the PIM basis, the $\odot$ symbol indicates Hadamard product, and λ is the parameter controlling the importance of the regularization term. To achieve efficient calculation of Eq. 6.6, we developed an analytical gradient for steepest descent. We then optimized the three sub-problems sequentially and iteratively to avoid local minimum since the degeneracies in each sub-problem are not typically the same. With reconstructed $\overline{\mathbf{X}}$, we recovered the single-pass $\overline{\mathbf{T}}$ by reversing the basis transformation from the modal space back to the recording coordinates with the previously calculated transformation matrices, $\mathbf{E}_{d,p}$,

$$\overline{\mathbf{T}} = \mathbf{E}_d \overline{\mathbf{X}} \mathbf{E}_p^{\dagger}. \tag{6.7}$$

The recovered $\overline{\mathbf{T}}$, which specifies the full light transfer information for all spatial channels, can thereafter allow coherent focusing or imaging techniques through the MMF with matrix inversion $\overline{\mathbf{T}}^{-1}$ [22, 86], as illustrated in Fig. 3.1.1(b).

6.2.3 Experimental Setup

To prove the concept of the proximal calibration method based on the numerical algorithm as in Eq. 6.6, we measured $\mathbf{T}$ and $\mathbf{C}$ and synthesized $\mathbf{M}$ in Eq. 6.5. The polarization-resolved TM measurement setup is shown in Fig. 6.2.2, which is the same as in Chapter 3 and 4 and publication [86]. We used a 1m-long step-index MMF (SI-MMF) with 50 µm core size, and 0.22 NA operated at 1550 nm, which theoretically supports ∼129 spatial modes per polarization state. The fiber was loosely coiled with a minimum radius of curvature of ~ 50 mm. We measured $\mathbf{T}$ by sequentially probing proximal input channels and detecting the corresponding distal output including both polarization states, as illustrated in Fig. 6.2.2(a). The input and output channels of $\mathbf{T}$ have been ordered first by spatial coordinate, then by polarization, leading to four quadrants corresponding to either H or V illumination and detection.

The same MMF was utilized as a distal calibration element with the glass-air interface at fiber distal facet providing reflection signals. In Fig. 6.2.2(b), to measure its round-trip TM, $\mathbf{C}$, we probed through the same set of input channels and detected the corresponding proximal outputs at the same input locations. Similar to $\mathbf{T}$, $\mathbf{C}$ also has four polarization quadrants. We separately obtained the round-trip TMs, $\mathbf{C}_{i=1,2,3}$, in three different fiber shape realizations, respectively. To retain the intrinsic transpose symmetry of $\mathbf{C}$ imposed by optical reciprocity, we numerically corrected the misalignment of output channels [41].

As illustrated in Fig. 6.2.2(c), we then modeled the concatenation of the distal calibration element to the original to-be-calibrated MMF segment with matrix multiplication, and synthesized proximal measurements, $\mathbf{M}_{i=1,2,3}$ following Eq. 6.3. In a practical endoscopic setting without open access to MMF distal end, we have prior knowledge of $\mathbf{C}$ and can measure $\mathbf{M}$. To approximate a real experiment, we added to $\mathbf{M}_i$ complex white Gaussian noise with a signal to noise ratio of 18, justified by noise quantification in repeated TM measurements.

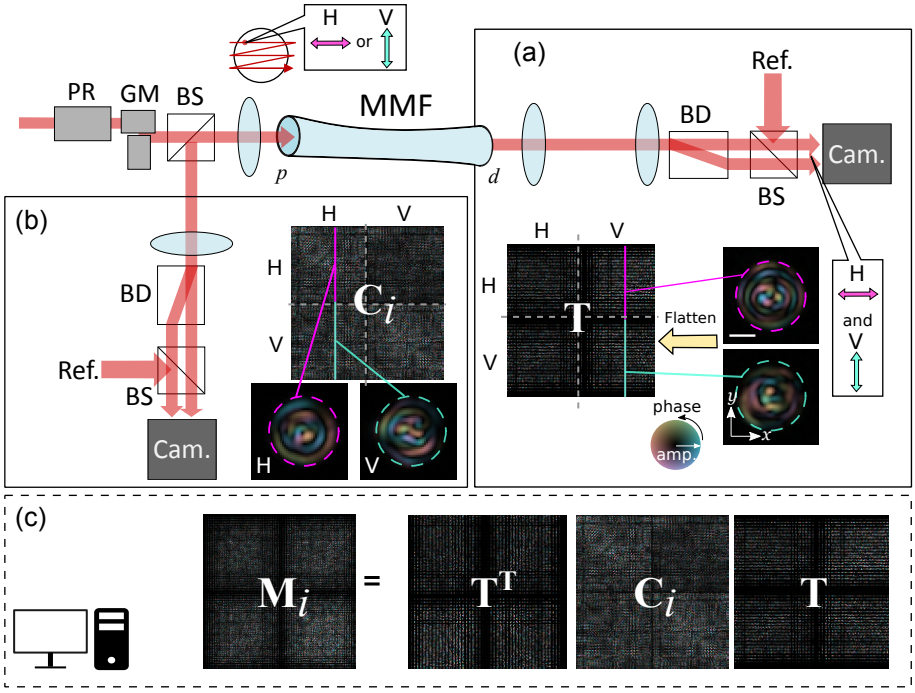

Figure 6.2.2: Experimental setup of MMF TM measurement. PR: phase retarder, GM: galvanometer scanning mirror, BD: beam displacer, BS: non-polarization beam splitter, Ref.:reference wave, Cam.: camera. Using (a) single-pass $\mathbf{T}$ measurement and (b) round-trip $\mathbf{C}_{i=1,2,3}$ measurements, we can (c) synthesize proximal $\mathbf{M}_{i=1,2,3}$ measurements imitating calibration signals in an endoscopic setting.

6.2.4 Regulator Generation

The regularizer $\mathbf{S}$ in Eq. 6.6 penalizes the matrix entries accounting for unlikely coupling in estimated $\mathbf{X}$ to impose the sparsity constraint. To design an adequate regularizer, we generated a generic real-valued mask $\mathbf{S}$ by fitting the sparsity model $\mathbf{S}_q$ on each polarization quadrant of empirical $\mathbf{X}$

$$\begin{aligned} \mathbf{S} &= \begin{bmatrix} \mathbf{S}_{\mathrm{HH}} & \mathbf{S}_{\mathrm{VH}} \\ \mathbf{S}_{\mathrm{HV}} & \mathbf{S}_{\mathrm{VV}} \end{bmatrix} \\ \mathbf{S}_q(\zeta,\xi) &= 1 - e^{-a(r/N)-((\theta-b)/c)^2} \\ r &= \sqrt{\zeta^2+\xi^2}, \theta = \tan^{-1}(\xi/\zeta) \\ \overline{\mathbf{S}}_q &= \arg\min_{\mathbf{S}_q} \left| 0.7 - \frac{||\mathbf{S}_q \odot \mathbf{X}_q||_F^2}{||\mathbf{X}_q||_F^2} \right|, \end{aligned} \tag{6.8}$$

where a, b, c are the parameters to be fitted, and ζ and ξ are the row and column indices, respectively. Figure 6.2.3(a) shows $\mathbf{X}$, the forward TM in PIM basis, where the energy concentrates towards the diagonal. Lower order modes have more localized cross-coupling. We generated sparsity mask $\mathbf{S}$ for optimization regularization, as shown in Fig. 6.2.3(b), where each quadrant has similar structure. We tested the mask on forward TM of MMF in several shape realizations, and all TMs have $70 \pm 4\%$ energy contained within the mask.

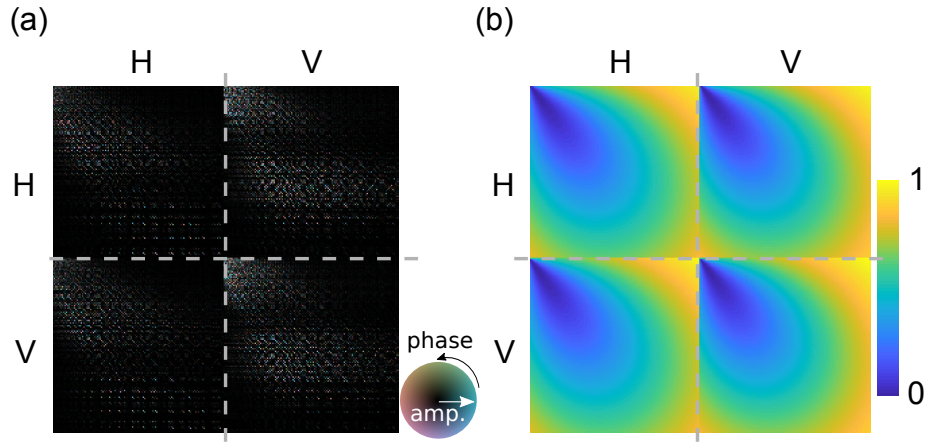

Figure 6.2.3: Sparsity of the transmission matrix in modal representation. (a) The forward $\mathbf{X}$ (b) Generated mask $\mathbf{S}$ based on TM.

6.3 Transmission Reconstruction Accuracy

6.3.1 Reconstructing Forward TM

With proximal measurement $\mathbf{P}$, prior knowledge of distal calibration element $\mathbf{D}$, and generic waveguide structure $\mathbf{S}$, we aim to retrieve $\overline{\mathbf{X}}$ for MMF imaging by solving the optimization in Eq. 6.6 with $\lambda = 0.04$. While minimizing the designed cost function, we monitored the normalized error of current estimated $\overline{\mathbf{X}}$ compared to ground truth $\mathbf{X}_{\text{gt}}$,

$$\epsilon(\overline{\mathbf{X}}, \mathbf{X}_{\text{gt}}) = \frac{||\overline{\mathbf{X}} - \mathbf{X}_{\text{gt}}||_F^2}{||\overline{\mathbf{X}}||_F ||\mathbf{X}_{\text{gt}}||_F}. \tag{6.9}$$

We also evaluated the matrix correlation by calculating

$$C(\overline{\mathbf{X}}, \mathbf{X}_{\mathrm{gt}}) = \left| \frac{\sum_{ij} a_{ij}^* b_{ij}}{\sqrt{\sum_{ij} |a_{ij}|^2} \sqrt{\sum_{ij} |b_{ij}|^2}} \right|, \tag{6.10}$$

where , i and j are the matrix row and column indices, and a_{ij} and b_{ij} are the entries of $\overline{\mathbf{X}}$ and $\mathbf{X}_{\mathrm{gt}}$, respectively. In addition, we synthesized focusing through MMF for visualizing reconstruction efficacy. To show the robustness of our method, which does not require the knowledge of fiber shape, we started from a random initial guess $\mathbf{X}_{\mathrm{init}}$, which is a complex normally distributed random matrix masked with $1 - \mathbf{S}$, and the corresponding focusing through MMF resulted in speckle output. As shown in Fig. 6.3.1, the initial cost, error, and matrix correlation are 0.69, 168.4%, and 0.02, respectively. The matrix product $\mathbf{X}_{\mathrm{gt}} \mathbf{X}_{\mathrm{init}}^{\dagger}$ is a chaotic matrix, indicating that the initial guess is far from the ground truth. The optimization algorithm converged within 12000 iterations in ∼20 min. The final cost, error, and matrix correlation are 0.51, 43.2%, and 0.78, respectively. Therefore, the optimization leads to a good solution regardless of a random initial guess.

6.3.2 Reconstruction Evaluation

To test the spatial uniformity of the reconstructed channels in real space, we converted $\overline{\mathbf{X}}$ back to $\overline{\mathbf{T}}$ in real space following Eq. 6.7, and numerically focused through individual channels. To synthesize focusing through the MMF, we separately measured another $\tilde{\mathbf{T}}$, where the $\sim$ symbol indicates replicate measurement. We then computed the input wave-fronts, which are essentially the columns of $\overline{\mathbf{T}}^{-1(\mathrm{tik})}$ using Tikhonov regularized matrix inversion since the TM is low-ranked and non-invertible. Numerically propagating the wave-fronts through the MMF, which is modeled by $\tilde{\mathbf{T}}\overline{\mathbf{T}}^{-1(\mathrm{tik})}$, creates foci at varying distal positions. Reshaping the distal output to 2D coordinates allow us to visualize focusing and evaluate the recovery of $\overline{\mathbf{T}}$, as few examples are shown in Fig. 6.3.2. The focus contrast at each channel, η, defined as the ratio of the peak intensity at the intended focal point to the average level of speckled background, is computed, and the averaged

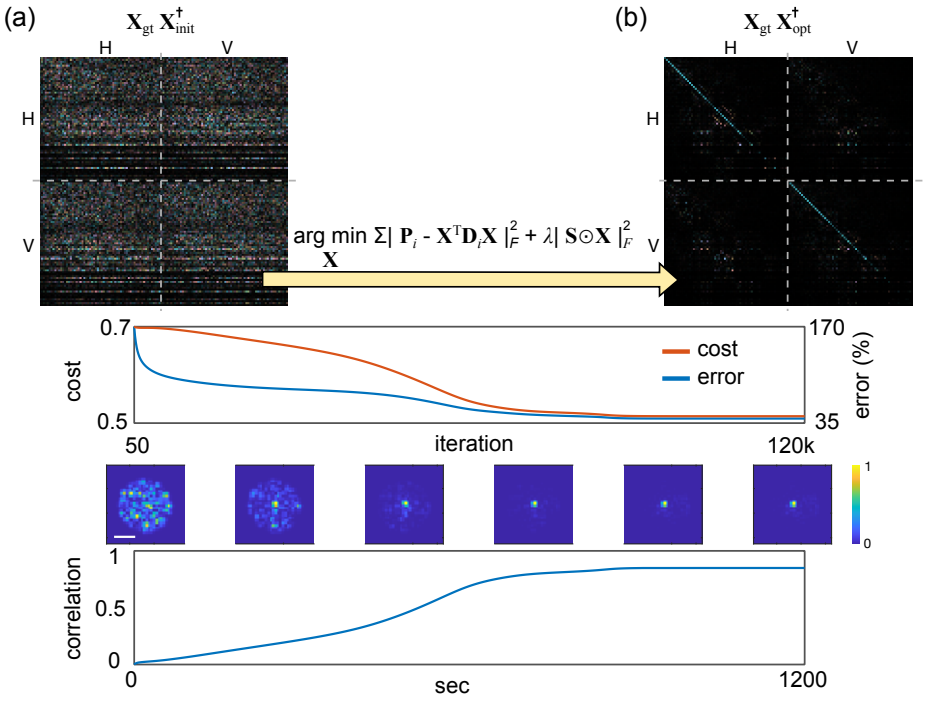

Figure 6.3.1: Forward transmission reconstruction by solving the designed optimization problem. $\mathbf{X}_{gt}\overline{\mathbf{X}}^{\dagger}$ (a) before (b) after the optimization.

value over all available channels is ∼100.7. For comparison, we repeated the process using the ground truth $\mathbf{T}$, where the averaged focus contrast is ∼187.5, as if the open distal access is available in common MMF calibration experiments.

In addition to focusing through MMF at individual channels, we simulated reflectance imaging through MMF to visualize performance. To image an object through the MMF, we mapped the generated scanning focus within the MMF core to reflectance intensity of the object at the corresponding position on a 2D grid, which is equivalent to common imaging through MMF experiments based on WFS systems [22, 72]. We then tiled multiple images as if the MMF is moving across the object to augment the FOV. The results are shown in Fig. 6.3.3.

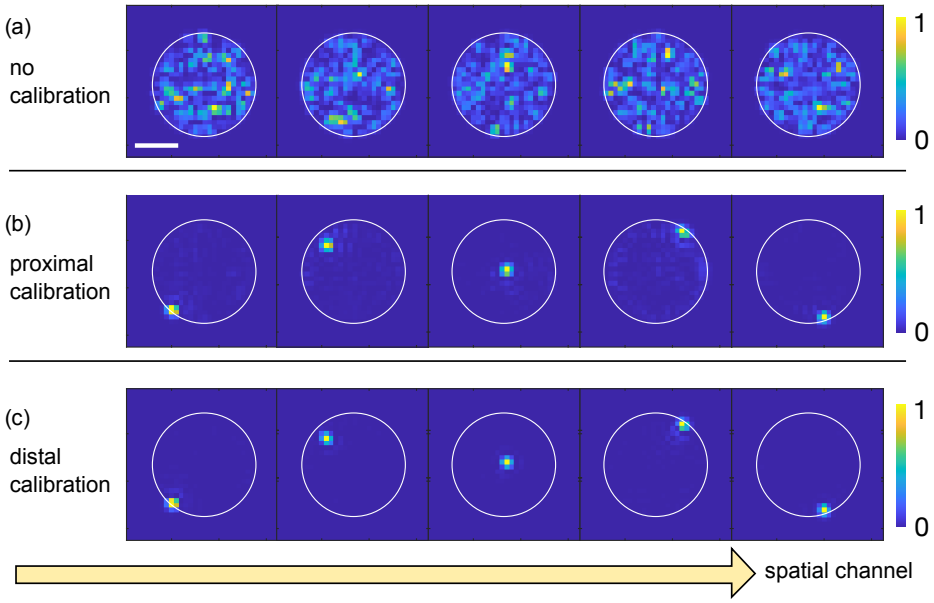

Figure 6.3.2: Focusing through MMF at various channels with (a) no calibration (b) our proximal calibration approach (c) common distal calibration.

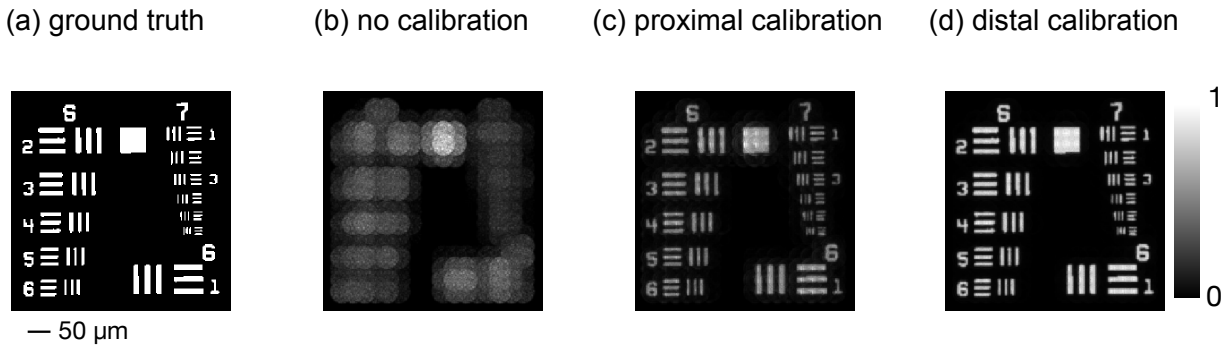

Figure 6.3.3: Simulated imaging through MMF of (a) object with (b) no calibration (c) our proximal calibration approach, and (d) common distal calibration.

6.4 Discussion

Calibration of MMF forward transmission without open distal access is inevitable in the development of flexible MMF endoscopy. However, the transpose symmetry of proximal measurements results in ambiguity when reconstructing the MMF forward transmission. By

leveraging the distal calibration element and sparsity constraint on the MMF transmission as analogous to compressed sensing [127], we crafted an optimization formulation that avoids convergence to false solutions in the under-determined system.

While bending admittedly remains the most fundamental limitation towards practical use of flexible MMF endoscopy, several strategies tackling the problem from different aspects are being pursued to address the need for TM calibration without open access to the distal fiber end: The transmission through MMF can be predicted given the fiber shape [22]; The installation of carefully designed passive distal optics to the MMF tip may provide additional mathematical constraints that in retrieving the TM from round-trip measurements [37, 39]; Graded-index MMF has been shown to feature increased robustness of light transport to bending deformations [38]; A distal guide star together with prior knowledge of TM structure can assist recovering a subset of spatial channels using only proximal access for partial imaging through a MMF [40]; Compressive sampling of TM has been reported to greatly reduce the number of measurements by assuming a TM sparsity constraint [79], which could also be used for TM deduction in proximal calibration; Alternatively, input to MMF with random fiber conformations can be reconstructed from output speckle patterns based on a data-driven approach [128]. Further progress with these methods in combination with our matrix approach would pave a way to flexible MMF endoscopy in a general clinical setting. The proposed iterative method is different from an analytical attempt, as it does not involve direct matrix inversion or factorization that may amplify the measurement noise and compromise the retrieval of a good solution. The optimization converges to a good solution regardless of random initial guess, allowing on-site MMF calibration. Since the triplet proximal measurements with different realizations of the distal calibration element render information of forward transmission spanning all available spatial channels, the reconstruction is not limited to certain physical position and hence partially calibrated MMF. Furthermore, the method does not require exact fiber shape and geometry, integrated optics with sophisticated nano-structure, and precise operating wavelengths,

and a common complex medium may suffice as a distal calibration element. In this study, we demonstrated the proximal calibration by synthesizing round-trip measurements from experimental experimental TMs, indicating the practicality and potential of implementation.

In the experiments, we used another MMF segment as the distal calibration element to show that our method works with readily available complex media. As a result, an optical diffuser that scrambles light propagation may also serve for the purpose and have a miniaturized footprint. However, in this case we need to consider the optical coupling efficiency, as high laser power for compensating loss may be dangerous, and the stray light reflection may lead to additional problems. Also, while we physically perturbed the calibrating MMF for different realizations, the design and engineering of the calibration element with actuators will be necessary for pragmatic development. One possible engineering solution is to use polymer-dispersed liquid crystals, where their optical properties can be configured by applied voltages [129]. Lastly, a remotely controllable optical filter for separating MMF calibration and imaging modes is also required to achieve a fully functional MMF-based endoscope.

In our designed optimization problem, the time complexity of computation grows with the power of number of modes, and the calibration of MMFs with larger core size and more number of modes may need huge computing power for on-the-fly calibration. Similar to many steepest gradient descent algorithm, an adaptive step size may help accelerating the convergence. Since the TM sparsity relies on a weak scattering regime, the efficiency of the proximal calibration method upon MMF bending with small radius of curvature remains to be investigated.

Remaining efforts towards achieving flexible MMF endoscopy are practical implementation of miniaturized distal calibration elements, high-speed TM measurements, and fast numerical recovery of forward transmission from proximal measurements, which may also spark new approaches for deep tissue imaging or remote sensing.

6.5 Conclusion

In this chapter, we learned how reciprocal symmetry in proximal measurements of MMF transmission imposes ambiguity on the retrieval of forward light transport process. Nevertheless, using the optimization approach with sparsity constraint according to waveguide physics, we can solve for the ill-posed inverse problem and reconstruct all MMF imaging channels. The demonstrated proximal calibration method may relax requirements on the design and fabrication of MMF and distal calibration elements, which may expedite the imaging probe development towards flexible MMF endoscopy.

Research is what I'm doing when I don't know what I'm doing.

— Wernher von Braun

7 Conclusion and Future Outlook

Contents

In the previous sections, we developed various simulation toolboxes and computational solutions to address critical technical challenges of imaging and sensing through MMF. Here, we summarize the chapters and highlight the main contributions of our works. Then, based on the achievements, we will discuss the future outlook of MMF-based endoscopy and pertinent applications. Finally, we will give conclusion of this thesis.

7.1 Summary and Contributions

In Chapter 2, we reviewed theoretical MMF transmission model, created numerical simulation toolbox, and studied the fiber-guided modes, propagation constants, and mode coupling effect under fiber bending. The different refractive index profiles between SI- and GI-MMF lead to distinctive transmission properties. We employed a coherent

transmission matrix (TM) technique to characterize the end-to-end light transport process between input and output channels, which allows us to quantify number of guided modes, study transmission loss, visualize hidden transmission structure and underlying physics, and enable focusing and imaging through MMF. We also developed several numerical techniques to handle matrix inversion, correct physical misalignment in experiments, and transform matrix basis.

In Chapter 3, we disclosed a computational imaging paradigm for multi-modal 3D reflectance imaging through MMF of unlabeled samples and without active wave control. Using the TM technique, we numerically created depth-gating effect for optical sectioning, refocused on varying axial position for 3D imaging, and extracted elastic signals with various sample specificity. We evaluated the optical sectioning, fully characterized the imaging system performance, and demonstrated numerical point spread function engineering. Compared to the previous imaging through MMF approaches, our method has advantages in image rendering flexibility, label-free contrast generation, hardware system simplicity, and potentially imaging speed. The method has also enabled many first-time imaging demonstration through MMF including phase and polarization-resolved imaging in a reflection geometry.

In Chapter 4, we demonstrated a computational spectral correlation in MMF, which brings new insights in spectral DOF of complex media. We created a parametric dispersion model that allows compensating waveguide dispersion in fiber transmission, revealing an ultra-wide hidden spectral correlation. This computational method allow us to study the nonlinear dispersion effect in principal modes without additional experimental requirements. Application-wise, the dispersion model enabled highly efficient multispectral system calibration strategies in MMF, which may be widely applicable to other complex media such as resonant cavities, disordered media, and biological tissues. The method may also spark new calibration strategies in nonlinear microscopy, multicolor imaging and sensing, and dispersion correction in meta-surfaces and photography.

In Chapter 5, we described a new depth profiling system by harnessing the random functions generated from MMF. The multiple pathlengths of broadband light transmission through MMF create a long sensing range and high axial resolution without assuming sample sparsity. The imaging specifications such as sensing range and signal to noise ratio can be reconfigured by altering the MMF input coupling and fiber scattering regime. We demonstrated depth reflectivity profiling of layered samples with centimeter range and micrometer axial resolution. The method may be useful in areas where a flexible trade-off between performance and system simplicity is beneficial, such as in industrial inspection, remote sensing (or LiDAR), or medical imaging, and may inspire extension to two and three-dimensional imaging.

In Chapter 6, we demonstrated a proximal calibration method to tackle the flexibility problem in MMF-based imaging systems. In an endoscopic setting, the reciprocal symmetry in proximal measurements imposes ambiguity in deriving the forward transmission, which is needed for focusing and imaging through MMF. The method is based on a distal calibration element, the knowledge in waveguide physics, and developed optimization approach. We showed, with experimental TMs, that the method allows reconstruction of MMF forward transmission with high accuracy. The optimization approach with entry-wise regularization is also analogous to least absolute shrinkage and selection operator (the so called Lasso method [130]), which was introduced in order to improve the prediction accuracy and interpretability of regression models.

7.2 Next Steps and Outlook

Looking forward, we believe that the following topics will guide the research direction towards practical MMF-based imaging and sensing probes:

1. Coherence gating through MMF for optical sectioning - We have shown a computational confocal gating effect by exploiting the DOFs of monochromatic transmission through

MMF, but the resolution, especially in the axial direction, depends heavily on the fiber NA and imaging distance. A superior 3D spatial resolution down to organelle scale may be straightforwardly achieved by using MMF with higher NA or operated at a shorter wavelength. However, this leads to an increased number of modes and thus inevitably longer MMF calibration and image acquisition time. Furthermore, the effective fiber NA decays with imaging distance, so the high-resolution imaging range may be very limited. Coherence gating, on the other hand, is another optical sectioning method that uses broadband low-coherence light or a wavelength-swept laser source to capture micrometer-resolution axial reflectivity profiles across the sensing range. The axial resolution relies on the spectral bandwidth instead of the spatial attributes. For example, current optical endoscopy based on optical coherence tomography (OCT) uses light source with bandwidth of several tens of nanometers and employs a SMF to deliver light between a remote sample and proximal detection. While the coherence gating technique has also been implemented on MCFs or fiber bundles [131, 132], to apply the technique to MMF imaging will require multispectral calibration as an inevitable prerequisite. Fortunately, as we introduced the dispersion model of transmission through MMF in Chapter 4, we can efficiently reconstruct spatio-spectral channels based on the computational methods and drastically reduce the number of measurements during multispectral calibration. As a result, realizing OCT through MMF may be a promising research direction.

2. Imaging weakly scattering samples through MMF - We have conducted proof-of-concept 3D reflectance imaging of layered samples, i.e., cell clusters on both front and back surfaces of a coverslip, through MMF based on computational reconstruction in Chapter 3. Reflection from the coverslip, which was $\sim$0.04, provided sufficient reflectance signals for imaging demonstration. However, biological tissues are weakly scattering samples with reflectivity as low as $\sim 10^{-4}$ to 10^{-5} [133], which can only be resolved with a much higher system sensitivity. Similar to OCT imaging systems, in our interferometric

detection setup, we may increase the reference arm power to amplify weak signals, but this will also amplify the specular reflection from fiber facet and saturate our limited camera dynamic range. As a next step, we may use anti-reflection coating on MMF facets or other engineering solutions to suppress the specular reflection from both the proximal and distal fiber facets to favor detection of weak sample signals [134, 135]. We can thereafter determine the optimal sample and reference arms power in the MMF imaging system to resolve realistic samples for biomedical applications.

3. Field of view, resolvable points, and imaging speed - As described in Appendix A, the lateral field of view (FOV) of imaging through flat-end MMF is bounded by fiber core size and NA. A large FOV can be obtained, however, at the expense of more invasiveness. As an alternative, side-view MMF imaging is possible with an engineered fiber termination that reduces compression and damage to the tissue [33]. We have also shown in Appendix B that, for monochromatric volumetric imaging through MMF, the number of total resolvable 3D voxels (throughput) is on the order of $\sim N^{3/2}$ ($N^{1/2}$ resolvable points in each spatial dimension), where N is the number of MMF guided modes. For instance, a SI-MMF with 100 µm core size and 0.22 NA operated at a visible wavelength may provide $\sim 10^4$(lateral) $\times$ 10^2(axial) $= 10^6$ resolvable voxels. While the number of *en face* resolvable points is close to a typical endo-microscope [136], and an even higher throughput (megapixel 2D image) may be achievable with a larger N (MMF with more modes), there is an inherent tradeoff between throughput and imaging speed. In our monochromatic polarization-resolved TM measurement, it took several to tens of seconds for MMF with several hundreds to over a thousand guided modes. The physical measurement speed is currently bottle-necked by the 120-Hz near-infrared InGaAs camera, and we may switch to other cameras at visible wavelength with > 20 kHz frame rate, which may significantly reduce the TM measurement time by a factor of > 100, leading to volumetric images in few frames per second for our computational imaging approach. Alternatively, the time reduction may also translate to real-time

proximal fiber calibration for flexible MMF-based imaging probes. Furthermore, as imaging through MMF with partial TM measurement at compression rate more than 90% is possible [86], we can study the optimal compression rate for realistic samples (or the optimal number of measurements) and may accelerate the imaging rate by more than another factor of 10.

4. Parameterizing dispersion in other complex medium - We have created a dispersion model of transmission through MMF and showed effective numerical dispersion compensation. To evaluate the efficacy of our parametric dispersion model on other complex media and find potential applications, we may repeat the same procedures with common scattering materials such as optical diffusers, disordered waveguides, or paint layer. While our current steepest descent optimization algorithm is sufficient for solving high order dispersion in several-meter-long MMF, new and more efficient optimization strategies for constructing dispersion model of longer or higher NA MMF will need further investigation. Integration of the dispersion model into the design of SDM systems with MMF will also be a good research topic in optical communications.

5. Other proximal calibration strategies - We have explained the technical challenge of on-site MMF calibration in an endoscopic setting. In the proposed proximal calibration method, to configure the distal calibration element into different realizations may need remote access to the distal end in practice, which, however, increases the fabrication complexity and cost. An alternative approach may be to include other constraints in the spectral domain: a passive distal element with strong dispersion such that when solving for the forward fiber transmission from the proximal multispectral measurements, we can apply the computational spectral correlation and impose additional constraints. This may avoid moving parts in the MMF distal end and relax the implementation difficulties.

6. Other sensing through MMF applications - We have developed an axial profiling system using the spatio-temporal modes generated from MMF. The similar idea to depth sensing

with MMF can be extended to other physical or chemical variation. For instance, we can use the same system to measure the refractive index of an unknown substance based on the pathlength change in the sample arm. Alternatively, we can calibrate the TM of MMF under different environments, and, in the sensing phase, measure the fiber perturbation and convert it to the corresponding physical quantities by analyzing the TM change. Previous literature on sensing with MMF typically used optical coupling efficiency through a MMF spatial channel as a single indicator for measuring the variation of physical quantities [137–140]. However, the TM approach uses full DOFs in the MMF, which may be more sensitive and offer a larger sensing range.

While remaining technical challenges for clinical translation of imaging through MMF are likely to be solved following the above-mentioned steps, there are still fundamental limitations of MMF imaging difficult to overcome. For reflectance imaging, which is ideal for clinical applications, since, on average, each resolvable point in sample space roughly requires one camera snapshot on the proximal side, the camera frame rate will be a hard limitation imposed on the imaging speed. Even with fast cameras with kHz frame rate and applying compressive measurement approach, it will still take several seconds to complete a megapixel 2D image through the MMF. A video-rate MMF-based endoscope may thus come at the expense of the number resolvable points. Another limitation is the imaging FOV, which scales linearly with the fiber core size and will typically be in sub-millimeter range. Combined with optical sectioning based on coherence gating with multispectral measurement, the realistic sample volume may be in the range of $\sim 10^7 \mu m^3$. Since the signal to background ratio (SBR) of imaging through MMF is essentially constrained by the number of guided modes, the limited SBR may restrict the image dynamic range to $\sim 10^3$ to 10^4. As a result, clinically speaking, we believe that this minimally invasive endoscopic imaging modality, under efficient placement guidance to lesion sites, is best suitable for visualizing pathology at cellular level such as infection, hyperplasia, hypertrophy, atrophy, and metaplasia. Such ability is critical for early diagnosis and prognosis improvement for serious or fatal diseases.

7.3 Final Conclusion

In this thesis, motivated by unmet medical needs, we proposed imaging and sensing through MMF for minimally invasive endoscopic applications. To achieve this, we studied and addressed critical technical challenges. We demonstrated the potential of computational reconstruction in overcoming hardware limitations, and the results also opened the door to many new science questions as discussed in each chapter. In addition, we developed various algorithms for correcting imperfection in experiments, investigating waveguide physics, signal processing, multi-variate fitting, and solving inverse problem based on linear algebra, matrix calculus, and optimization techniques. We believe the thesis has provided foundational elements towards developing a hair-thin MMF-based imaging probe that, as elaborated in future outlook, has high likelihood in clinical translation. Although the imaging throughput may not match the conventional white light video-endoscopy with megapixel specifications, the MMF-based endoscopic imaging will open new opportunities in biomedicine that are otherwise impossible with current technology.

Appendices

The microscope image is the interference effect of a diffraction phenomenon.

— Ernst Abbe

A

Resolution and Field of View in Imaging through MMFs

Contents

A.1 3D Resolution

To calculate the theoretical lateral and axial resolution, we need to first compute the effective NA, NA_{eff}, specific to an OP at an axial position. While the effective NA may also be dependent of the lateral displacement from the optical axis, we only consider an on-axis point object on the OP for convenience. Given the object at a distance d away from the MMF facet, the effective NA can be calculated from the maximal angle formed with the point as the vertex and marginal rays within the MMF acceptance angle as sides, as illustrated in Fig. A.1.1(a) and (b). When d is within the focal length of the MMF, $\Omega \sim \eta D/2NA$, a full NA can be obtained, which is determined during MMF fabrication.

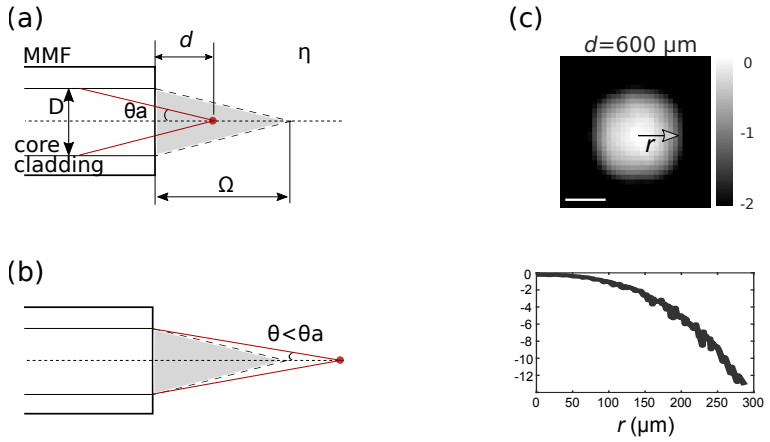

Figure A.1.1: Illustration of effective NA for an on-axis point object (red dot) on an OP (a) within and (b) beyond the MMF focal length. The dotted line indicates optical axis. (c) The simulated beam divergence at $d = 600$ μm with experimental **T**, and the circular blob diameter associates with the imaging FOV. The plotted radius-wise mean intensity in logarithmic scale with defined threshold determines the expected FOV on the OP at d. The scale bar is 100 μm.

Here, η is the medium refractive index, and θ_a is the fiber acceptance angle. Once d is larger than this range, only a partial NA can be achieved due to the limited MMF diameter. The value of effective NA is summarized as

$$NA_{eff} = \begin{cases} NA, & \text{if } d < \frac{\eta D}{2NA}. \\ \sim \frac{D}{2d}, & \text{otherwise.} \end{cases} \tag{A.1}$$

Given the effective NA, we can then compute the expected lateral and axial resolution as in confocal microscopy [141]

$$\delta x = \frac{0.4\,\lambda}{NA_{eff}} \tag{A.2a}$$

$$\delta z = \frac{1.4\,\eta\,\lambda}{NA_{eff}^2}, \tag{A.2b}$$

where we see that the axial resolution has a strong dependence on the system NA.

A.2 Field of View

With the circular symmetry of fiber core shape, we can define the FOV on an OP as the diameter of a circular area with circumference from furthest off-axis points having

normalized confocally detected intensity dropped below 1% threshold. Using the measured **T** of the MMF, we can free-space propagate each output light field per input to an OP and incoherently sum all output light intensity over each input realization. This results in a circular blob on the OP indicating the average illumination power at each spatial channel. Taking the spatial-channel-wise intensity square of the blob informs confocally detectable power, as shown in Fig. A.1.1(c), where the OP is 600 µm away from the MMF distal facet. The low light coupling efficiency at FOV peripheral causes the vignetting effect on reconstructed images, and the quantified FOV has ⌀∼260 µm by applying the threshold to plotted radius-wise mean intensity.

Calculus works by making visible the infinitesimally small.

— Keith Devlin

B

Resolvable Voxels in Imaging through MMF

Contents

The number of resolvable *en face* image features in monochromatic 2D imaging through MMFs has been discussed extensively [142, 143]. Given a MMF supporting N modes, the number of resolvable points is also $\sim N$. However, for volumetric imaging, especially the axial dimension, the achievable number of resolvable "depths" has not been studied so far. Here, we discuss the number of resolvable voxels (throughput) in 3D imaging through MMFs.

B.1 Number of Modes in MMF

Assume a step-index MMF with diameter D and NA operated at λ. The dimensionless V number is calculated as

$$V = \pi \cdot D \cdot NA/\lambda, \tag{B.1}$$

and the number of modes N is related to the V number

$$N \sim V^2/2. \tag{B.2}$$

B.2 Effective NA and Spatial Resolution

Consider an OP at d away from the facet, when d is smaller than the MMF focal length, the generated on-axis focus through the MMF has a minimal lateral dimension δ and depth of focus σ [144]

$$\begin{aligned} \delta_{min} &= 0.6\lambda/NA \\ \sigma_{min} &= 1.4\lambda/NA^2. \end{aligned} \tag{B.3}$$

However, when d is larger than the MMF focal length, the MMF has an effective NA

$$NA_{\mathit{eff}} = D/2d, \tag{B.4}$$

and we have

$$\begin{aligned} \delta &= 0.6\lambda/NA_{\mathit{eff}} \\ \sigma &= 1.4\lambda/NA_{\mathit{eff}}^2. \end{aligned} \tag{B.5}$$

δ is linearly proportional to d, whereas σ is proportional to the square of d. Note that while δ grows with d, it cannot exceed the aperture size D according to wave optics.

B.3 Number of Resolvable Observation Planes

Rearranging the variables, we can parameterize NA_{eff} and d as a function of δ

$$NA_{\mathit{eff}} = 0.6\lambda/\delta, \tag{B.6}$$

and

$$d = D\delta/\lambda. \tag{B.7}$$

To calculate the number of separated OPs N_{OP}, we integrate the number of depth of focus upon small δ increment

$$\begin{aligned} N_{OP} &= \int_{\delta_{min}}^{D} \frac{\frac{\partial d}{\partial \delta}}{\sigma} d\delta \\ &= \int_{\delta_{min}}^{D} 0.257 \frac{D}{\delta^2} d\delta \\ &= 0.257 \frac{D \cdot NA - \lambda}{\lambda} \\ &\sim 0.257 \frac{D \cdot NA}{\lambda} \\ &= \frac{0.257}{\pi} \sqrt{2N} \end{aligned} \tag{B.8}$$

B.4 Number of Resolvable Voxels

As illustrated in Fig. B.4.1, on each OP, we can have roughly N resolvable points, so, taking also the axial dimension into account, we can have total resolvable voxels within the MMF viewing cone

$$\begin{aligned} N_{total} &= N \cdot N_{OP} \\ &= N \cdot \frac{0.257}{\pi} \sqrt{2N} \\ &= 0.116 \cdot N^{\frac{3}{2}}, \end{aligned} \tag{B.9}$$

which is a finite number.

In our computational imaging in Chapter 3, we used a N-by-N reflection matrix $\mathbf{R}$ to model the reflectance of a sample, where the matrix $\mathbf{R}$ has N^2 complex elements, and we collected on-diagonal elements for confocal imaging. Assume the total detected out-of-focus background energy, B, distributed uniformly over the N^2 matrix elements of $\mathbf{R}$, and the in-focus signal intensity within a voxel S, then the theoretical signal to background ratio (SBR) of the voxel will be $\sim N^2 \cdot \frac{S}{B}$.

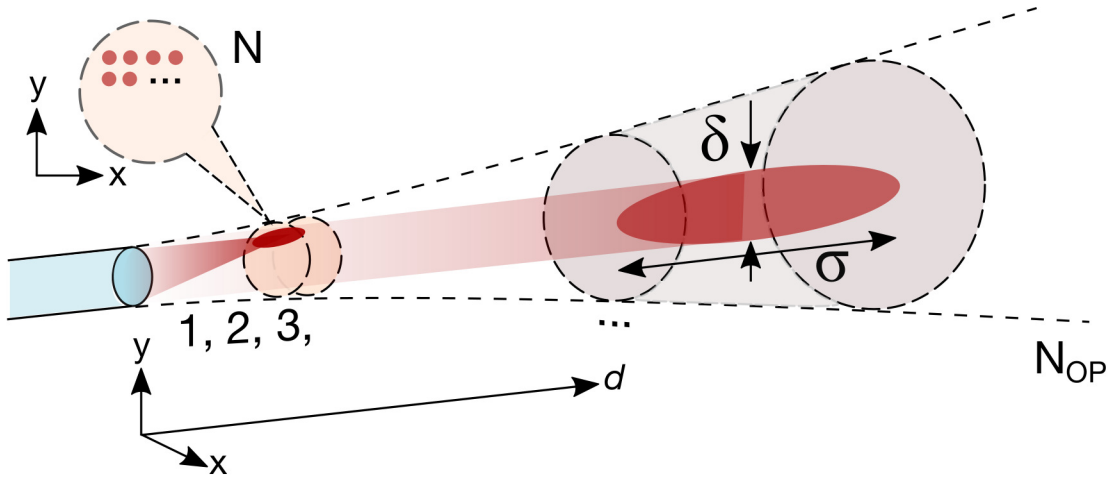

Figure B.4.1: Number of resolvable points in the MMF viewing angle. As the effective NA decays to a point where the lateral resolution approaches D, we cannot generate focus spots anymore since the wave from the fiber facet has no convergence.

It's not that I'm so smart, it's just that I stay with problems longer.

— Albert Einstein

C

Matrix Optimization with Unitary Constraints

Contents

Numerical matrix optimization under given constraints may involve optimization methods on Riemannian manifolds and require closed form gradient for efficient computation. In the Section 4.3.4, we optimized for complex matrix $\mathbf{D}(\Delta\omega) = e^{\mathbf{X}(\Delta\omega)} = e^{\sum_{k=1}^{K} \mathbf{X}_k \Delta\omega^k}$ under the unitary constraint, which is equivalent to the optimization of skew-Hermitian matrix $\mathbf{X}_k$. While optimization with orthogonality constraints was neither simple nor computationally cheap, we developed analytical gradient for Eq. 4.10 following the work by et al. [84].

C.1 Theory

We are trying to minimize the complement correlation

$$\arg\min_{\mathbf{X}_k \in \mathfrak{g}} \sum_{n=1}^{N} (1 - |tr(\mathbf{M}_n^\dagger e^{\sum_{k=1}^{K} \mathbf{X}_k \Delta\omega_n^k} \mathbf{M}(\omega_o))|^2), \tag{C.1}$$

which is equivalent to

$$\arg\min_{\mathbf{X}_k \in \mathfrak{g}} - \sum_{n=1}^{N} f(e^{\mathbf{X}(\Delta\omega_n)}), \tag{C.2}$$

where

$$\begin{aligned} f(e^{\mathbf{X}(\Delta\omega_n)}) &\equiv tr(\mathbf{A}_n^\dagger \mathbf{B}_n) tr(\mathbf{A}_n^\dagger \mathbf{B}_n)^*, \\ \mathbf{A}_n &\equiv \mathbf{M}_n, \\ \mathbf{B}_n &\equiv e^{\mathbf{X}(\Delta\omega_n)} \mathbf{M}(\omega_o), \\ \mathbf{X}(\Delta\omega_n) &\equiv \sum_{k=1}^{K} \mathbf{X}_k \Delta\omega_n^k. \end{aligned} \tag{C.3}$$

The gradient of $f(\cdot)$ with respect to $\mathbf{X}_k$

$$\frac{\partial f(e^{\mathbf{X}})}{\partial \mathbf{X}_k} = \frac{\partial f(e^{\mathbf{X}})}{\partial \mathbf{X}} \frac{\partial \mathbf{X}}{\partial \mathbf{X}_k} = \frac{\partial f(e^{\mathbf{X}})}{\partial \mathbf{X}} \Delta\omega^k \tag{C.4}$$

is subject to $\mathbf{X}_k \in \mathfrak{g}$. Since $\mathbf{X}_k$ is skew-Hermitian, $\mathbf{X}$ is also skew-Hermitian. This results in a constrained derivative

$$\frac{\partial f(e^{\mathbf{X}})}{\partial \mathbf{X}} = \nabla(f \circ \exp)(\mathbf{X}) = e^{\mathbf{X}} (\mathrm{d}\ \exp)_{-\mathbf{X}} (\frac{1}{2} (\nabla f(e^{\mathbf{X}})^\dagger e^{\mathbf{X}} - (e^{\mathbf{X}})^\dagger \nabla f(e^{\mathbf{X}}))), \tag{C.5}$$

where the unconstrained derivative

$$\nabla f(e^{\mathbf{X}}) \equiv \frac{\partial f(e^{\mathbf{X}})}{\partial e^{\mathbf{X}}} = -2 \cdot tr(\mathbf{M}_n^\dagger \mathbf{B}_n) \mathbf{M}_n \mathbf{M}_0^\dagger, \tag{C.6}$$

and the factorized differential of the exponential function on a matrix Lie group

$$\begin{aligned} \mathrm{d}\ \exp_{\mathbf{X}} \mathbf{Y} &= e^{\mathbf{X}} \phi(\mathrm{ad}_{\mathbf{X}})(\mathbf{Y}) = e^{\mathbf{X}} \frac{(1 - e^{-\mathrm{ad}_X})}{\mathrm{ad}_X}(\mathbf{Y}) = e^{\mathbf{X}} \sum_{k=0}^{\infty} \frac{(-1)^k}{(k+1)!} (\mathrm{ad}_{\mathbf{X}})^k (\mathbf{Y}), \\ \phi(\mathbf{Z}) &\equiv \frac{1 - e^{-\mathbf{Z}}}{\mathbf{Z}}, \\ \mathrm{ad}_{\mathbf{X}}(\mathbf{Y}) &= [\mathbf{X}, \mathbf{Y}]. \end{aligned} \tag{C.7}$$

Putting everything together, Eq. C.5 can be also written as

$$\nabla(f \circ \exp)(\mathbf{X}) = \sum_{k=0}^{\infty} \frac{(\mathrm{ad}_{\mathbf{X}})^k}{(k+1)!}(e^{-\mathbf{X}} \nabla f(e^{\mathbf{X}})), \tag{C.8}$$

and we can update $\mathbf{X}_k$ iteratively with the corresponding gradient.

C.2 Numerical Implementation

The differential of the exponential of matrices $(\mathrm{d}\exp)_{\mathbf{X}}$ can be approximated by Fréchet derivative to machine-precision through computing the exponential of a $2n \times 2n$ matrix [145]

$$e^{\begin{bmatrix} -\mathbf{X} & \mathbf{Q} \\ \mathbf{0} & -\mathbf{X} \end{bmatrix}} = \begin{bmatrix} e^{-\mathbf{X}} & (\mathrm{d}\exp)_{-\mathbf{X}}(\mathbf{Q}) \\ \mathbf{0} & e^{-\mathbf{X}} \end{bmatrix}. \tag{C.9}$$

During optimization, to do gradient decent and update all $\mathbf{X}_k$ in each iteration, we average the gradient of $\mathbf{X}_k$ over all frequencies

$$\mathbf{X}_k^{i+1} = \mathbf{X}_k^i - \alpha \frac{\partial f(e^{\mathbf{X}})}{\partial \mathbf{X}} \Delta\omega^k, \tag{C.10}$$

where i indicates the i-th optimization iteration, and α is the iteration step size (or learning rate).

References

[1] C.W. Hufeland. *Journal Der Practischen Arzneykunde Und Wundarzneykunst, 1809, Vol. 29 (Classic Reprint)*. Journal der practischen Arzneykunde und Wundarzneykunst. Wittich, 1806. URL: https://books.google.com.tw/books?id=dn8tAAAAcAAJ.

[2] Diederik F Janssen. "Who named and built the Désormeaux endoscope? The case of unacknowledged opticians Charles and Arthur Chevalier". In: *Journal of Medical Biography* 29.3 (2021). PMID: 33998906, pp. 176–179. eprint: https://doi.org/10.1177/09677720211018975. URL: https://doi.org/10.1177/09677720211018975.

[3] Sabina Beg, Ana Wilson, and Krish Ragunath. "The use of optical imaging techniques in the gastrointestinal tract". In: *Frontline Gastroenterology* 7.3 (2016). Ed. by Adolfo Parra Blanco, pp. 207–215. eprint: https://fg.bmj.com/content/7/3/207.full.pdf. URL: https://fg.bmj.com/content/7/3/207.

[4] Jingjing Sun and Huikai Xie. "MEMS-Based Endoscopic Optical Coherence Tomography". In: *International Journal of Optics* 2011 (June 2011), p. 825629. URL: https://doi.org/10.1155/2011/825629.

[5] Cameron M. Lee et al. "Scanning fiber endoscopy with highly flexible, 1 mm catheterscopes for wide-field, full-color imaging". In: *Journal of Biophotonics* 3.5-6 (2010), pp. 385–407. eprint: https://onlinelibrary.wiley.com/doi/pdf/10.1002/jbio.200900087. URL: https://onlinelibrary.wiley.com/doi/abs/10.1002/jbio.200900087.

[6] Brett E. Bouma et al. "Intravascular optical coherence tomography

Invited

". In: *Biomed. Opt. Express* 8.5 (2017), pp. 2660–2686. URL: http://www.osapublishing.org/boe/abstract.cfm?URI=boe-8-5-2660.

[7] Michalina J. Gora et al. "Endoscopic optical coherence tomography: technologies and clinical applications

Invited

". In: *Biomed. Opt. Express* 8.5 (May 2017), pp. 2405–2444. URL: http://www.osapublishing.org/boe/abstract.cfm?URI=boe-8-5-2405.

[8] Gyungseok Oh, Euiheon Chung, and Seok H. Yun. "Optical fibers for high-resolution in vivo microendoscopic fluorescence imaging". In: *Optical Fiber Technology* 19.6, Part B (2013). Optical Fiber Sensors, pp. 760–771. URL: https://www.sciencedirect.com/science/article/pii/S1068520013000886.

[9] Shailendra S. Chauhan et al. "Confocal laser endomicroscopy". In: *Gastrointestinal Endoscopy* 80.6 (2014), pp. 928–938. URL: https://doi.org/10.1016/j.gie.2014.06.021.

[10] Antonios Perperidis et al. "Image computing for fibre-bundle endomicroscopy: A review". In: *Medical Image Analysis* 62 (2020), p. 101620. URL: https://www.sciencedirect.com/science/article/pii/S136184151830639X.

[11] Viktor Tsvirkun et al. "Widefield lensless endoscopy with a multicore fiber". In: *Opt. Lett.* 41.20 (2016), pp. 4771–4774. URL: http://ol.osa.org/abstract.cfm?URI=ol-41-20-4771.

[12] Juergen C. Jung and Mark J. Schnitzer. "Multiphoton endoscopy". In: *Opt. Lett.* 28.11 (2003), pp. 902–904. URL: http://ol.osa.org/abstract.cfm?URI=ol-28-11-902.

[13] Michael J. Levene et al. "In Vivo Multiphoton Microscopy of Deep Brain Tissue". In: *Journal of Neurophysiology* 91.4 (2004). PMID: 14668300, pp. 1908–1912. eprint: https://doi.org/10.1152/jn.01007.2003. URL: https://doi.org/10.1152/jn.01007.2003.

[14] Iwamuro M et al. In: *World Journal of Gastroenterology* 26.13 (2020), pp. 1439–1449.

[15] Timo Rath et al. "High-definition endoscopy with digital chromoendoscopy for histologic prediction of distal colorectal polyps". In: *BMC Gastroenterology* 15.1 (2015), p. 145. URL: https://doi.org/10.1186/s12876-015-0374-3.

[16] Tina Schubert et al. "Optical improvements in the diagnosis of bladder cancer: implications for clinical practice". In: *Therapeutic advances in urology* 9.11 (2017), pp. 251–260. URL: https://doi.org/10.1177/1756287217720401.

[17] A. Goorsenberg et al. "Advances in Optical Coherence Tomography and Confocal Laser Endomicroscopy in Pulmonary Diseases". In: *Respiration* 99.3 (2020), pp. 190–205. URL: https://www.karger.com/DOI/10.1159/000503261.

[18] L. Thiberville et al. "Human in vivo fluorescence microimaging of the alveolar ducts and sacs during bronchoscopy". In: *European Respiratory Journal* 33.5 (2009), pp. 974–985. eprint: https://erj.ersjournals.com/content/33/5/974.full.pdf. URL: https://erj.ersjournals.com/content/33/5/974.

[19] Tsung-Han Tsai et al. "Optical coherence tomography in gastroenterology: a review and future outlook". In: *Journal of Biomedical Optics* 22.12 (2017), pp. 1 –17. URL: https://doi.org/10.1117/1.JBO.22.12.121716.

[20] Youngwoon Choi et al. "Scanner-Free and Wide-Field Endoscopic Imaging by Using a Single Multimode Optical Fiber". In: *Phys. Rev. Lett.* 109 (20 2012), p. 203901. URL: https://link.aps.org/doi/10.1103/PhysRevLett.109.203901.

[21] Sergey Turtaev et al. “High-fidelity multimode fibre-based endoscopy for deep brain in vivo imaging”. In: *Light: Science & Applications* 7.1 (2018), p. 92. URL: http://www.nature.com/articles/s41377-018-0094-x.

[22] Martin Plöschner et al. “Multimode fibre: Light-sheet microscopy at the tip of a needle”. In: *Scientific Reports* 5.1 (2015), p. 18050. URL: https://doi.org/10.1038/srep18050.

[23] Allard P. Mosk et al. “Controlling waves in space and time for imaging and focusing in complex media”. In: *Nature Photonics* 6.5 (2012), pp. 283–292. URL: https://doi.org/10.1038/nphoton.2012.88.

[24] S. M. Popoff et al. “Measuring the Transmission Matrix in Optics: An Approach to the Study and Control of Light Propagation in Disordered Media”. In: *Phys. Rev. Lett.* 104 (10 2010), p. 100601. URL: https://link.aps.org/doi/10.1103/PhysRevLett.104.100601.

[25] Ioannis N. Papadopoulos et al. “Focusing and scanning light through a multimode optical fiber using digital phase conjugation”. In: *Opt. Express* 20.10 (2012), pp. 10583–10590. URL: http://www.opticsexpress.org/abstract.cfm?URI=oe-20-10-10583.

[26] Roberto Di Leonardo and Silvio Bianchi. “Hologram transmission through multi-mode optical fibers”. In: *Opt. Express* 19.1 (2011), pp. 247–254. URL: http://opg.optica.org/oe/abstract.cfm?URI=oe-19-1-247.

[27] Tomáš Čižmár and Kishan Dholakia. “Shaping the light transmission through a multimode optical fibre: complex transformation analysis and applications in biophotonics”. In: *Opt. Express* 19.20 (2011), pp. 18871–18884. URL: http://opg.optica.org/oe/abstract.cfm?URI=oe-19-20-18871.

[28] Cizmar T. “Exploiting multimode waveguides for pure fibre-based imaging”. In: *Nat. Commun.* 3 (2012), p. 1027.

[29] Damien Loterie et al. “Digital confocal microscopy through a multimode fiber”. In: *Opt. Express* 23.18 (2015), pp. 23845–23858. URL: http://www.opticsexpress.org/abstract.cfm?URI=oe-23-18-23845.

[30] Martin Plöschner, Tomáš Tyc, and Tomáš Čižmár. “Seeing through chaos in multimode fibres”. In: *Nature Photonics* 9.8 (2015), pp. 529–535.

[31] Shay Ohayon et al. “Minimally invasive multimode optical fiber microendoscope for deep brain fluorescence imaging”. In: *Biomed. Opt. Express* 9.4 (2018), pp. 1492–1509. URL: http://www.osapublishing.org/boe/abstract.cfm?URI=boe-9-4-1492.

[32] Angel Cifuentes et al. “Polarization-resolved second-harmonic generation imaging through a multimode fiber”. In: *Optica* 8.8 (2021), pp. 1065–1074. URL: http://www.osapublishing.org/optica/abstract.cfm?URI=optica-8-8-1065.

[33] Beatriz M. Silveira et al. “Side-view holographic endomicroscopy via a custom-terminated multimode fibre”. In: *Opt. Express* 29.15 (2021), pp. 23083–23095. URL: http://www.osapublishing.org/oe/abstract.cfm?URI=oe-29-15-23083.

[34] Navid Borhani et al. “Learning to see through multimode fibers”. In: *Optica* 5.8 (2018), pp. 960–966. URL: http://www.osapublishing.org/optica/abstract.cfm?URI=optica-5-8-960.

[35] Edgar E. Morales-Delgado, Demetri Psaltis, and Christophe Moser. “Two-photon imaging through a multimode fiber”. In: *Opt. Express* 23.25 (2015), pp. 32158–32170. URL: http://www.opticsexpress.org/abstract.cfm?URI=oe-23-25-32158.

[36] Damien Loterie, Demetri Psaltis, and Christophe Moser. “Bend translation in multimode fiber imaging”. In: *Opt. Express* 25.6 (2017), pp. 6263–6273. URL: http://www.opticsexpress.org/abstract.cfm?URI=oe-25-6-6263.

[37] Ruo Yu Gu, Reza Nasiri Mahalati, and Joseph M. Kahn. “Design of flexible multi-mode fiber endoscope”. In: *Opt. Express* 23.21 (2015), pp. 26905–26918. URL: http://www.opticsexpress.org/abstract.cfm?URI=oe-23-21-26905.

[38] Dirk E. Boonzajer Flaes et al. “Robustness of Light-Transport Processes to Bending Deformations in Graded-Index Multimode Waveguides”. In: *Phys. Rev. Lett.* 120 (23 2018), p. 233901. URL: https://link.aps.org/doi/10.1103/PhysRevLett.120.233901.

[39] George S. D. Gordon et al. “Characterizing Optical Fiber Transmission Matrices Using Metasurface Reflector Stacks for Lensless Imaging without Distal Access”. In: *Phys. Rev. X* 9 (4 2019), p. 041050. URL: https://link.aps.org/doi/10.1103/PhysRevX.9.041050.

[40] Shuhui Li et al. “Memory effect assisted imaging through multimode optical fibres”. In: *Nature Communications* 12.1 (2021), p. 3751. URL: https://doi.org/10.1038/s41467-021-23729-1.

[41] Szu-Yu Lee et al. “Reciprocity-induced symmetry in the round-trip transmission through complex systems”. In: *APL Photonics* 5.10 (2020), p. 106104. URL: https://doi.org/10.1063/5.0021285.

[42] A. Yariv. “Optical Electronics in Modern Communications Fifth Edition”. In: 2012.

[43] D. Marcuse. “Gaussian approximation of the fundamental modes of graded-index fibers”. In: *J. Opt. Soc. Am.* 68.1 (1978), pp. 103–109. URL: http://opg.optica.org/abstract.cfm?URI=josa-68-1-103.

[44] Robert Brüning et al. “Overlap relation between free-space Laguerre Gaussian modes and step-index fiber modes”. In: *J. Opt. Soc. Am. A* 32.9 (2015), pp. 1678–1682. URL: http://josaa.osa.org/abstract.cfm?URI=josaa-32-9-1678.

[45] Mahdieh B. Shemirani et al. “Principal Modes in Graded-Index Multimode Fiber in Presence of Spatial- and Polarization-Mode Coupling”. In: *J. Lightwave Technol.* 27.10 (2009), pp. 1248–1261. URL: http://www.osapublishing.org/jlt/abstract.cfm?URI=jlt-27-10-1248.

[46] Wen Xiong et al. “Principal modes in multimode fibers: exploring the crossover from weak to strong mode coupling”. In: *Opt. Express* 25.3 (2017), pp. 2709–2724. URL: http://www.osapublishing.org/oe/abstract.cfm?URI=oe-25-3-2709.

[47] Per Christian Hansen. "The L-curve and its use in the numerical treatment of inverse problems". English. In: *InviteComputational Inverse Problems in Electrocardiology*. InviteComputational Inverse Problems in Electrocardiology ; Conference date: 01-01-2000. WIT Press, 2000.

[48] Maxime W. Matthès et al. *Learning and avoiding disorder in multimode fibers*. 2020. arXiv: 2010.14813 [physics.optics].

[49] Hermann A. Haus. *Waves and fields in optoelectronics*. Englewood Cliffs, NJ : Prentice-Hall, [1984] ©1984, [1984]. URL: https://search.library.wisc.edu/catalog/999550742402121.

[50] Potton R. J. "Reciprocity in optics". In: *Rep. Prog. Phys.* 67 (2004), p. 717.

[51] Onsager L. "Reciprocal relations in irreversible processes. I." In: *Phys. Rev.* 37 (1931), p. 405.

[52] Casimir H. B. G. "Reciprocity theorems and irreversible processes". In: *Proc. IEEE* 51 (1963), p. 1570.

[53] Silveirinha M. G. "Hidden time-reversal symmetry in dissipative reciprocal systems". In: *Opt. Express* 27 (2019), p. 14328.

[54] Bromberg Y. "Control of coherent backscattering by breaking optical reciprocity". In: *Phys. Rev. A* 93 (2016), p. 023826.

[55] Wiersma D. S. "Breaking reciprocity". In: *Nat. Photonics* 6 (2012), p. 506.

[56] Cui M. "Implementation of a digital optical phase conjugation system and its application to study the robustness of turbidity suppression by phase conjugation". In: *Opt. Express* 18 (2010), p. 3444.

[57] Yaqoob Z. "Optical phase conjugation for turbidity suppression in biological samples". In: *Nat. Photonics* 2 (2008), p. 110.

[58] Vellekoop I. M. "Digital optical phase conjugation of fluorescence in turbid tissue". In: *Appl. Phys. Lett.* 101 (2012), p. 081108.

[59] Popoff S. "Image transmission through an opaque material". In: *Nat. Commun.* 1 (2010), p. 81.

[60] Jalas D. "What is—and what is not—an optical isolator". In: *Nat. Photonics* 7 (2013), p. 579.

[61] Wen Xiong et al. "Complete polarization control in multimode fibers with polarization and mode coupling". In: *Light: Science & Applications* 7.1 (2018), p. 54. URL: https://doi.org/10.1038/s41377-018-0047-4.

[62] Y. Bromberg et al. "Control of coherent backscattering by breaking optical reciprocity". In: *Phys. Rev. A* 93 (2 2016), p. 023826. URL: https://link.aps.org/doi/10.1103/PhysRevA.93.023826.

[63] B. Picinbono. "Second-order complex random vectors and normal distributions". In: *IEEE Transactions on Signal Processing* 44.10 (1996), pp. 2637–2640.

[64] F.D. Neeser and J.L. Massey. “Proper complex random processes with applications to information theory”. In: *IEEE Transactions on Information Theory* 39.4 (1993), pp. 1293–1302.

[65] Mooseok Jang et al. “Method for auto-alignment of digital optical phase conjugation systems based on digital propagation”. In: *Opt. Express* 22.12 (2014), pp. 14054–14071. URL: http://www.opticsexpress.org/abstract.cfm?URI=oe-22-12-14054.

[66] Lyubov V. Amitonova and Johannes F. de Boer. “Compressive imaging through a multimode fiber”. In: *Optics Letters* 43.21 (2018).

[67] George S. D. Gordon et al. “Characterizing Optical Fiber Transmission Matrices Using Metasurface Reflector Stacks for Lensless Imaging without Distal Access”. In: *Phys. Rev. X* 9 (4 2019), p. 041050. URL: https://link.aps.org/doi/10.1103/PhysRevX.9.041050.

[68] P. C. Hansen. “The L-Curve and its Use in the Numerical Treatment of Inverse Problems”. In: *in Computational Inverse Problems in Electrocardiology, ed. P. Johnston, Advances in Computational Bioengineering*. WIT Press, 2000, pp. 119–142.

[69] Youngwoon Choi et al. “Overcoming the Diffraction Limit Using Multiple Light Scattering in a Highly Disordered Medium”. In: *Phys. Rev. Lett.* 107 (2 2011), p. 023902. URL: https://link.aps.org/doi/10.1103/PhysRevLett.107.023902.

[70] Drew Scoles, Yusufu N. Sulai, and Alfredo Dubra. “In vivo dark-field imaging of the retinal pigment epithelium cell mosaic”. In: *Biomed. Opt. Express* 4.9 (2013), pp. 1710–1723. URL: http://www.osapublishing.org/boe/abstract.cfm?URI=boe-4-9-1710.

[71] “Removal of back-reflection noise at ultrathin imaging probes by the single-core illumination and wide-field detection”. In: *Scientific Reports* 7.1 (2017), p. 6524. URL: https://doi.org/10.1038/s41598-017-07024-y.

[72] Tomáš Čižmár and Kishan Dholakia. “Exploiting multimode waveguides for pure fibre-based imaging”. In: *Nature Communications* 3 (2012). arXiv: /www.pubmedcentral.nih.gov/articlerender.fcgi?artid=3006164{\&}tool=pmcentrez{\&}rendertype=abstract. [Figures, S., 2010. Supplementary information. Nature, 1(c), pp.1-7. Available at: http:].

[73] Jian Liu et al. “3D dark-field confocal microscopy for subsurface defects detection”. In: *Optics Letters* 45.3 (2020), p. 660.

[74] Jaewook Shin et al. “A minimally invasive lens-free computational microendoscope”. In: *Science Advances* 5.12 (2019). eprint: https://advances.sciencemag.org/content/5/12/eaaw5595.full.pdf. URL: https://advances.sciencemag.org/content/5/12/eaaw5595.

[75] Wonjun Choi et al. *Fourier holographic endoscopy for label-free imaging through a narrow and curved passage*. 2020. arXiv: 2010.11776 [physics.optics].

[76] M. GU, H. BAO, and H. KANG. "Fibre-optical microendoscopy". In: *Journal of Microscopy* 254.1 (2014), pp. 13–18. eprint: https://onlinelibrary.wiley.com/doi/pdf/10.1111/jmi.12119. URL: https://onlinelibrary.wiley.com/doi/abs/10.1111/jmi.12119.

[77] Antoine Boniface et al. "Transmission-matrix-based point-spread-function engineering through a complex medium". In: *Optica* 4.1 (2017), pp. 54–59. URL: http://www.osapublishing.org/optica/abstract.cfm?URI=optica-4-1-54.

[78] Antonio M. Caravaca-Aguirre et al. "Real-time resilient focusing through a bending multimode fiber". In: *Opt. Express* 21.10 (2013), pp. 12881–12887. URL: http://www.opticsexpress.org/abstract.cfm?URI=oe-21-10-12881.

[79] Shuhui Li et al. "Compressively sampling the optical transmission matrix of a multimode fibre". In: *Light: Science & Applications* 10.1 (2021), p. 88. URL: https://doi.org/10.1038/s41377-021-00514-9.

[80] Dirk E. Boonzajer Flaes et al. "Robustness of Light-Transport Processes to Bending Deformations in Graded-Index Multimode Waveguides". In: *Phys. Rev. Lett.* 120 (23 2018), p. 233901. URL: https://link.aps.org/doi/10.1103/PhysRevLett.120.233901.

[81] Shanhui Fan and Joseph M. Kahn. "Principal modes in multimode waveguides". In: *Optics Letters* 30.2 (2005), p. 135.

[82] Rohan Prasad and Kumar Appaiah. "Impact of modulation bandwidth on multiplexing using principal modes in MMF links". In: *Opt. Express* 26.2 (2018), pp. 1779–1795. URL: http://www.osapublishing.org/oe/abstract.cfm?URI=oe-26-2-1779.

[83] Jiang Hu et al. *A Brief Introduction to Manifold Optimization*. 2019. arXiv: 1906.05450 [math.OC].

[84] Mario Lezcano-Casado and David Martínez-Rubio. *Cheap Orthogonal Constraints in Neural Networks: A Simple Parametrization of the Orthogonal and Unitary Group*. 2019. arXiv: 1901.08428 [cs.LG].

[85] Martin Arjovsky, Amar Shah, and Yoshua Bengio. *Unitary Evolution Recurrent Neural Networks*. 2016. arXiv: 1511.06464 [cs.LG].

[86] Szu-Yu Lee et al. "Confocal 3D reflectance imaging through multimode fiber without wavefront shaping". In: *Optica* 9.1 (2022), pp. 112–120. URL: http://www.osapublishing.org/optica/abstract.cfm?URI=optica-9-1-112.

[87] Etienne Cuche, Pierre Marquet, and Christian Depeursinge. "Spatial filtering for zero-order and twin-image elimination in digital off-axis holography". In: *Appl. Opt.* 39.23 (2000), pp. 4070–4075. URL: http://ao.osa.org/abstract.cfm?URI=ao-39-23-4070.

[88] Joel Carpenter, Benjamin J. Eggleton, and Jochen Schröder. "Observation of Eisenbud–Wigner–Smith states as principal modes in multimode fibre". In: *Nature Photonics* 9.11 (2015), pp. 751–757. URL: https://doi.org/10.1038/nphoton.2015.188.

[89] Damien Loterie, Demetri Psaltis, and Christophe Moser. "Bend translation in multimode fiber imaging". In: *Optics Express* 25.6 (2017). URL: https://doi.org/10.1364/OE.25.006263.

[90] Susana Silva et al. "Ultrahigh-sensitivity temperature fiber sensor based on multimode interference." In: *Applied optics* 51 16 (2012), pp. 3236–42.

[91] Mickael Mounaix and Joel Carpenter. "Control of the temporal and polarization response of a multimode fiber". In: *Nature Communications* 10.1 (2019), p. 5085. URL: https://doi.org/10.1038/s41467-019-13059-8.

[92] Antoine Boniface et al. "Rapid broadband characterization of scattering medium using hyperspectral imaging". In: *Optica* 6.3 (2019), pp. 274–279. URL: http://www.osapublishing.org/optica/abstract.cfm?URI=optica-6-3-274.

[93] Shuhui Li et al. "Compressively sampling the optical transmission matrix of a multimode fibre". In: *Light: Science & Applications* 10.1 (2021), p. 88. URL: https://doi.org/10.1038/s41377-021-00514-9.

[94] Brandon Redding et al. "High-resolution and broadband all-fiber spectrometers". In: *Optica* 1.3 (2014), pp. 175–180. URL: http://www.osapublishing.org/optica/abstract.cfm?URI=optica-1-3-175.

[95] Louisiane Devaud et al. "Chromato-axial memory effect in step-index multimode fibers". In: *APL Photonics* 6.12 (2021), p. 126105. eprint: https://doi.org/10.1063/5.0067892. URL: https://doi.org/10.1063/5.0067892.

[96] D J Richardson, J M Fini, and L E Nelson. "Space-division multiplexing in optical fibres". In: *Nature Photonics* 7.5 (2013), pp. 354–362. URL: https://doi.org/10.1038/nphoton.2013.94.

[97] Nicolas K. Fontaine et al. "Laguerre-Gaussian mode sorter". In: *Nature Communications* 10.1 (2019), p. 1865. URL: https://doi.org/10.1038/s41467-019-09840-4.

[98] Georg Rademacher et al. "Peta-bit-per-second optical communications system using a standard cladding diameter 15-mode fiber". In: *Nature Communications* 12.1 (2021), p. 4238. URL: https://doi.org/10.1038/s41467-021-24409-w.

[99] Szu-Yu Lee et al. "Single-shot depth profiling by spatio-temporal encoding with a multimode fiber". In: *Opt. Express* 28.2 (2020), pp. 1124–1138. URL: http://www.opticsexpress.org/abstract.cfm?URI=oe-28-2-1124.

[100] Joseph N. Mait, Gary W. Euliss, and Ravindra A. Athale. "Computational imaging". In: *Adv. Opt. Photon.* 10.2 (2018), pp. 409–483. URL: http://aop.osa.org/abstract.cfm?URI=aop-10-2-409.

[101] Matthew P. Edgar, Graham M. Gibson, and Miles J. Padgett. "Principles and prospects for single-pixel imaging". In: *Nature Photonics* 13.1 (2019), pp. 13–20. URL: https://doi.org/10.1038/s41566-018-0300-7.

[102] Marco F. Duarte et al. “Single-pixel imaging via compressive sampling”. In: *IEEE Signal Processing Magazine* 25.2 (2008), pp. 83–91.

[103] Youngwoon Choi et al. “Overcoming the Diffraction Limit Using Multiple Light Scattering in a Highly Disordered Medium”. In: *Phys. Rev. Lett.* 107 (2 2011), p. 023902. URL: https://link.aps.org/doi/10.1103/PhysRevLett.107.023902.

[104] E Mudry et al. “Structured illumination microscopy using unknown speckle patterns”. In: *Nature Photonics* 6.5 (2012), pp. 312–315.

[105] Hasan Yilmaz et al. “Speckle correlation resolution enhancement of wide-field fluorescence imaging”. In: *Optica* 2.5 (2015), pp. 424–429. URL: http://www.osapublishing.org/optica/abstract.cfm?URI=optica-2-5-424.

[106] Mani Ratnam Rai, A. Vijayakumar, and Joseph Rosen. “Extending the field of view by a scattering window in an I-COACH system”. In: *Opt. Lett.* 43.5 (2018), pp. 1043–1046. URL: http://ol.osa.org/abstract.cfm?URI=ol-43-5-1043.

[107] Meihua Liao et al. “Extending the depth-of-field of imaging systems with a scattering diffuser”. In: *Scientific Reports* 9.1 (2019), p. 7165. URL: https://doi.org/10.1038/s41598-019-43593-w.

[108] Alok Kumar Singh et al. “Exploiting scattering media for exploring 3D objects”. In: *Light: Science & Applications* 6.2 (2017), e16219–e16219. URL: https://doi.org/10.1038/lsa.2016.219.

[109] Nick Antipa et al. “DiffuserCam: lensless single-exposure 3D imaging”. In: *Optica* 5.1 (2018), pp. 1–9. URL: http://www.osapublishing.org/optica/abstract.cfm?URI=optica-5-1-1.

[110] Sujit Kumar Sahoo, Dongliang Tang, and Cuong Dang. “Single-shot multispectral imaging with a monochromatic camera”. In: *Optica* 4.10 (2017), pp. 1209–1213. URL: http://www.osapublishing.org/optica/abstract.cfm?URI=optica-4-10-1209.

[111] Patrick Llull et al. “Coded aperture compressive temporal imaging”. In: *Opt. Express* 21.9 (2013), pp. 10526–10545. URL: http://www.opticsexpress.org/abstract.cfm?URI=oe-21-9-10526.

[112] Kenneth MacCabe et al. “Pencil beam coded aperture x-ray scatter imaging”. In: *Opt. Express* 20.15 (2012), pp. 16310–16320. URL: http://www.opticsexpress.org/abstract.cfm?URI=oe-20-15-16310.

[113] Tomohiro Shirai, Tero Setälä, and Ari T. Friberg. “Temporal ghost imaging with classical non-stationary pulsed light”. In: *J. Opt. Soc. Am. B* 27.12 (2010), pp. 2549–2555. URL: http://josab.osa.org/abstract.cfm?URI=josab-27-12-2549.

[114] Zhipeng Chen et al. “Temporal ghost imaging with a chaotic laser”. In: *Optical Engineering* 52.7 (2013), pp. 1 –7. URL: https://doi.org/10.1117/1.OE.52.7.076103.

[115] Piotr Ryczkowski et al. “Ghost imaging in the time domain”. In: *Nature Photonics* 10.3 (2016), pp. 167–170. URL: https://doi.org/10.1038/nphoton.2015.274.

[116] Fabrice Devaux et al. “Computational temporal ghost imaging”. In: *Optica* 3.7 (2016), pp. 698–701. URL: http://www.osapublishing.org/optica/abstract.cfm?URI=optica-3-7-698.

[117] Christoph Hauger, Marco Wörz, and Thomas Hellmuth. “Interferometer for optical coherence tomography”. In: *Appl. Opt.* 42.19 (2003), pp. 3896–3902. URL: http://www.osapublishing.org/ao/abstract.cfm?URI=ao-42-19-3896.

[118] Peter Koch, Volker Hellemanns, and Gereon Hüttmann. “Linear optical coherence tomography system with extended measurement range”. In: *Opt. Lett.* 31.19 (2006), pp. 2882–2884. URL: http://www.osapublishing.org/ol/abstract.cfm?URI=ol-31-19-2882.

[119] Salma Farahi et al. “Dynamic bending compensation while focusing through a multimode fiber”. In: *Opt. Express* 21.19 (2013), pp. 22504–22514. URL: http://www.osapublishing.org/oe/abstract.cfm?URI=oe-21-19-22504.

[120] Jian Zhao et al. “Deep Learning Imaging through Fully-Flexible Glass-Air Disordered Fiber”. In: *ACS Photonics* 5.10 (2018), pp. 3930–3935. URL: https://doi.org/10.1021/acsphotonics.8b00832.

[121] Pengfei Fan, Tianrui Zhao, and Lei Su. “Deep learning the high variability and randomness inside multimode fibers”. In: *Opt. Express* 27.15 (2019), pp. 20241–20258. URL: http://www.osapublishing.org/oe/abstract.cfm?URI=oe-27-15-20241.

[122] Rajendra Bhatia. “The bipolar decomposition”. In: *Linear Algebra and its Applications* 439.10 (2013), pp. 3031–3037. URL: https://www.sciencedirect.com/science/article/pii/S0024379513005612.

[123] Charles R. Johnson, Kazuyoshi Okubo, and Robert Reams. “Uniqueness of matrix square roots and an application”. In: *Linear Algebra and its Applications* 323.1 (2001), pp. 51–60. URL: https://www.sciencedirect.com/science/article/pii/S0024379500002433.

[124] Szu-Yu Lee, Martin Villiger, and Brett Bouma. “Proximal measurement of multimode fiber transmission matrix (Conference Presentation)”. In: *Adaptive Optics and Wavefront Control for Biological Systems V*. Ed. by Thomas G. Bifano, Sylvain Gigan, and Na Ji. Vol. 10886. International Society for Optics and Photonics. SPIE, 2019. URL: https://doi.org/10.1117/12.2509043.

[125] Emmanuel J. Candes and Michael B. Wakin. “An Introduction To Compressive Sampling”. In: *IEEE Signal Processing Magazine* 25.2 (2008), pp. 21–30.

[126] Ryan J. Tibshirani and Jonathan Taylor. “The solution path of the generalized lasso”. In: *The Annals of Statistics* 39.3 (2011), pp. 1335 –1371. URL: https://doi.org/10.1214/11-AOS878.

[127] Mark A. Davenport et al. “Introduction to compressed sensing”. In: *Compressed Sensing: Theory and Applications*. Cambridge University Press, 2012, 1–64.

[128] Shachar Resisi, Sebastien M. Popoff, and Yaron Bromberg. "Image Transmission Through a Dynamically Perturbed Multimode Fiber by Deep Learning". In: *Laser & Photonics Reviews* 15.10 (2021), p. 2000553. eprint: https://onlinelibrary.wiley.com/doi/pdf/10.1002/lpor.202000553. URL: https://onlinelibrary.wiley.com/doi/abs/10.1002/lpor.202000553.

[129] E. P. Pozhidaev et al. "Polymer dispersed liquid crystals with electrically controlled light scattering in the visible and near-infrared ranges". In: *Opt. Mater. Express* 10.12 (2020), pp. 3030–3040. URL: http://www.osapublishing.org/ome/abstract.cfm?URI=ome-10-12-3030.

[130] Robert Tibshirani. "Regression Shrinkage and Selection via the Lasso". In: *Journal of the Royal Statistical Society. Series B (Methodological)* 58.1 (1996), pp. 267–288. URL: http://www.jstor.org/stable/2346178.

[131] Tuqiang Xie et al. "Fiber-optic-bundle-based optical coherence tomography". In: *Opt. Lett.* 30.14 (2005), pp. 1803–1805. URL: http://ol.osa.org/abstract.cfm?URI=ol-30-14-1803.

[132] G. S. D. Gordon et al. "Coherent Imaging Through Multicore Fibres With Applications in Endoscopy". In: *Journal of Lightwave Technology* 37.22 (2019), pp. 5733–5745.

[133] J. A. Izatt and M. A. Choma. "Theory of Optical Coherence Tomography". In: *Optical Coherence Tomography: Technology and Applications*. Ed. by Wolfgang Drexler and James G. Fujimoto. Berlin, Heidelberg: Springer Berlin Heidelberg, 2008, pp. 47–72. URL: https://doi.org/10.1007/978-3-540-77550-8_2.

[134] Matthew D. Risi et al. "Analysis of multimode fiber bundles for endoscopic spectral-domain optical coherence tomography". eng. In: *Applied optics* 54.1 (2015). 25967012[pmid], pp. 101–113. URL: https://pubmed.ncbi.nlm.nih.gov/25967012.

[135] Ivo T. Leite et al. "Observing distant objects with a multimode fiber-based holographic endoscope". In: *APL Photonics* 6.3 (2021), p. 036112. URL: https://doi.org/10.1063/5.0038367.

[136] Wenxuan Liang et al. "Throughput-Speed Product Augmentation for Scanning Fiber-Optic Two-Photon Endomicroscopy". In: *IEEE Transactions on Medical Imaging* 39 (2020), pp. 3779–3787.

[137] H.A. Rahman et al. "Tapered plastic multimode fiber sensor for salinity detection". In: *Sensors and Actuators A: Physical* 171.2 (2011), pp. 219–222. URL: https://www.sciencedirect.com/science/article/pii/S0924424711005383.

[138] Susana Silva et al. "Ultrahigh-sensitivity temperature fiber sensor based on multimode interference". In: *Applied Optics* 51.16 (2012), pp. 3236–3242. URL: http://www.osapublishing.org/ao/abstract.cfm?URI=ao-51-16-3236.

[139] Haris Apriyanto et al. “Comprehensive Modeling of Multimode Fiber Sensors for Refractive Index Measurement and Experimental Validation”. In: *Scientific Reports* 8.1 (2018), p. 5912. URL: https://doi.org/10.1038/s41598-018-24153-0.

[140] D. A. May-Arrioja et al. “Linear multimode interference fiber temperature sensor using the liquid in glass thermometer principle”. In: *Appl. Opt.* 58.14 (2019), pp. 3856–3861. URL: http://www.osapublishing.org/ao/abstract.cfm?URI=ao-58-14-3856.

[141] Thomas J. Fellers Kenneth R. Spring and Michael W. Davidson. “Resolution and Contrast in Confocal Microscopy”. In: *Olympus - Life Science Solutions* (). URL: https://www.olympus-lifescience.com/en/microscope-resource/primer/techniques/confocal/resolutionintro/.

[142] Changhyeong Yoon et al. “Experimental measurement of the number of modes for a multimode optical fiber”. In: *Opt. Lett.* 37.21 (2012), pp. 4558–4560. URL: http://ol.osa.org/abstract.cfm?URI=ol-37-21-4558.

[143] Reza Nasiri Mahalati, Ruo Yu Gu, and Joseph M. Kahn. “Resolution limits for imaging through multi-mode fiber”. In: *Opt. Express* 21.2 (2013), pp. 1656–1668. URL: http://www.opticsexpress.org/abstract.cfm?URI=oe-21-2-1656.

[144] Y. Hiraoka, J.W. Sedat, and D.A. Agard. “Determination of three-dimensional imaging properties of a light microscope system. Partial confocal behavior in epifluorescence microscopy”. In: *Biophysical Journal* 57.2 (1990), pp. 325–333. URL: https://www.sciencedirect.com/science/article/pii/S0006349590825340.

[145] Awad H. Al-Mohy and Nicholas J. Higham. “Computing the Fréchet Derivative of the Matrix Exponential, with an Application to Condition Number Estimation”. In: *SIAM Journal on Matrix Analysis and Applications* 30.4 (2009), pp. 1639–1657. eprint: https://doi.org/10.1137/080716426. URL: https://doi.org/10.1137/080716426.